

REPUBLIQUE DU CAMEROUN

Paix-Travail-Patrie

UNIVERSITE DE YAOUNDE I

CENTRE DE RECHERCHE ET DE
FORMATION DOCTORALE EN
SCIENCE TECHNOLOGIE ET
GEOSCIENCES

UNITE DE RECHERCHE ET DE
FORMATION DOCTORALE
PHYSIQUE ET APPLICATIONS



REPUBLIC OF CAMEROON

Peace-Work-Fatherland

UNIVERSITY OF YAOUNDE I

POSTGRADUATE SCHOOL OF

SCIENCE, TECHNOLOGY &
GEOSCIENCES

RESEARCH AND POSTGRADUATE
TRAINING UNIT FOR
PHYSICS AND APPLICATIONS

Laboratory of Mechanics, Materials and Structure

Laboratoire de Mecanique, Matériaux et Structure

Continuous-Wave and Femtosecond Lasers Inscriptions on Amorphous Silica Glass

Thesis defended publicly on June 4, 2021 at the University of Yaounde I in
fulfilment for the Award of Doctorat/Ph.D. in Physics

Option: Materials Science

By:

KAMENI NTEUTSE PEGUY

Matricule: 10W0315

Master's in Physics

Under the Supervision of:

ZEKENG SERGE SYLVAIN

Professor, University of Yaounde I

and

DIKANDÉ ALAIN MOISE

Professor, University of Buea



Year 2021





DEPARTEMENT DE PHYSIQUE
DEPARTMENT OF PHYSICS

ATTESTATION DE CORRECTION DE LA
THESE DE DOCTORAT/Ph.D

Nous, Professeur NANA NBENDJO Blaise Roméo, Examineur, et Professeur TCHAWOUA Clément, Président du Jury de la Thèse de Doctorat/Ph.D de Monsieur KAMENI NTEUTSE Peguy, Matricule 10W0315, préparée sous les directions du Professeur DIKANDE Alain Moise, et Professeur ZEKENG Serge Sylvain, intitulée : « *Continuous-Wave and Femtosecond Lasers Inscriptions on Amorphous Silica Glass* », soutenue le vendredi, 04 juin 2021 en vue de l'obtention du grade de Docteur/Ph.D en Physique, Spécialité Sciences des Matériaux, attestons que toutes les corrections demandées par le Jury de soutenance ont été effectuées.

En foi de quoi, la présente attestation lui est délivrée pour servir et valoir ce que de droit.

Fait à Yaoundé le 10 juin 2021

Examineur

Pr. NANA NBENDJO Blaise Roméo

Le Président du Jury

Pr. TCHAWOUA Clément



Le Chef de Département de Physique

Bienvenu
Professeur

Dedication

To my parents:

Ngimene Mathieu and Leutchoua

Augustine.

Acknowledgements

-I would like to thank my supervisors **Prof. DIKANDÉ Alain Moise** and **Prof. ZEKENG Serge Sylvain** for their valuable guidance and support extended during the course of this research.

-I would like to thank the **Postgraduate School of Science, Technology and Geosciences Research and Postgraduate Training Unit for Physics and Applications**, University of Yaounde 1.

-I would like to thank the Head of the physics department **Prof. NDJAKA Jean-Marie Bienvenu**, for the wonderful advice that he has provided to me as well as all my lecturer from the physics department at the University of Yaounde 1. Special thanks goes to, **Prof. NDJAKA Jean-Marie Bienvenu**, **Prof. KOFANE Timoléon Crépin**, **Prof. WOAFU Paul**, **Prof. TCHAWOUA Clément**, **Prof. PEMHA Elkana**, **Prof. ESSIMBI ZOBO Bernard**, **Prof. HONA Jacques**, **Prof. FOUEDJO David**, **Prof. WAKATA Annie**, **Prof. NDOP Joseph**, **Prof. NDJANDJOCK NOUCK Philippe**, **Prof. BEN-BOLIE Germain**, **Prof. FEWO Serge**, **Dr. TCHOFFO Fidèle**, **Dr. EDONGUE Hervais** and **Dr. TEYOU NGOUPO Ariel**, for the knowledge that I have benefited from them during my training at the University of Yaounde 1.

I must equally extend a hand of gratitude to the academic director of AIMS-Cameroon **Prof. GARUTI Marco** as well as **Prof. NANA NBENDJO Blaise Romeo**, **Dr. WAMBA Etienne**, **Dr. FOTSING Hans** and **Dr. TSOBGNI Pelerine** for the valuable discussions I had with them, and the support and encouragement they offered during the course of this research.

I would also like to express my thanks to the African Institute for Mathematical Sciences (AIMS)-Rwanda and Cameroon branches, for a visit during which part of this work was completed.

My appreciations are also extended to all my friends and classmates at the University of Yaounde 1 for their support extended during the course of this research.

Finally, my special thank goes to my family for their love, care and support that was a source of inspiration and motivation for all I have achieved in my life.

Contents

Dedication	ii
Acknowledgements	iii
Contents	vi
Abstract	vii
Résumé	ix
List of abbreviations	xi
List of Tables	xii
List of Figures	0
General Introduction	1
Chapter 1: State of the Art on Lasers and Laser Inscriptions	5
1.1 Overview on laser	5
1.1.1 Brief historical development of lasers	5
1.1.2 Basic principles of laser	6
1.1.3 The laser beam	7
1.1.4 Different types of lasers and application	8
1.2 Laser interaction with transparent material	11
1.2.1 Optical Kerr effect	11
1.2.2 Photoionization	16
1.2.3 Avalanche ionization and plasma generation	17

1.2.4	Laser-plasma interaction	19
1.3	Generality on laser inscription: marking and engraving	21
1.3.1	Methods of laser inscription technologies	21
1.3.2	Inscription criteria and mark legibility characteristics	24
1.3.3	Important inscription parameters	27
1.3.4	Marking and engraving transparent materials	31
1.4	Femtosecond laser inscription on transparent material	40
Chapter 2: Material, Theoretical Model and Methodology		42
2.1	Crystalline and amorphous silica structures	43
2.1.1	Crystalline silica structure	44
2.1.2	Amorphous silica structure	44
2.2	Amorphous silica glass properties	46
2.3	Characteristics of the lasers used for inscription on amorphous silica	49
2.3.1	Characteristic of continuous-wave laser	49
2.3.2	Characteristic of pulsed laser	49
2.4	Theoretical model for laser inscription on amorphous silica glass	51
2.4.1	Laser equation	52
2.4.2	Equation for the plasma generation in amorphous silica glass	62
2.4.3	Theoretical model	64
2.5	Methodology	65
2.5.1	Fourth-order Runge Kutta algorithm	66
Chapter 3: Results and Discussion		68
3.1	Stability investigation of the continuous-wave laser inscription on amorphous silica glass in the presence of plasma generation	69
3.1.1	Model without recombination processes in the plasma generated	69
3.1.2	Steady states solutions of the laser in the continuous-wave regime	69
3.1.3	Continuous-wave laser frequency in the steady state	72
3.1.4	Laser fluence in the steady state	72
3.1.5	Modulational-instability analysis of the laser in the continuous-wave regime	73
3.1.6	Summary	82

3.2 Stability investigation of the continuous-wave laser inscription on amorphous silica glass in the presence of plasma generated: effect of radiative recombination 85

 3.2.1 Steady states solutions 85

 3.2.2 Laser fluence 88

 3.2.3 Benjamin-Feir instability analysis of a continuous-wave 88

 3.2.4 Summary 94

3.3 Stability investigation of pulsed laser inscription on amorphous silica glass 94

 3.3.1 Fixed-point solutions 96

 3.3.2 Pulses stability 99

 3.3.3 Summary 110

General Conclusion and Perspectives 112

References 129

This thesis proposes a theoretical approach to explore the effects of the competition between multi-photon absorption, group-velocity dispersion and electron-hole radiative recombination processes, on the laser beam dynamics (i.e. continuous-wave and femtosecond regimes) and stability (spot) during inscription on amorphous silica glass. The study rests on a model consisting of a K -order nonlinear complex Ginzburg-Landau equation, coupled with a Drude-type equation for the electron plasma density. In this goal, the modulational instability analysis combined with the dynamical approach was used to explore all the possible operation regimes inherent to the stability of the model. For the modulational instability analysis, we have considered a single input laser intensity in the continuous wave regime then we started the analysis from an input field in the steady state, and followed its stability when coupling a small perturbation with the laser amplitude as it propagates in an anisotropic transparent amorphous silica glass. An analysis of the stability of continuous-waves regime, following the modulational-instability theory, reveals that, in the absence of electron-hole radiative recombination, the competing effects of Kerr nonlinearity and K -photon absorptions can stabilize or destabilize the continuous wave laser beam during the inscription process. However, in the presence of electron-hole radiative recombination, our analysis of stability of continuous-waves regime, following the modulational-instability, suggests that the competitions between multi-photon absorption and radiative recombination processes can be detrimental or favorable to continuous-wave laser stability, depending on the group-velocity dispersion of amorphous silica glass. In the full nonlinear dynamical regime, we have chosen a specific ansatz (to represent a femtosecond laser) that we introduced in the model and this allows us to transform the system of model equations into a system of four equations of first order (ODE's) for which we examined its singular solutions by exploring the possible fixed points, as a function of the multi-photon absorption rate K . Then, we proceeded numerically to solve the system of four equations of first order ordinary differential equation (ODE's), using a fourth-order Runge-Kutta algorithm. Numerical simulations of the full nonlinear regime reveal the existence of the stable pulse trains for which the amplitudes are increased by the radiative recombination processes. From these last results, we were able to derive the femtosecond laser beam spot

diameter $d_{spot} = 50\mu\text{m}$ that could allow to obtain a fine engraving on amorphous silica glass.

Keywords: Laser Inscription, Engraving, Multi-photon Absorptions, Avalanche Ionization, Plasma Generation, Radiative Recombination, Modulational-Instability, Continuous Waves Laser, Femtosecond laser, Pulse train, Amorphous Silica.

Cette thèse propose une étude théorique pour explorer les effets compétitifs entre l'absorption multi-photonique, la dispersion de la vitesse de groupe, et les processus de recombinaison radiative électron-trou, sur la dynamique et la stabilité du faisceau laser continu et femtoseconde (spot) lors de l'inscription sur un verre de silice amorphe. L'étude repose sur un modèle consistant en une équation de Ginzburg-Landau complexe non linéaire d'ordre K , couplée à une équation de type Drude, décrivant l'évolution temporelle de la densité du plasma d'électrons généré dans la silice amorphe. Dans cette optique, l'analyse de l'instabilité modulationnelle combinée à l'approche dynamique a été utilisée pour explorer tous les régimes d'opération possibles inhérents à la stabilité du modèle. Pour la technique d'analyse de l'instabilité modulationnelle, nous avons considéré une intensité laser d'entrée en régime d'onde continue, puis nous avons commencé l'analyse par un champ d'entrée en régime permanent, et nous avons suivi sa stabilité en couplant une petite perturbation sur l'amplitude du faisceau laser continu lorsqu'il se propage dans le verre de silice amorphe optiquement anisotrope. Une analyse de la stabilité du faisceau laser en mode continue, suivant la théorie de l'instabilité modulationnelle, révèle qu'en l'absence de recombinaison radiative électron-trou, les effets compétitifs de la non-linéarité Kerr et de l'absorption multi-photonique peuvent stabiliser ou déstabiliser le faisceau laser continue pendant le processus d'inscription. Cependant, en présence d'une recombinaison radiative électron-trou, notre analyse de la stabilité en mode continue, au moyen de l'instabilité modulationnelle, suggère que la compétition entre les processus d'absorption multi-photonique et de recombinaison radiative peut être préjudiciable ou favorable à la stabilité en régime continu, selon la dispersion de la vitesse de groupe dans le verre de silice amorphe. Dans le régime dynamique complètement non linéaire, nous avons choisi une solution spécifique (pour représenter un laser femtoseconde) que nous avons introduite dans le modèle et cela nous a permis de transformer le système d'équations du modèle en un système de quatre équations différentielle linéaire du premier ordre (EDO) pour lequel nous avons examiné ses solutions singulières en explorant les points fixes possibles, en fonction du taux d'absorption multi-photonique K . Ensuite, nous avons résolu numériquement le système de quatre équations (EDO) du premier ordre, en utilisant l'algorithme de Runge-Kutta d'ordre quatre. Les simulations numériques

du régime complètement non linéaire révèlent l'existence des trains d'ondes stables dont les amplitudes sont augmentées par la recombinaison radiative. À partir de ces derniers résultats, nous avons pu déterminer le diamètre du spot laser femtoseconde $d_{spot} = 50\mu\text{m}$ sur la surface du verre de silice amorphe qui permettrait d'obtenir une gravure fine.

Mots-clés : Inscription laser, Gravure, Absorption multi-photon, Ionisation par avalanche, Génération de plasma, Recombinaison radiative, Instabilité modulationnelle, Laser à ondes continues, Laser femtoseconde, Train d'ondes, Silice amorphe.

List of abbreviations

- ☞ Li_2CO_3 : Lithium Carbonate
- ☞ SiO_2 : Silicon Dioxide
- ☞ $Nd : YAG$: Neodymium-Doped Yttrium Aluminum Garnet
- ☞ Al_2O_3 : Aluminum Oxide
- ☞ CO_2 : Carbon Dioxide
- ☞ ArF : Argon fluoride
- ☞ CW: Continuous-Wave
- ☞ PW: Pulsed-Wave
- ☞ ps: picosecond
- ☞ fs: femtosecond
- ☞ LIBS: Laser Induce Breakdown Spectroscopy
- ☞ HAZ: Heat Affected Zone
- ☞ SAZ: Shock Affected Zone
- ☞ MPI: Multi-photon Ionization
- ☞ MPA: Multi-photon Absorption

List of Tables

2.1	Some Important Properties of Amorphous Silica Glass	46
3.1	Parameters for which pulses is unstable: $\omega = 1.3$ rad/fs	105
3.2	Parameters for which pulses is stable: $\omega = 1.5$ rad/fs	110

List of Figures

1	Examples letter "A" printed with laser radiation stable (left) and unstable laser radiation (right) [23].	3
1.1	A cross-sectional view of the first Ruby Laser [28].	6
1.2	Schematic set up of Laser system [30].	7
1.3	Comparison between ordinary light properties and laser light [31].	8
1.4	identification of a potassium, in the matrix Li_2CO_3 using LIBS approach. . . .	10
1.5	Comparison of damages produce by CW-laser, ns-laser and ps/fs laser on the transparent material [31].	10
1.6	A schematic of single and multiphoton absorption of incident photons (shown in red) causing electrons to be promoted to the conduction band from the valence band. [38].	16
1.7	Diagram of the photoionization of an electron through tunnelling (left), multiphoton ionization (right) and both non-linear processes (central) with different values for Keldysh parameter γ [39].	17
1.8	Schematic potential energy diagram for avalanche ionization (right), that follows after seed electrons are created by multi-photon absorption (left) [39].	18
1.9	Plasma expansion by pulse laser. $I(r)$, spatial intensity distribution; r , radius; τ , pulse duration, HAZ is the heat affected zone, and SAZ is the shock affected zone [2].	19
1.10	Schematic representation of the focusing-defocusing cycles undergone by the intense core of the beam [9].	20
1.11	Occurrence of different physical phenomena during different timescales involved in laser-material interaction [42].	20
1.12	An Example of mask inscription system [46].	22

1.13 Engraving using raster or dot matrix inscription [48, 49].	23
1.14 Engraving via vector inscription method [48].	23
1.15 Engraving of bar-codes: a) 1D; b) 2D [51, 52].	23
1.16 An example of beam deflected inscription system [48].	24
1.17 Microcracks along a line generated by a Nd:YAG laser on a plastic leadless chip carrier covered with a gold-nickel lid; with pulse energy of 0.1 J, pulse duration of 0.6 ms, argon as the assist gas, gas pressure of 0.2 MPa, lens focal length of 150 mm, focal position of 0.1 mm away from the material, and percentage overlap of 85% [59].	26
1.18 View of the spot diameter of the laser beam on the transparent material [59].	28
1.19 Effects of increasing the lens focal length [65].	29
1.20 Effects of increasing the lens focal length [65].	29
1.21 Laser marking (left) and laser engraving (right) [47].	31
1.22 Cross-section of laser scribed Al_2O_3 substrate in air [72].	32
1.23 Vaporization effect of a letter "8" marked on a ceramic package using Nd:YAG laser [59].	33
1.24 Effect of pulse frequency on mark width and depth with different lamp current (left) and Effect of pulse frequency on mark intensity with different lamp current (right) [73].	34
1.25 Microscopy observation of the microcrack induced by the laser in the glass float around the engraved zone [20].	36
1.26 Description of the effects of the laser parameters on the glass float surface engraved with CO_2 laser in the continuous-wave regime ($\lambda = 10.6\mu\text{m}$ and the maximum power $P = 60\text{W}$) [20].	37
1.27 Data matrix engraved on glass material with CO_2 laser operating in pulse regime using wavelength of $10.6\mu\text{m}$, with a fluence of $7\text{J}/\text{cm}^2$ and 10 pulses [20].	38
1.28 Data matrix engraved on clear glass material using ArF excimer laser with the wavelength of 193 nm, with a fluence of $F = 0.95\text{J}/\text{cm}^2$ and 200 pulses [66].	39
1.29 Laser ablation of transparent material with $F = 0.8\text{J}/\text{cm}^2$ (left) and $F = 0.2\text{J}/\text{cm}^2$ (right) both of them with $\lambda = 612\text{nm}$ and $T = 300$ femtosecond [2].	40

2.1	Tetrahedral pattern of silica [79].	43
2.2	Diagram of the phase transition paths between different varieties of silica at 1 atmosphere pressure, as controlled by temperature [79].	44
2.3	Crystalline structures of SiO_2 : 2D (left) and 3D (right) [83, 84].	44
2.4	Amorphous structures of SiO_2 : 2D (left) and 3D (right) [83, 84].	45
2.5	Continuous-wave laser output (left) and Pulsed laser output right [91].	50
2.6	Experimental setup for implementation of plasma assisted material processing in the bulk of amorphous silica [83].	51
3.1	Imaginary versus real parts of κ_1 (full curve) and κ_2 (dashed curve), for $I_0 = 2.5$, $\nu = 0.5$, $\gamma_0 = 0.1$, $\omega_0\tau_0 = 0.2$, $\sigma = 0.8$, $\mu = -0.1$ and $\delta = -0.5$. The four graphs are for $K = 2, 3, 4, 5$, as indicated in the graphs.	78
3.2	Imaginary versus real parts of κ_1 (full curve) and κ_2 (dashed curve), for $K = 2, 3, 4, 5$. Other parameter values are $I_0 = 2.5$, $\nu = 0.5$, $\gamma_0 = 0.1$, $\omega_0\tau_0 = 0.2$, $\sigma = 0.8$, $\mu = -0.1$ and $\delta = 0.5$	79
3.3	Imaginary versus real parts of κ_1 (full curve) and κ_2 (dashed curve), for $K = 2, 3, 4, 5$. Other parameter values are $I_0 = 2.5$, $\nu = 0.05$, $\gamma_0 = 0.1$, $\omega_0\tau_0 = 0.2$, $\sigma = 0.8$, $\mu = -0.1$ and $\delta = -0.5$	80
3.4	Imaginary versus real parts of κ_1 (full curve) and κ_2 (dashed curve), for $K = 2, 3, 4, 5$. Other parameter values are $I_0 = 2.5$, $\nu = 0.05$, $\gamma_0 = 0.1$, $\omega_0\tau_0 = 0.2$, $\sigma = 0.8$, $\mu = -0.1$ and $\delta = 0.5$	81
3.5	Imaginary versus real parts of κ_1 (full curve) and κ_2 (dashed curve), for $K = 2, 3, 4, 5$. Other parameter values are $I_0 = 2.5$, $\nu = 0.5$, $\gamma_0 = 0.1$, $\omega_0\tau_0 = 1.1$, $\sigma = 0.8$, $\mu = -0.1$ and $\delta = -0.5$	83
3.6	Imaginary versus real parts of κ_1 (full curve) and κ_2 (dashed curve), for $K = 2, 3, 4, 5$. Other parameter values are $I_0 = 2.5$, $\nu = 0.5$, $\gamma_0 = 0.1$, $\omega_0\tau_0 = 1.1$, $\sigma = 0.8$, $\mu = 0.1$ and $\delta = 0.5$	84
3.7	Imaginary versus real parts of κ_1 (full curve) and κ_2 (dashed curve) for $K = 2, 3, 4, 5$. The radiative recombination coefficient a is varied as $a = 0, 0.001, 0.002, 0.003, 0.004$. $\alpha = 0.6$, $\nu = 0.5$, $\mu = 0.1$, $I_p = 2.5$, $\omega_0\tau_0 = 0.2$, $\sigma = 0.8$, $\delta = -0.5$, $\gamma_0 = 0.1$	92

3.8	Imaginary versus real parts of κ_1 (full curve) and κ_2 (dashed curve) for $K = 2, 3, 4, 5$. The radiative recombination coefficient a is varied as $a = 0, 0.001, 0.002, 0.003, 0.004$. $\alpha = 0.6, \nu = 0.5, \mu = 0.1, I_p = 2.5, \omega_0\tau_0 = 0.2, \sigma = 0.8, \delta = 0.5, \gamma_0 = 0.1$	93
3.9	Fixed points of the laser amplitude g as a function of ω , for $K = 2, 3, 4, 5$, $\sigma = 0.8, \omega_0\tau_0 = 0.2, \mu = 0.25$	98
3.10	Variation of the instantaneous frequency M with the amplitude g of laser, for $K = 2, 3, 4, 5$ and two different values of ω indicated in the graphs. $\sigma = 0.8$, $\omega_0\tau_0 = 0.2, \mu = 0.25, \delta = -0.5$	100
3.11	Variation of the laser amplitude g with the electron plasma density ρ , for K $= 2, 3, 4, 5$ and different values of the radiative re- combination coefficient a indicated in the graphs. $\nu = 0.1, \alpha = 0.6, \gamma_0 = 0.1, \mu = 0.25$	101
3.12	Time variation of the laser amplitude g , for $K = 2, 3, 4, 5$ and different values of the radiative recombination coefficient a indicated in the graphs. $\sigma = 0.8$, $\omega_0 = 1.38, \tau_0 = 0.58, \delta = -0.5, \mu = 0.5, \nu = 0.5, \gamma_0 = 0.18, \alpha = 0.6$	102
3.13	Time variation of the electron plasma density ρ , for $K = 2, 3, 4, 5$ and values of a indicated in the graphs. $\sigma = 0.8, \omega_0 = 1.38, \tau_0 = 0.58, \delta = -0.5, \mu = 0.5$, $\nu = 0.5, \gamma_0 = 0.18, \alpha = 0.6$	103
3.14	Time variation of the electron plasma density ρ , for $K = 2, 3, 4, 5$ and values of a indicated in the graphs. $\sigma = 0.8, \omega_0 = 1.38, \tau_0 = 0.58, \delta = -0.5, \mu = 0.5$, $\nu = 0.5, \gamma_0 = 0.18, \alpha = 0.6$	106
3.15	Time variation of the electron plasma density ρ , for $K = 2, 3, 4, 5$ and values of a indicated in the graphs. $\sigma = 0.8, \omega_0 = 1.38, \tau_0 = 0.58, \delta = -0.5, \mu = 0.5$, $\nu = 0.5, \gamma_0 = 0.18, \alpha = 0.6$	107
3.16	Time variation of the electron plasma density ρ , for $K = 2, 3, 4, 5$ and values of a indicated in the graphs. $\sigma = 0.8, \omega_0 = 1.38, \tau_0 = 0.58, \delta = -0.5, \mu = 0.5$, $\nu = 0.5, \gamma_0 = 0.18, \alpha = 0.6$	108
3.17	Time variation of the laser amplitude g , for $K = 2, 3, 4, 5$ and different values of the radiative recombination coefficient a indicated in the graphs. $\sigma = 0.8$, $\omega_0 = 1.38, \tau_0 = 0.58, \delta = -0.5, \mu = 0.5, \nu = 0.5, \gamma_0 = 0.18, \alpha = 0.6$	109

General Introduction

Laser inscription nowadays offers one of the most reliable and easily portable tools in a broad range of modern industrial material processing [1, 2]. Applications extend from accurate manufacturing of electronic devices to fine engraving and machining of hard metals, ceramics and soft plastics into various micro textures for improvement of functions and properties of end products [3, 4]. In these applications laser beam focused on a dielectric medium is absorbed via nonlinear photo-ionization mechanisms [5, 6], leading to a permanent modification of material structure at scales of the order of nanometers. In the specific context of transparent materials [7, 6], at low pulse powers, the modification will be a smooth refractive index change which can be exploited advantageously in the fabrication of photonic devices [3, 8]. However, at higher pulse powers, the modification gives rise to more complex processes such as birefringences, periodic nanoplanes aligning themselves orthogonally to the laser polarization to form periodic nanogratings, change in the electronic structure due to electron and hole productions from charge ionization with the generation of electron plasma, electron-hole radiative recombination processes [3, 6, 8], etc..

Although, laser inscription on transparent materials, usually relies on three main factors, namely the characteristic laser parameters (i.e. the laser power, pulse duration, pulse repetition rate and laser beam spot size), characteristic properties of host materials (e.g. their absorption, reflection, transmission, chromatic dispersions, optical nonlinearities or self-focusing conditions etc.), and the relative importance of physical processes such as the electron plasma generation, multiphoton absorption, and electron-hole radiative recombination. These factors (laser and medium) act in conjunction to impose the regime of laser operation, in particular their competition determines the laser stability in a specific operation regime. Indeed, in accordance with the fineness required at the end of an inscription, optical fields used in laser material processing can be operated in two different regimes [3, 9, 8], namely: continuous-wave (cw) regime, and pulsed regime [9]. Laser operating in pulsed regime can allow inscription with high resolution in depth and therefore offer a rich potential for applications in drilling [3], cutting [10], welding [11, 12], ablation [11], material surface texturing and scripting [11, 12]. Of the class of pulsed lasers, we remark that besides their short duration and high powers, femtosecond laser have

been most attractive owing to their minimal thermal drawbacks [13, 14]. Indeed femtosecond laser are able to accumulate heat such as to minimize defect-induced damages, as a matter of fact this heat accumulation prevents undesired physical casualties as for instance the formation of microcracks, material bending, etc. [15], notably during laser engraving/or marking transparent glasses [16, 17]. Furthermore, femtosecond laser are highly attractive in modern laser processing technologies [18, 19], with possibility of applications in optical waveguide fabrications, direct laser writing on optical discs, lasers marking and engraving on transparent materials [20].

Theoretical considerations of femtosecond laser inscription on transparent materials have attracted only little attention in the study of laser machining processes [21, 16, 9]. The motivation for such considerations rests on a need for a good understanding not only of physical processes involved in the processes, but also of the implications of the combination of these physical processes on the aspects like the laser stability in its distinct possible operation regimes during inscription on transparent material. Indeed, as already mentioned above, a plasma is formed because of the nonlinear absorption of the laser radiation in transparent material. However, it is reported that the presence of this plasma leads to a protective shield on the material's upper surface [22]. Due to plasma influence, the incident laser energy gradually decreases as it interacts with the material while the plasma keeps expanding. As a consequence, there is a transition dynamics of the laser due to its instability. Such a process driven by an instability-induced dynamical transition of laser can affect namely the shape, size and fineness of the characters to be engraved on transparent material. In fact, to achieve the desired shape, size and fineness of the characters to be engraved on the transparent material surface, the laser beam (spot) should be stable in the inscription processes. Figure 1 is an examples letter "A" printed with stable laser beam (left) and unstable laser beam (right).

In this thesis, we propose a theoretical study to investigate the continuous-wave and femtosecond laser dynamics and stability during inscription on a transparent material with promising applications in engraving. Before following the ultimate goal of our study, we would like to underline that transparent material here refers to any material that could manipulate or modify light properties (e.g. Glasses, lenses, reflecting prisms, mirror, optical fibres etc.). The transparent material that attracted our attention in the present work is amorphous silica glass best known as fused silica glass. This material will be well presented in chapter 2.



Figure 1: Examples letter "A" printed with laser radiation stable (left) and unstable laser radiation (right) [23].

However, as already stressed above, for this inscription application, the laser beam spot must operate in a specific regime as a continuous wave or as a pulsed wave and should be stable during the materials processing. In general, continuous-wave laser is useful when we do not want a very fine character, while pulsed waves (i.e. femtosecond laser) are necessary when we want to have a very fine character on the material. If the laser beam spot is not stable on the material during the process, then the precision and the fineness of the characters to be generated on the material will not be achieved. Therefore, if we understand the laser stability via theoretical model, we can prevent undesired printing errors on amorphous silica glass during its inscription. Investigating the stability of laser beam spot is relevant for an optimum preconditioning for the required quality, precision and fineness in a step of laser inscription on amorphous silica glass. In this thesis, we address these issues and our investigation will be based on the theoretical model that will be constructed in chapter 2. In order to achieve our objective, this thesis will be organized as follows:

In chapter 1, we introduce some basic concepts regarding lasers as well as laser transparent material-interaction. Then we emphasize on laser inscription process where, we presented the two methods used in the inscription technology. In addition to this we also defined the important parameters used in the inscription process. To end this chapter, we presented a previous work done on lasers marking and engraving.

In chapter 2, we present the amorphous silica glass structure as well as its different properties. Then we build the theoretical model dedicated to our study and the chapter end with the methodology of our work.

In chapter 3, we utilize the theoretical model that we built in chapter 2 to investigate the continuous-wave and femtosecond laser dynamics and stability during inscription on amorphous silica glass, taking into account multi-photon absorption, Kerr nonlinearity, plasma generation and electron-hole radiative recombination processes in the plasma generated.

State of the Art on Lasers and Laser Inscriptions

The objective of this chapter is to introduce some basic concepts regarding lasers as well as the advantages of using femtosecond laser in the inscription processes. As we are already stressed in our introduction that a transparent material is any material that could manipulate or modify the light properties, then we will be emphasized on the laser inscriptions on transparent materials in general. In this goal, some previous works done on the lasers marking and engraving will be presented.

1.1 Overview on laser

1.1.1 Brief historical development of lasers

The word laser is an acronym which stands for light amplification by stimulated emission of radiation. Actually, laser is a photonic device that produces intense beams of light which are monochromatic, coherent, and highly collimated. In 1917, Albert Einstein introduced the theory of stimulated emission. He hypothesized that if a molecule or an atom is in an excited state, it will give up its energy if acted upon by a quantum of the same energy [24]. Therefore, this idea permitted Ch.H. Townes, J.P. Gordon and H.J. Zeiger in 1954 to build the very first maser (microwave amplifier by stimulated emission of radiation) [25, 26]. Then in 1957, Bloembergen *et al.* realized the second generation of maser whose device was emitted in the infrared domain. Just one year (1958) after the maser was performed to generate light in the infrared range, Schawlow and Townes concluded that it is possible to adapt this device in such a way that it can generate wave at higher frequency energy, corresponding to a visible domain [27]. The pioneering works of Townes, Bassov, Schawlow and Prokhorov, permitted Theodore

Maiman in 1960, to invent the first laser using ruby crystals whose device was emitting optical radiation with the wavelength 694 nm as shown on figure 1.1 [28]. The same year, Javan,

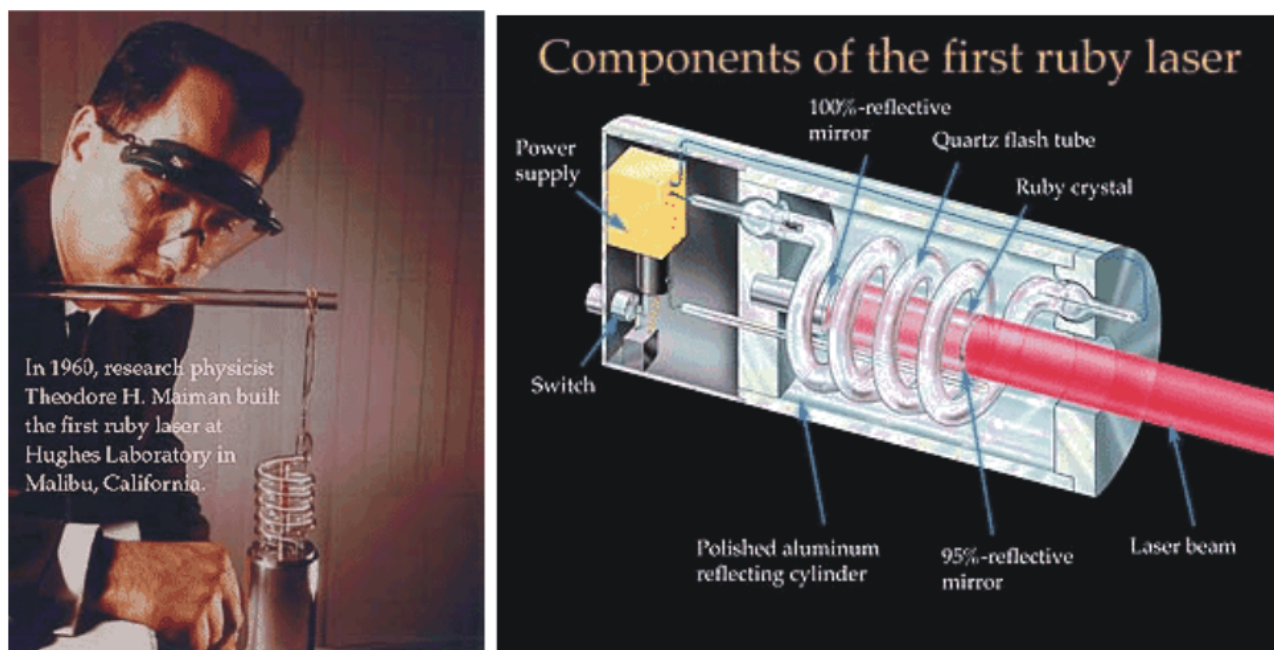


Figure 1.1: A cross-sectional view of the first Ruby Laser [28].

Bennet and Herriot created a gas laser using He-Ne (helium-neon) as an amplifying medium. In 1962, Hall invented the first semiconductor laser. Then, in 1966, Sorokin realized the first dye laser [29].

1.1.2 Basic principles of laser

The laser is a photonic component, based on light amplification by stimulated emission of radiation. Stimulated emission is an interaction between matter and light, where an already excited atom will emit two photons, completely identical after the absorption of a second photon. By multiplying the number of excited atoms in the amplifying medium, a beam of light is created with identical photons. Lasers emit radiation that is spatially and temporally coherent. A laser system is the sum of an amplifying medium, resonator and energy pumping source. The general principle of operation of a laser, illustrated in figure 1.2, can thus be summarized as follows: we feed a medium with a pumping source, this medium will emit a laser beam which will be reflected on the mirrors of a resonant cavity. The multiple reflections of the beam in the cavity participate in the amplification, by stimulated emission, of the beam.

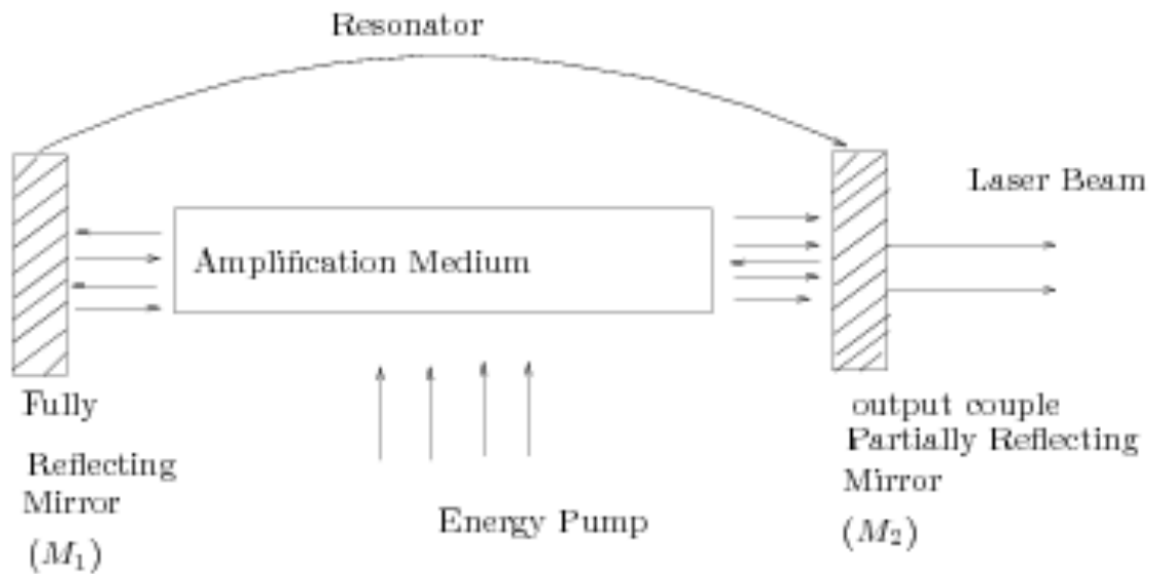


Figure 1.2: Schematic set up of Laser system [30].

The laser radiation is emitted by the output mirror which is semi-transparent.

1.1.3 The laser beam

Laser is just another source of electromagnetic radiation with very unique properties. For the best understanding of these properties, we can think about an ordinary source of light such as a burning candle or the sun. With an ordinary source of light the photon is emitted by spontaneous emission in all directions. In contrast, laser device emits photons, which are all concentrated in only one direction and this directivity has a consequence on the output power. If we take for instance an incandescent lamp (see figure 1.3, left), the power radiates will be distributed in all direction in the space and for that reason the power measure at a given point is low. However, for the laser all the power will be concentrated on a very small surface such that even with a low power laser, the power measured on that small surface will be considerable. The specific properties that make the difference between an ordinary source of light and light from the laser source are; monochromaticity, coherence, directionality, spectral brightness and operation regime (i.e. continuous-wave or pulse regimes). Indeed in continuous-wave regime, power is provided continuously over a given time while in pulsed regime, power is delivered in pulses of chosen duration over a given time.

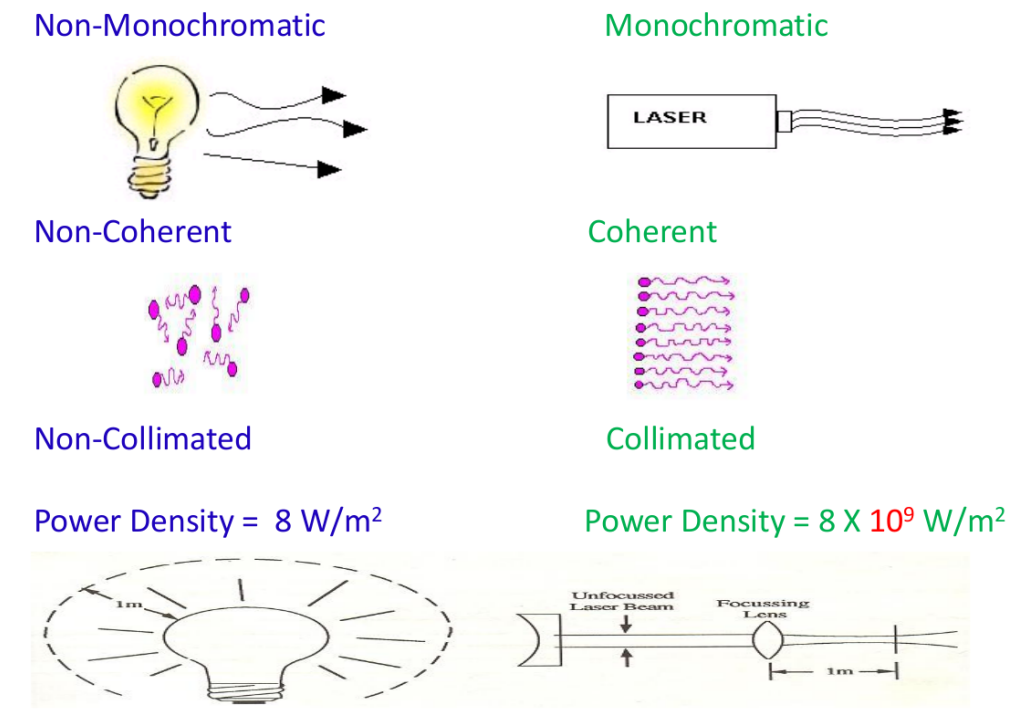


Figure 1.3: Comparison between ordinary light properties and laser light [31].

1.1.4 Different types of lasers and application

The different types of lasers can be classified according to the amplifying media used, gaseous, liquid and solid state lasers. Gas lasers are pumped using an electric current. The gaseous amplifying medium is then excited by collision with electrons. Among the most widely used are excimer lasers, argon lasers and CO_2 lasers. These are particularly used in industry for their high efficiency and allow the materials treatment. As for liquid lasers, more commonly known as dye lasers, the pumping is optical and uses arc lamps or other lasers, gas or solid state. These lasers use organic molecules in solvents, which must be changed regularly, and cover the entire visible spectrum. Finally, solid-state lasers fall into two families, electrically pumped semiconductor lasers (laser diodes) and optically pumped lasers using crystals or glasses. Laser diodes are particularly compact and highly efficient lasers that use stimulated emission to recombine electron-hole pairs in semiconductors that can be of various types (GaN, AlGaAs, etc.) depending on the desired wavelength, ranging from ultraviolet to near infrared. These lasers have two major defects: the spatial quality of the beams obtained is poor and it is not possible to use them in triggered mode. Other solid-state lasers use matrices, crystalline

or amorphous, doped with ions (Nd^{3+} , Yb^{3+} , Ti^{3+} , etc.) which enable a laser effect to be obtained. They are optically pumped by other lasers and emit in the red or near infrared. Lasers are used in various applications such as [32]:

- i) **In Medicine**, lasers are used to destroy kidney stones, to remove tumors successfully, to remove caries or decayed portion of the teeth, Lasers are used in cancer diagnosis and therapy.
- ii) **In Communications**, laser light is used in optical fiber communications to send information over large distances with low loss, in space communication, radars and satellites.
- iii) **In Industries**, lasers are used to cut glass and quartz, lasers are used for heat treatment in the automotive industry, for inscription on transparent materials and therefore offer a rich applications in ablation, marking and engraving.
- iv) **In Science and Technology**, a laser helps in studying the Brownian motion of particles, lasers are used in computer printers, lasers are used to measure the pollutant gases and other contaminants of the atmosphere.
- V) **In spectroscopic** lasers are used to characterize the materials. Indeed, figure 1.4 shown an example of Laser Induced Breakdown Spectroscopy approach where, a nanosecond laser Nd:YAG is used to identify a potassium, in the matrix Li_2CO_3 .

Progress in laser technology has made possible a wealth of micromachining processing applications, one of most currently popular ones being related to its use, is laser inscriptions on transparent material. This application in general rest on fundamental principles of Physics, particularly the theory of laser-material interactions which involves concepts of light propagation in materials.

In general, the nature of laser-material interaction in the femtosecond mode is fundamentally different from interaction with longer pulses (i.e. cw-lasers and nanosecond lasers) see for instance figure 1.5. Indeed, L. Rihakova *et al.* [18] and Sanjay Mishra *et al* [19], has investigated on different laser materials processing such as transparent Glass, Silicon, Polymers and Ceramics. They compared different results obtained with different type of lasers (i.e. nanosecond and femtosecond lasers) in the material processing and come out with the same

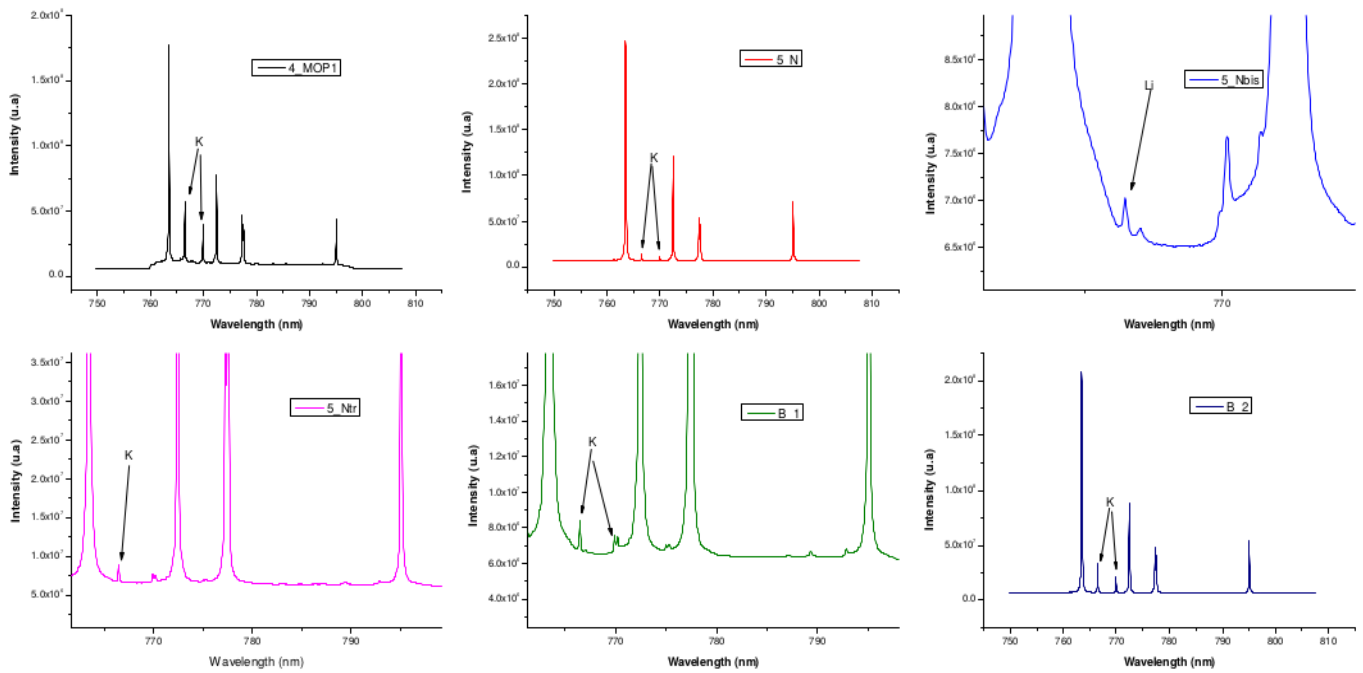


Figure 1.4: identification of a potassium, in the matrix Li_2CO_3 using LIBS approach.

conclusion that the femtosecond ($1fs = 10^{-15}$ s) laser was more suitable than the nanosecond laser for material processing.

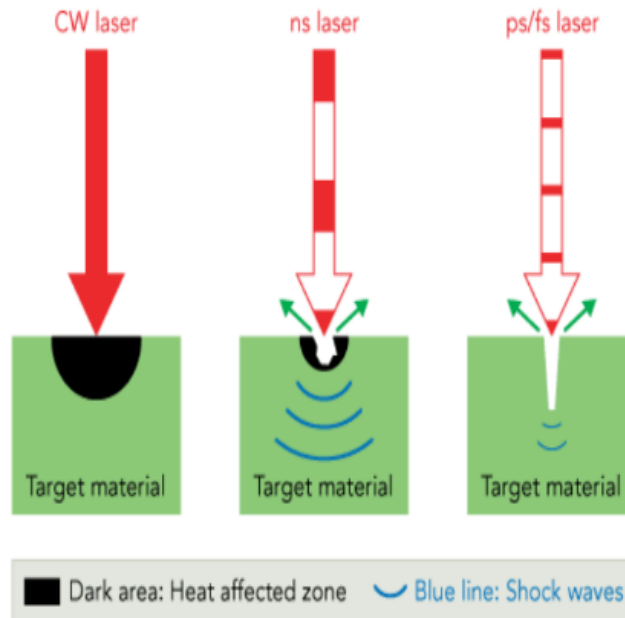


Figure 1.5: Comparison of damages produce by CW-laser, ns-laser and ps/fs laser on the transparent material [31].

As we have already stressed in our introduction, during the process of laser interaction with transparent material, the structures of materials are modified by the breaking of chemical bonds that causes the release of free electrons. These electrons usually form a plasma with variable density, and their interactions with photons composing the laser lead to relevant phenomena as for instance multiphoton absorptions, tunneling ionization, avalanche ionization and radiative recombinations [33]. However, to gain a good understanding of the physics behind laser inscription processes, it is useful to first understand all those phenomena generated in the transparent material.

1.2 Laser interaction with transparent material

Laser parameters and material properties have a significant effect on the interaction and therefore on the results of inscription. Laser energy, laser stability, repetition rate, laser wavelength, and pulse duration are several laser parameters that play a role in the absorption of laser pulses by the optical materials. Specific properties of materials, such as bandgap and thermal properties determine whether inscription with continuous-wave or femtosecond lasers is possible and how the resulting structures look and behave. The process by which energy from laser is absorbed by the material and the mechanisms by which the material responds, are the key to understand the laser material interaction.

1.2.1 Optical Kerr effect

The optical Kerr effect is a phenomenon in which the refractive index of a material changes because of an applied high intensity laser beam, and the change in the refractive index is proportional to the square of the electric field of the laser. The optical Kerr effect is best observed in materials known as Kerr mediums, centrosymmetric materials (e.g. fused silica). The optical Kerr effect plays an important role in the laser inscription process. To be more explicit it allows self-focusing of the laser beam in the material and therefore provides enough energy density to generate features on the material.

When the material is subjected to high laser intensity, the refractive index of this material does not depend only on the frequency ν of the radiation propagating through it, but also on its intensity I . In an instantaneous response medium, the polarization of the

medium can be developed in increasing power of the electric field [34]:

$$P_1(t) = \epsilon_0 (\chi^{(1)} E_1(t) + \chi^{(2)} E_1^2(t) + \chi^{(3)} E_1^3(t) + \dots) \quad (1.1)$$

Note that in this expression E_1 is the real field. If we consider a quasi-monochromatic wave of central frequency ω_0 then the real electric field is written as:

$$E_1(r,t) = \frac{1}{2} (\mathbf{E}(r,t)e^{-i\omega_0 t} + \mathbf{E}(r,t)e^{i\omega_0 t}). \quad (1.2)$$

$$\text{Defined } E(r,t) = \mathbf{E}(r,t)e^{-i\omega_0 t} \quad \text{and} \quad \bar{E}(r,t) = \mathbf{E}(r,t)e^{i\omega_0 t}, \quad (1.3)$$

and replacing equation (1.3) into (1.2) yields:

$$E_1(r,t) = \frac{1}{2} (E(r,t) + \bar{E}(r,t)) \quad (1.4)$$

In a medium that has an inversion center, it is shown that terms with even powers in the field cancel each other out [34]. The media that will be considered later falls into this category.

In the spectral domain, this non-linear response corresponds to a source term that will radiate waves at new frequencies. We retain in what follows only the components at the frequency ω_0 . The expression (1.1) is then written:

$$\begin{aligned} P_{\omega_0} &= \epsilon_0 \left(\chi^{(1)} E(t) + \frac{3}{4} \chi^{(3)} |E(t)|^2 E(t) \right) \\ &= \epsilon_0 \left(\chi^{(1)} + \frac{3}{4} \chi^{(3)} |E(t)|^2 \right) E(t) \end{aligned} \quad (1.5)$$

In general, we know that:

$$D_{\omega_0}(t) = \epsilon_0 E(t) + P_{\omega_0}(t) = \epsilon E(t) \implies P_{\omega_0}(t) = (\epsilon - \epsilon_0) E(t). \quad (1.6)$$

Knowing that $\epsilon = \epsilon_0 \epsilon_r$ and $n^2 = \epsilon_r$, equation (1.6) becomes:

$$P_{\omega_0}(t) = \epsilon_0 (n^2 - 1) E(t). \quad (1.7)$$

Utilizing equations (1.5) and (1.7) we obtain:

$$n^2 - 1 = \chi^{(1)} + \frac{3}{4} \chi^{(3)} |E|^2 \quad (1.8)$$

$$\text{hence} \quad n = \left(1 + \chi^{(1)} + \frac{3}{4} \chi^{(3)} |E|^2 \right)^{\frac{1}{2}} \quad (1.9)$$

setting $n_0^2 = 1 + \chi^{(1)}$, equation (1.9) becomes:

$$n = \left(n_0^2 + \frac{3}{4} \chi^{(3)} |E|^2 \right)^{\frac{1}{2}} \quad (1.10)$$

$$= n_0 \left(1 + \frac{3}{4n_0^2} \chi^{(3)} |E|^2 \right)^{\frac{1}{2}} \quad (1.11)$$

$$\approx n_0 \left(1 + \frac{1}{2} \frac{3}{4n_0^2} \chi^{(3)} |E|^2 \right) \quad (1.12)$$

Thus,

$$n = n_0 + \frac{3}{8n_0} \chi^{(3)} |E|^2 \quad (1.13)$$

Let's look at the meaning of $|E|^2$. In general, the power density in the medium or intensity I is obtained by calculating the time average of the Poynting vector $\langle \Pi \rangle$.

$$I = \langle \Pi \rangle = \langle E_1(r,t) \times H_1(r,t) \rangle \quad (1.14)$$

where,

$$E_1(r,t) = \frac{1}{2} (E + \bar{E}) \quad (1.15)$$

$$H_1(r,t) = \frac{1}{2} (H + \bar{H}) \quad (1.16)$$

For a plane wave we have the relationship:

$$H = n_0 \sqrt{\frac{\epsilon_0}{\mu_0}} E = n_0 c \epsilon_0 E, \quad \text{since } c = \frac{1}{\sqrt{\epsilon_0 \mu_0}} \quad (1.17)$$

Taking equation (1.17) into equation (1.16) reads:

$$H_1(r,t) = \frac{1}{2} n_0 c \epsilon_0 (E + \bar{E}). \quad (1.18)$$

Introducing equations (1.15) and (1.18) into equation (1.14) yields:

$$I = \frac{1}{4} n_0 c \epsilon_0 \langle (E + \bar{E})^2 \rangle \quad (1.19)$$

$$= \frac{1}{4} n_0 c \epsilon_0 \langle \mathbf{E}^2 e^{-2i\omega_0 t} + \mathbf{E}^2 e^{2i\omega_0 t} + 2|\mathbf{E}|^2 \rangle \quad (1.20)$$

$$= \frac{1}{2} n_0 c \epsilon_0 |\mathbf{E}|^2 = \frac{1}{2} n_0 c \epsilon_0 |E|^2 \quad (1.21)$$

This intensity is often expressed in W/cm^2 . It follows from equation (1.21) that:

$$|E|^2 = \frac{2I}{n_0 c \epsilon_0} \quad (1.22)$$

Replacing formula (1.22) into equation (1.13), we can then write the refractive index of the medium in the form:

$$n = \sqrt{1 + \chi^{(1)}} + \frac{3\chi^{(3)}}{4n_0^2 c \epsilon_0} I = n_0 + n_2 I \quad (1.23)$$

with:

$$n_0 = \sqrt{1 + \chi^{(1)}} \quad \text{and} \quad n_2 = \frac{3\chi^{(3)}}{4n_0^2 c \epsilon_0} \quad (1.24)$$

n_0 the linear index of refraction is dimensionless while n_2 the non-linear index of the middle is often expressed in cm^2/W . This changes in refractive index due to laser intensity is called the optical Kerr effect by analogy to the classic electro-optical Kerr effect in which the index of the material changes in proportion to the square of the applied static field. The coefficient n_2 is related to the third-order susceptibility of the material. This coefficient can be positive or negative, and its contribution to the total refractive index is no longer negligible when the material is exposed to a high peak intensity carried by ultra-short pulses in the case of fused silica material we have $n_0 = 1.45$ and $n_2 = 3.54 \times 10^{-16} \text{ cm}^2 / W$ [35].

As a summary of this subsection, we can say that, when the optical intensity inside the material is strong, the polarizability of the material change in response, leading to the modification of the nonlinear refractive index of the material. The phenomena which explain the nonlinearity in the laser is the Kerr nonlinearity. Actually, the Kerr nonlinearity affects the phase of an optical laser beam via the intensity-dependent refractive index $n = n_0 + n_2 I$. Here, n_0 is a linear refractive index of the bulk medium, n_2 is the nonlinear coefficient describing nonlinear self-modulation such that $n_2 I$ is a nonlinear contribution to the refractive index. In general, over the material length, the kerr nonlinearity on laser propagation in the material is defined by [36]:

$$Z_n = i \frac{2\pi n_2 L_{mat}}{\lambda_0 A_{eff}} |E|^2 E \quad (1.25)$$

where L_{mat} is the material length and A_{eff} is the effective area of the nonlinear medium. Because E is normalized to represent the laser power, $|E|^2/A_{eff}$ represents optical intensity of laser beam. We shall come back in a detail on this notion in chapter 2, while modelling the laser equation.

For a Gaussian spatial distribution of the laser pulse intensity, the central part has a higher intensity than the wings. According to equation (1.23), the centre section will see a

higher index (lower if $n_2 < 0$) than the other sections of the pulse. Thus, its propagation speed will be lower and the wave-front will bend as if it had passed through a converging lens. The effect of self-focusing is cumulative, which can lead to a catastrophic collapse of the wave-front on the optical axis. For self-focusing to be dominant, the wave-front must overcome the defocusing effect of diffraction. This condition is met when the peak power exceeds the critical self-focusing power [37]

$$P \geq P_{cr} \quad \text{where,} \quad P_{cr} = \frac{3.72\lambda_0^2}{8\pi n_0 n_2} \quad (1.26)$$

This parameter is valid for continuous-wave beams but is used as a reference for pulsed beams. When a laser pulse with a peak power greater than the critical power is focused by an optical element, the position of the wave-front collapse is generally located in front of the geometrical focus. However, other effects, such as dispersion and plasma formation, can influence the process. The cumulative effect of self-focusing by several slices of the pulse can also lead to filamentation [37].

However, when a laser pulse hits the surface of a material, it can be linearly or nonlinearly absorbed depending on the incident photon energies. If the laser energy is greater than the energy gap of the material, a single photon from the laser pulse will have sufficient energy to excite the electrons in the valence band and will allow them to move directly from the valence band to the conduction band of the material. In this case, the laser energy is said to be linearly absorbed. Actually, it has been reported that in some indirect bandgap semiconductors single photon absorption can also occur but this process requires assistance from phonon interactions [38]. On the other hand, if the laser energy is less than the energy gap of the material, the absorption is nonlinear meaning that several photons will simultaneously add up their energies to allow the electrons to be excited in the valence band to reach the conduction band. The two processes are well shown in figure 1.6.

We have already stress above that the material targeted by the current work is a transparent material and in general for such material, there is no linear absorption of the laser radiation. Therefore, in what will follow, we will be focused only on the case of nonlinear absorption. Indeed, there exist two classes of nonlinear absorption processes leading to the ionization of the irradiated material, they are the nonlinear photoionization and the avalanche or cascade ionization.

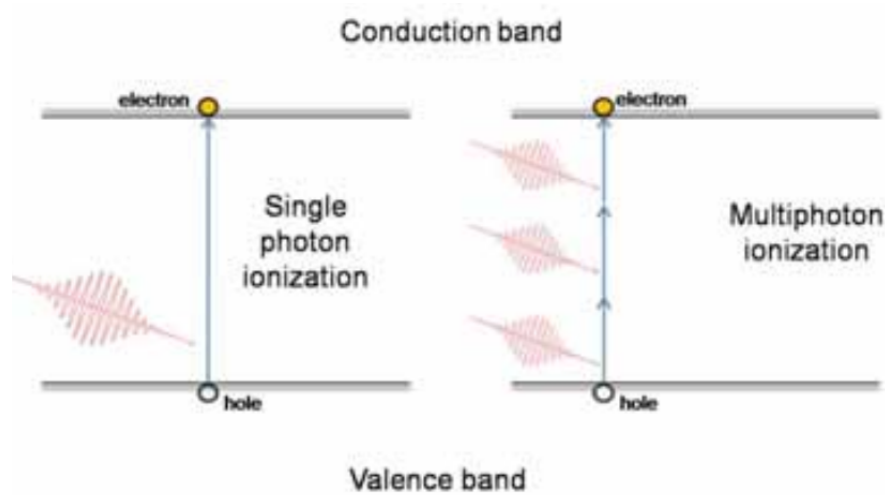


Figure 1.6: A schematic of single and multiphoton absorption of incident photons (shown in red) causing electrons to be promoted to the conduction band from the valence band. [38].

1.2.2 Photoionization

Photoionization is defined as a direct excitation of the electron by the optical field. As we already mentioned above, if a single photon of laser light does not have enough energy to excite an electron in a transparent material from the valence to the conduction band, multiple photons must cooperate together to excite the electron. Depending on the laser frequency and intensity, there are two regimes of Photoionization, namely, multi-photon ionization regime and tunneling ionization regime [39].

The adiabatic parameter γ , also known as the Keldysh parameter for the transition point between multiphoton ionization and tunneling ionization is defined as [40, 33]

$$\gamma = \frac{\omega}{e} \sqrt{\frac{m_e c n_0 \epsilon_0 E_g}{I}}, \quad (1.27)$$

where, ω is the laser frequency, I is the laser intensity at the focus, m_e is the effective electron mass, e is the elementary electron charge, c is the speed of light, n_0 is the linear refractive index and ϵ_0 is the permittivity of free space.

- ☞ At low laser intensity ($\sim 10^{13} - 10^{14} \text{ W/cm}^2$), with higher frequency (but not high enough that single photon absorption can occur), $\gamma > 1.5$ (Keldysh parameter). The Photoionization in this case is a **multiphoton ionization**. This mechanism of ionization occurs due to the simultaneous absorption of multiple photons by an electron in the

valence band. The number of photons K required to bridge the bandgap must satisfy $Kh\nu_0 \geq E_g$ [33], where E_g is the material bandgap, and ν_0 is the laser frequency. In the multiphoton ionization mechanism, the ionization rate is defined as $P(I) = \sigma_K I^K$ where σ_K is the multiphoton absorption for K -photon absorption while I is the optical field intensity.

- ☞ For high laser intensity ($> 10^{15} \text{ W/cm}^2$), with low frequency and $\gamma < 1.5$, the dominant mechanism, in this case, is a **tunneling ionization**. The strong field distorts the band structure and reduces the potential barrier between the valence and conduction bands. Direct band to band transitions may then proceed by quantum tunneling of the electron from the valence to conduction band. However, when $\gamma \sim 1.5$, the photoionization is a combination of tunneling and multiphoton ionization. The representation of those different processes can be observed in figure 1.7.

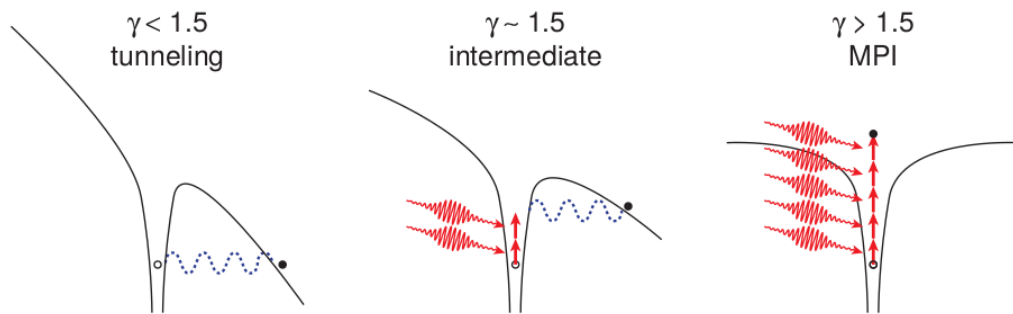


Figure 1.7: Diagram of the photoionization of an electron through tunnelling (left), multiphoton ionization (right) and both non-linear processes (central) with different values for Keldysh parameter γ [39].

1.2.3 Avalanche ionization and plasma generation

When a laser pulse with a high enough pulse peak intensity is focused into a material, the laser pulse transfers energy to the electrons in the valence band of the material and allows them to be excited and to reach the conduction band through nonlinear ionization. The free electron in the conduction band is accelerated by the electrical field of the laser from the conduction band minimum to higher energy levels of the conduction band, with an energy that allows it to collide

with other bound electrons. As long as the laser beam is present in the medium, the process will repeat itself and strong enough, giving rise to an electron avalanche as shown on figure 1.8. The existence of excited electrons in the conduction band is an initial condition required for avalanche ionization to occur. These initial electrons can be provided through multi-photon or tunneling ionization, ionized impurities or defect states, and thermally excited carriers [40, 39]. In this process, the electron density N , in the conduction band grows according to

$$\frac{dN}{dt} = \eta N, \quad (1.28)$$

where η is the avalanche ionization rate. Stuart et al. [40] developed a model of avalanche ionization in which the avalanche rate depends linearly on the laser intensity meaning that, $\eta = vI$, where v is the cascade ionization coefficient. Experimentally, it is shown that when

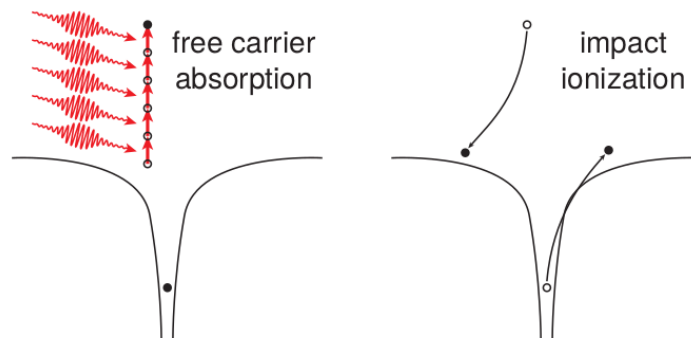


Figure 1.8: Schematic potential energy diagram for avalanche ionization (right), that follows after seed electrons are created by multi-photon absorption (left) [39].

the density of excited electrons in the conduction band reaches about 10^{29}cm^{-3} , a **plasma** is generated with a natural frequency that is resonant with the laser, leading to reflection and absorption of the remaining pulse energy [6]. The plasma generated expands rapidly in the opposite direction to the propagation of the laser beam. By reacting to the plasma relaxation effect, a shock wave then originates and propagates within the material. If the latter has a finite thickness, the shock wave can open with the relaxation of material towards the rear surface as shown on figure 1.9. The K -photon absorption and the avalanche ionization are responsible for the electron plasma generation.

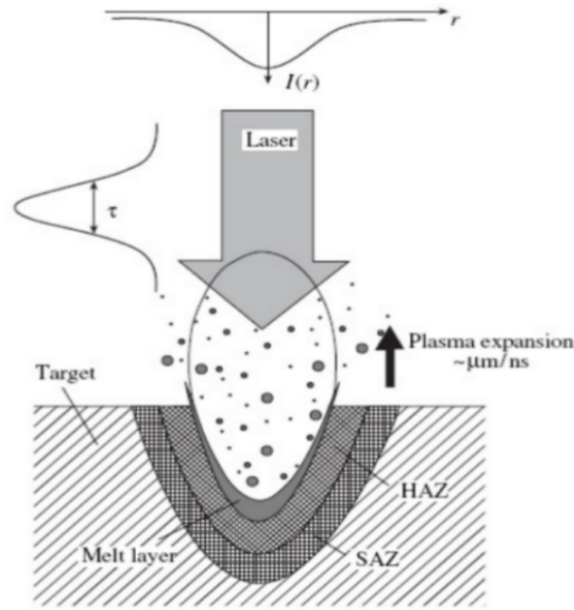


Figure 1.9: Plasma expansion by pulse laser. $I(r)$, spatial intensity distribution; r , radius; τ , pulse duration, HAZ is the heat affected zone, and SAZ is the shock affected zone [2].

1.2.4 Laser-plasma interaction

The plasma formed by this nonlinear ionization also affects the optical field propagation through absorption processes. The absorption of the laser field by the plasma is easily understood using the Drude model. In general, when the plasma density grows and its frequency [33]

$$\omega_p = \sqrt{\frac{Ne^2}{\epsilon_0 m}} \quad (1.29)$$

reaches the laser frequency, then the absorption of the optical field by the plasma becomes very important. The absorption coefficient in this case is given by:

$$\Gamma = \frac{\omega_p^2 \tau}{c(1 + \omega^2 \tau^2)} \quad (1.30)$$

where ω is the laser frequency, and τ the phenomenological Drude scattering time (usually around 0.2 fs) [40]. In addition to the fact that the plasma generated during the propagation of the laser beam in the transparent material is absorbed at high density, it can also have defocusing effects on the laser pulse as shown on figure 1.10. This is because the free electrons that constitute the plasma contribute negatively to the refractive index of the medium (Kerr effect). This plasma de-focusing is the process that arrests self-focusing and perturbs the

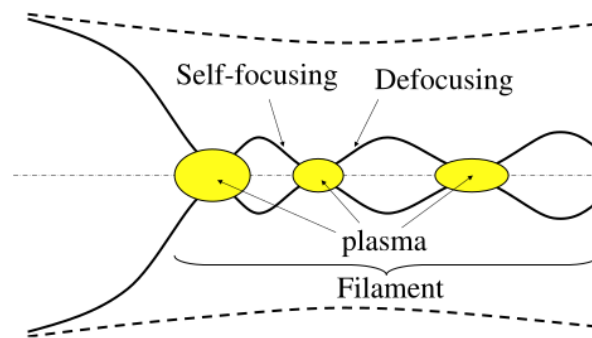


Figure 1.10: Schematic representation of the focusing-defocusing cycles undergone by the intense core of the beam [9].

laser signal (intensity clamping) [41]. Therefore becomes a relevant issue when laser is utilized in the inscription processes.

The physical mechanism generated during the laser-material interaction are summarized on figure 1.11.

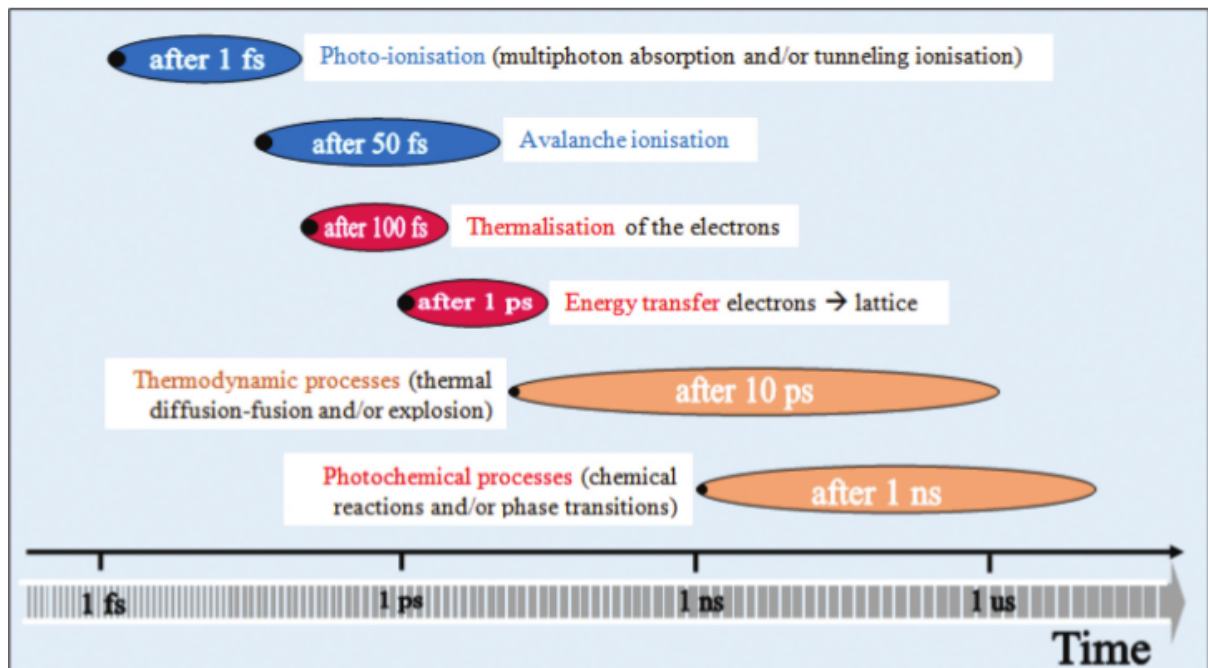


Figure 1.11: Occurrence of different physical phenomena during different timescales involved in laser-material interaction [42].

1.3 Generality on laser inscription: marking and engraving

Laser inscription, plays a significant role in modern industries where it is used to imprint characters, images, symbols or to leave mark on an object. Indeed laser inscription is a process in which the laser is use to engrave or mark a material from the top surface down to a specified depth. Actually, a number of different techniques have been utilized to mark different materials, e.g mechanical engraving, hot stamping, serigraphy, manual scribing, photo-lithography and etching. Some of these techniques are using inks or tool bits to mark the material. The disadvantages of this method is that when inscription is done with the tool bits, there is contact with the inscribing surface. According to the marking techniques with the inks, the issue is that the material's surface needs to be prior degreased to the ink-print process, and it takes much time to dry the ink on the material's surface. However, the technique of laser inscription does not include the use of inks, nor does it include tool bits which contact the inscribing surface and wear out. This offers a wide range of advantages over above mentioned traditional method where inks or bit heads have to be replaced regularly [43]. The arguments in favour of inscription by laser are strong meaning that, it is a technique fast, flexible, made inalterable, high degree of accuracy and the smoothness of the features, high precision, the possibility of inscribe at difficult to reach places, and the fact of being to engrave fragile materials such as ceramic, glass etc. [44]. Moreover, laser inscription process is also used to produce indelible alpha-numeric characters and logos for the purposes of product identification and traceability. Because of these applications, lasers inscription have attracted much attention in many industries sectors as for instance; microelectronics industry, glasses industry, medical industry, photonic industry and so on.

1.3.1 Methods of laser inscription technologies

Indeed, there are two different methods for laser inscription namely; inscription through mask and inscription via beam deflected method.

Mask Inscription method

In general, mask inscription method uses masks to engrave alpha-numeric characters on the material. This mask is made by the metal or dielectric coating deposited onto a glass substrate [45]. This contains all the information to be engraved on the material. Figure 1.12 is an example of mask engraving system used to engrave "A" letter on the workpiece. One of the

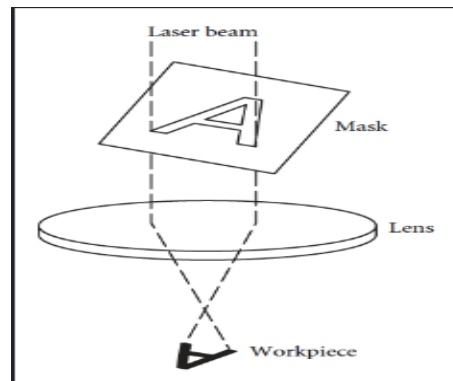


Figure 1.12: An Example of mask inscription system [46].

advantages of using mask inscription system to engrave the material is that a large quantity of material can be engraved at relatively high speed with high repeatability, provided that the engrave information stays the same. However, a disadvantage of this system is that it requires expensive masks that should be fabricated to suit different messages. Furthermore, changing the messages requires the changing of masks, and large engrave surfaces or long information to be engraved on the material require multiple pulses, which reduce throughput [47, 46, 45].

Laser beam deflected Inscription method

For the inscription with laser beam deflected method, a computer is used to move a worktable or a set of galvanometer mirrors to scan a focussed laser beam over the surface of the material. In this process, the computer plays a role of turning the laser on and off as required by the information being engraved. According to the fact that the work-table or the galvanometer mirrors are computer driven, messages can be changed from one to another quite easily. Graphics and characters with multiple fonts, sizes, orientations and rotations can all be combined into one inscription process. However, in this method, inscription is done either in the dot-matrix mode utilizing a raster scan (see figure 1.13), or in a vector scan mode (see

figure 1.14) [47, 48]. To be more specific, for the inscription in the dot-matrix or raster mode,

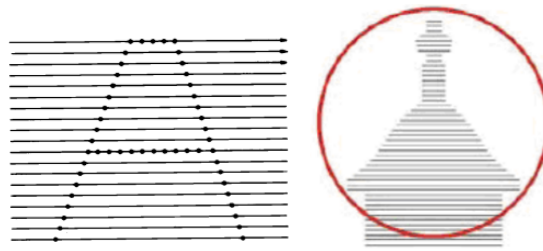


Figure 1.13: Engraving using raster or dot matrix inscription [48, 49].

the laser beam moves sequentially in rows on the material. This method is usually used mainly for engrave alpha numeric information, and it is less appropriate for graphic images. However,

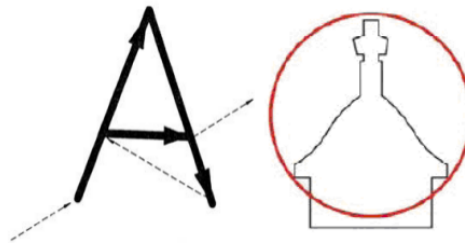


Figure 1.14: Engraving via vector inscription method [48].

in vector inscription method, the marks are imprint by focused laser radiation on the target material, which in turn is guided by an optical system and operated by a computer program. Vector engraving method can be applied to all types of information such as: numeric-code, bar-codes (i.e 1D and 2D codes, see figure 1.15), logos, and almost any other kind of image as well as characters [50]. This is the most common and versatile method of lasers inscription.

Figure 1.16 represent the laser inscription machine



Figure 1.15: Engraving of bar-codes: a) 1D; b) 2D [51, 52].

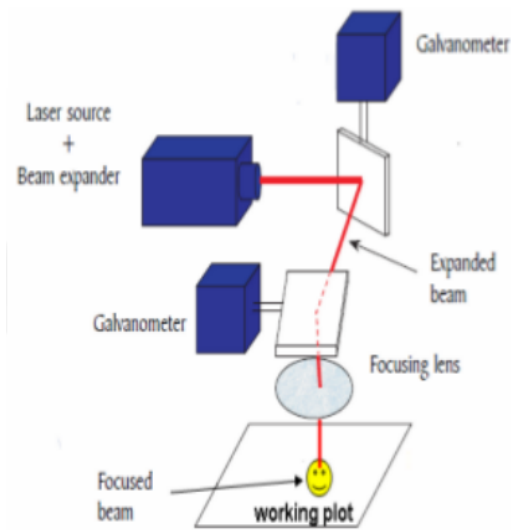


Figure 1.16: An example of beam deflected inscription system [48].

1.3.2 Inscription criteria and mark legibility characteristics

There are many parameters which affect both the ability of material inscription and the speed at which it can be engraved. One of the important key consideration of this technology is how well the material being inscribed absorbs the laser radiation. This can be determined by the type of laser used as different wavelengths can have different absorption characteristics. If the laser light is transmitted or reflected, then engraving becomes more difficult or even impossible. For optimum results the focussed laser beam has to be absorbed in the top few microns of the material surface, so that sufficient energy density is produced to modify the material surface. It is reported that, Metals reflect CO_2 laser radiation and therefore cannot be engraved by CO_2 lasers [53]. An absorbent coating will enable engraving by a CO_2 laser, or alternatively a solid-state laser can be utilized. Some polymers transmit CO_2 laser beam and cannot be engraved, and therefore it is necessary to include additives in the polymers [49], which absorb the radiation or to use a laser with a different wavelength as for instance Nd:YAG laser or femtosecond laser. However, If a material surface has a varnished coating the laser light has to remove the varnish before it can engrave the surface, and this will require a higher energy density.

Although, the quality of the mark on the material surface is assessed by its legibility characteristics such as mark contrast, mark width, mark depth, spattering, and microcracks

[3, 54, 55]. The level of acceptance of these different characteristics generally depends on the manufacturer's requirements [47].

Mark width

This denotes the width of the line segment that forms a character. With the mask image inscription, the mark width in the characters is essentially determined by the mask geometry and the lens imaging quality. It can be as small as a few micro-meters, which can only be read under a microscope. In deflected inscription method, the line width is mainly determined by the focused beam spot size [56]. Other parameters such as scanning speed, power density and material properties also affect the line width. In general, a toolmaker's microscope or Talysurf surface texture measuring equipment are used for the line width measurement.

Mark depth

The Engraving depth depends on energy volume density, materials properties and the laser-material interaction time. In mask inscription process, the vaporization depth is often determined by the thickness of paint or oxidation layer. It is typical of few microns to several tens of microns. In deflected laser inscription method, greater depth penetration into the material can be achieved varying between a few microns to several tens of millimeters. A further enhancement of the effect on the material can be realized by supplying gases such as oxygen or compressed air, which assist material removal. It has been reported that, with mask inscription method, the depth of penetration ranges from 1 to $10\mu\text{m}$ [57, 58], while with the deflected inscription method, the depths mark of about $25\mu\text{m}$ to 0.25mm have been reported [57]

Mark contrast

The mark contrast is define as a visual difference between the apparent brightness of the marked surface and unmarked surface of a material. The sharpness or resolution of the marked edges affects the engraving contrast [45]. This parameter is particularly important in bar code engraving, as poor edge sharpness may fail bar code reader. High peak power or power density produces better edge resolution.

Spattering

Spattering is characterized by the presence of resolidified streamers and droplets of surface material in the vicinity of the engravings, resulting probably from the powerful vaporization forces generated during the inscription process. This is undesirable, as it distorts the boundary of the mark, giving the lettering poor line definition and, therefore, poor mark legibility [59]. Spattering can be assessed as an attributable entity whereby ratings are used to associate the degree of spattering effects for each marking. One can rate the spattering effect either visually or through the use of an optical microscope.

Microcracks

The microcracks are created by the presence of tensile stress during the inscription process when a material is cooled rapidly from a molten state to a solid state. This is undesirable characteristics that affect the mechanical properties of the material. Moreover, this may induce corrosion-related failures into the material, thereby impairing the mark legibility as well as the reliability of the material [59]. Microcracks can be evaluated using either scanning-acoustic microscopy (SAM) or scanning-electron microscopy (SEM). Figure 1.17 shows the presence of microcracks in a marked line.

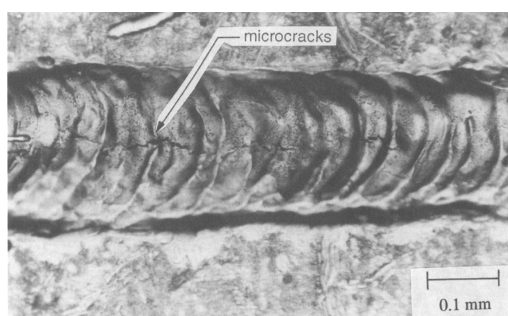


Figure 1.17: Microcracks along a line generated by a Nd:YAG laser on a plastic leadless chip carrier covered with a gold-nickel lid; with pulse energy of 0.1 J, pulse duration of 0.6 ms, argon as the assist gas, gas pressure of 0.2 MPa, lens focal length of 150 mm, focal position of 0.1 mm away from the material, and percentage overlap of 85% [59].

1.3.3 Important inscription parameters

The effectiveness of laser engraving also depends on the following parameters: the energy density, interaction time, material properties, focussing lens, spot size, pulse repetition frequency and the inscription speed.

Power density, energy density and lasers material interaction time

The power density, q_s , is defined as the average incident laser power at the material, P , divided by the focussed area, S_0 [60, 61]:

$$q_s = \frac{P}{S_0}. \quad (1.31)$$

The energy density or laser fluence, F , refers to the amount of laser energy radiation falling onto the surface of the specimen and is determined from [60]:

$$F = \frac{E}{S_0} = \frac{P}{S_0}T \quad (1.32)$$

where E is the amount of laser energy incident on the material and S_0 is the area of the focussed beam. For a fixed amount of input energy to the material, it has been found that the depth of penetration varies directly with the energy density of the beam [60]. For mask marking the focussed area is about $0.36 - 1.6\text{cm}^2$ while for beam deflected inscription method the focussed area is about $2.5 \times 10^{-5}\text{cm}^2$ [62]. However, the time of the impact of the laser radiation on the material also has a significant influence on the quality of engraving and the penetration depth of the incoming laser beam in the material. It is related to the power density, q_s , as:

$$T = \frac{F}{q_s} \quad (1.33)$$

where T is the time interval over which the laser pulse interacts with the material. The interaction time is inversely proportional to the beam speed and affects the ease of engraving and mark depth, as it determines the speed of heat transfer, phase changes, and any chemical reactions that may occur. If the energy is dissipated over a long duration, mark contrast can be effected by pigment discoloration. As the interaction time is decreased, mark contrast can be obtained through phase change by melting and resolidification, foaming, vaporization of surface area, and spattering of matrix materials [63].

Focussing lens and spot size

The quality and focal length of the focussing lens and the relative position of the laser beam with respect to the material are other important parameters in laser engraving. Highest power density is obtained if the focal position is at the lens focal point (i.e the spot size is small). In general, the wavelength, beam divergence and quality of optics has an important effect in determining how small a spot size can be on the material surface. The spot diameter d_{spot} is given by [48]:

$$d_{spot} = M^2 \frac{4\lambda}{\pi} \frac{f}{D}, \quad (1.34)$$

where f , is the focal length, D the laser beam diameter and M^2 a parameter defining the quality of the beam. However, the spot diameter d_{spot} (see figure 1.18), is related to the focal length and the beam divergence by $d_{spot} = f\theta$ [59]. The spot size or the focussed area increases

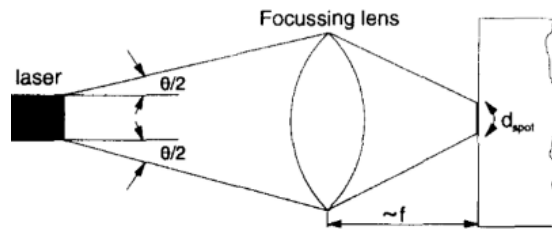


Figure 1.18: View of the spot diameter of the laser beam on the transparent material [59].

as the focal position is shifted away from the focal point. This means that, as the focussed area increases, the power density decreases [60, 64]. The focussed area of the laser beam as shown on figure 1.18, can be computed as:

$$S_0 = \frac{\pi}{4} d_{spot}^2. \quad (1.35)$$

Figure 1.19 illustrates the effect of spot size by increasing the lens focal length [65]. For constant output energy and pulse duration, increasing either the focal length or the beam divergence will result in a lower laser power density, as the focussed area is increased. In principle, the pulse duration and the pumping level do not affect the size of the focussed area.

Inscription speed and laser repetition rate

In the context of laser beam deflected inscription, engraving speed is defined as the linear speed of the laser beam whereas in the mask inscription, engraving speed is defined as the total

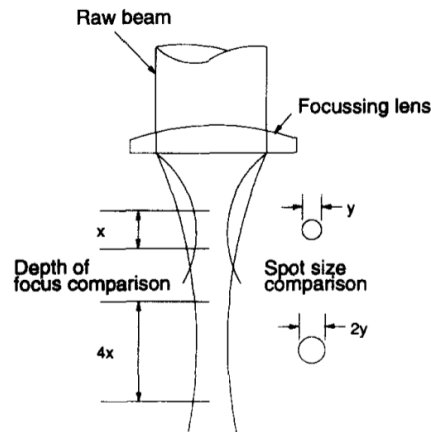


Figure 1.19: Effects of increasing the lens focal length [65].

number of material that can be engraved in 1 s. The repetition rate is the pulse frequency of the laser. In mask inscription, a typical engraving speed is about 8 to 20 materials per second, while in deflected inscription, the engraving speed is about 5 to 15 characters per second or about 400 mm/s [45]. Usually, the overlap region is used to ensure that the marks are visually continuous (see Fig. 1.20) on the material. The laser beam speed movement on the material

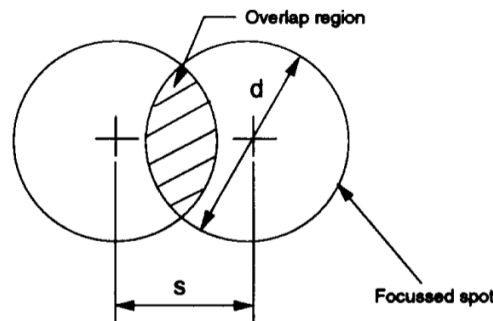


Figure 1.20: Effects of increasing the lens focal length [65].

is related to the percentage overlap and the repetition rate as follows:

$$v = d \left(1 - \frac{\text{percentage overlap}}{100} \right) \times \text{pulse repetition rate} \quad (1.36)$$

where,

$$\text{percentage overlap} = \left(1 - \frac{S}{d} \right) \times 100 \quad (1.37)$$

with d the spot size and S the centre-to-centre spacing between the pulsed spots [65].

Optical and thermal properties of the materials

During the lasers material-inscription, there can be either Fusion and Ejection, Vaporization, or Ablation of the material. These depend mainly on the material properties and laser parameters. The mechanism of material removal in laser engraving is the result of the laser absorption by this material. The absorption coefficient (α_n) of the material controls the decay of laser intensity with depth inside the material [19]. The absorption coefficient depends on the temperature and wavelength but at constant α_n , decay of laser intensity with depth is given by Beer-Lambert Law as, $I(z) = I_0 e^{-\alpha_n z}$ where I_0 is the input intensity at the surface of the material after considering reflection losses. The depth at which the intensity of the laser drops to $1/e$ value of its initial value at the interface is known optical penetration or absorption depth (δ_n) given by $\delta_n = 1/\alpha_n$. Laser radiation is absorbed either by exciting free electrons or by electronic or vibrational transitions in atoms, ions, or molecules. Electronic or vibrational states may be localized or non-localized and may be related to the solid surface, defects and impurities.

The absorptivity of a given material depends on its reflection and transmission characteristics. The absorptivity, transmissivity and reflectivity are inter-related by [45]:

$$a_n + r_n + \tau_n = 1, \quad (1.38)$$

where a_n is the absorptivity, r_n is the reflectivity and τ_n is transmissivity of the material. Indeed, the absorptivity is affected by material properties, surface condition, wavelength and surface temperature, as established by Bramson equation [60]:

$$a_n = 0.365 \left(\frac{T_e}{\lambda} \right)^{0.5} - 0.0667 \left(\frac{T_e}{\lambda} \right) + 0.006 \left(\frac{T_e}{\lambda} \right)^{1.5}, \quad (1.39)$$

where T_e is the temperature dependent electrical resistivity (Ωm), and λ is the laser wavelength. From equation 1.39, one can conclude that the absorptivity of the material surface increases with temperature. The thermal properties of the material are defined by the specific heat per unit mass, C_v , the mass density, ρ_n , and the thermal conductivity, Γ_n . These are related to the thermal diffusivity, κ_n by [45]:

$$\kappa_n = \frac{\Gamma_n}{C_v \rho_n}. \quad (1.40)$$

This thermal property determine the depth and the total volume of the material that undergoes thermal transformations. It is reported that, for a constant uniform irradiance, the thermal

penetration depth, L_{max} , is given by [60]:

$$L_{max} = \sqrt{4\kappa_n t_d}, \quad (1.41)$$

where t_d is the pulse duration.

1.3.4 Marking and engraving transparent materials

Laser marking discolors the surface of the material, while laser engraving actually removes a portion of the surface area as it marks see figure 1.21. Laser marking most commonly takes

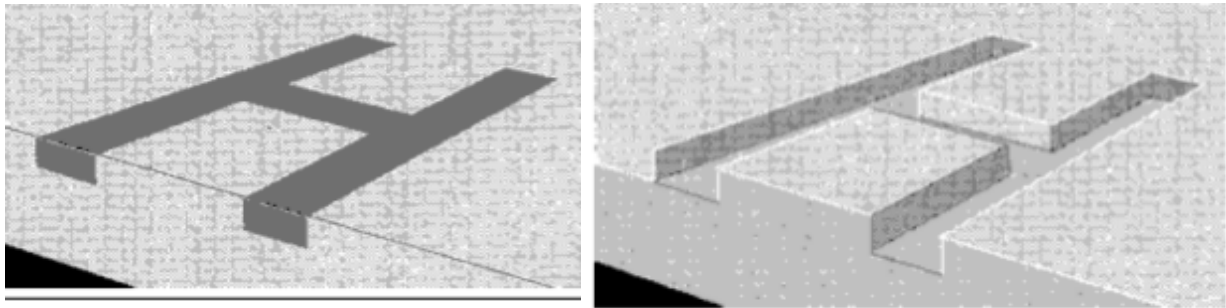


Figure 1.21: Laser marking (left) and laser engraving (right) [47].

the form of an alphanumeric code imprinted on the surface of the product to indicate the date of manufacture, best-before, serial number etc. Laser used in marking process are nanosecond lasers. In laser marking, the mark is generated on the material by the thermal process and it is possible to realize physical processes such as heating, vaporizing, melting or annealing. Each has a specific effect for different marking applications. Heating induce crack or micro-crack around the mark, vaporization produces a mark with depth in the material, like engraving.

Although, the labelling of glass is an important processing step for the medical sectors that allows tracing and controlling of their products. The traditional techniques, i.e. colour bar codes or labels, have several disadvantages, e.g. lack of permanency and susceptibility for tampering, limited adhesion and problems during sterilization [66]. Therefore, the unique recommended treatment of the glass used in medicine is the laser engraving. Actually, materials processing technology by using laser irradiation for glass engraving presents two principal aspects, namely the purely decorative side and the aspect of traceability or identification products. These makes it possible to include in a permanent way of the job numbers, matrix code of date or any important information on parts and articles [44, 67]. In general, glass

is a difficult material to mark at certain wavelengths because of its transparency and ability to reflect the laser radiation during the inscription processes [68]. The CO_2 laser and the femtosecond laser are suitable for glass inscription. Indeed, for the wavelength of the CO_2 lasers (i.e. $10.6\mu\text{m}$), glass is very absorbent. This is due to silica present in this material. Moreover, it has been reported that for glass, one notes 94% of absorption with the CO_2 lasers at the wavelength of $10.6\mu\text{m}$ [44].

A) Marking on transparent Ceramic

Nood *et al* [45], has investigated on the marking of transparent Ceramic (i.e. alumina corundum, Al_2O_3). They reported that marking via inscription process are found to be caused mainly by phase transformation, melting and resolidification, vaporization or explosive vaporization.

Phase transformation: Some materials undergo phase changes, from a polycrystalline phase to a crystalline phase, when laser treated to just below the melting point in air, e.g. alumina corundum (Al_2O_3) [69, 70]. Upon cooling, the grains grow in a preferred orientation [71], mark contrast being achieved from the differences between the orientated grains and the base material. Figure 1.22 shows a cross-sectional view of an Al_2O_3 substrate showing the phase changes after it has been laser treated in air. Other ceramic materials may undergo

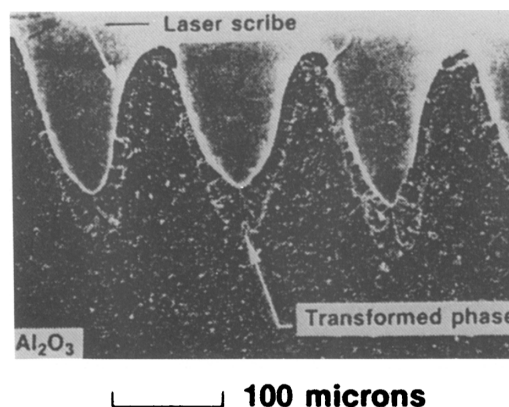


Figure 1.22: Cross-section of laser scribed Al_2O_3 substrate in air [72].

phase changes from the polycrystalline phase to the amorphous phase when laser treated in air or vacuum, giving the marked surface a glassy appearance, e.g. silicon nitride (Si_3N_4) [72].

Melting and resolidification: In this process, the surface temperature of the ceramic is raised just to its melting point and the material on the surface is then allowed to solidify, the result being a series of overlapping pools of resolidified material (usually of different phase) [59]. Visual contrast stems from the difference of reflection between the overlapping pools and the background area. The advantages of this technique include: no material removal, no debris generation, and minimum thermal stress introduced into the ceramics.

Vaporization: Vaporization produces visual contrast by physically removing surface material, contrast resulting from differences in colour, reflectance, or texture, or by the casting of shadows. When very high laser beam intensities are used, an explosive loss of material as well as vaporization may occur. In explosive vaporization, molten material is ejected in tiny droplets. Some of these droplets settle in the neighbourhood of the exposed area. The result is deep marks with ridges, burrs or spatters along the markings, which give good visibility but may not be acceptable in terms of mark quality (see Figure. 1.23). Microcracks may form along the markings, being produced by tensile stresses which result when the ceramic material is cooled rapidly from a molten state to an amorphous solid state.

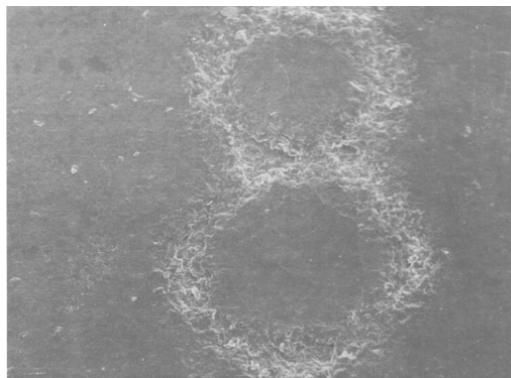


Figure 1.23: Vaporization effect of a letter "8" marked on a ceramic package using Nd:YAG laser [59].

J. Peter *et al.* [73] has investigated on the analysis of Nd:YAG laser marking process parameters. They studied for instance the effects of pulse frequency on various laser marking characteristics like mark width, mark depth and mark intensity (see figure 1.24), on alumina ceramic. According to figure 1.24 (left), the authors concluded that the mark width decreases with the increase in the pulse frequency and that also, increase in the pulse frequency, the spot

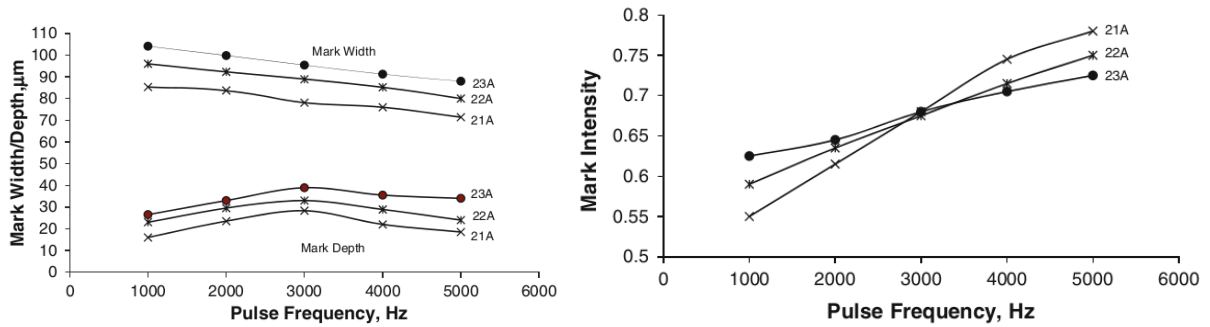


Figure 1.24: Effect of pulse frequency on mark width and depth with different lamp current (left) and Effect of pulse frequency on mark intensity with different lamp current (right) [73].

size decreases which lead to finer marking. In this same figure 1.24 (left), they represented the mark depth as function of pulse frequency too and concluded that, mark depth increases gradually for lower values of pulse frequency but decreases for higher values of pulse frequency. In general, the high peak power pulses at low frequencies will increase the surface temperature very rapidly resulting in material vaporization and minimal heat conduction into the part. But when the frequency increases the peak power is not sufficient to melt the material. Hence a part of the material stays inside owing to reduction in the depth of the mark. Equation (1.42) gives the relation between the average power and the peak power.

$$\text{Peak Power} = \frac{\text{Average Power}}{\text{Pulse Frequency} \times \text{Pulse Duration}} \quad (1.42)$$

With respect to the effect of pulse frequency on the mark intensity, the authors has shown on figure 1.24 (right), that as the pulse frequency increases, the mark intensity increases in a very steep manner. In addition to this, they mentioned that, as the pulse frequency increases, the peak power decreases which cause less material removal and less thermal damage, which creates a clean surface thereby resulting in an increase of mark intensity.

B) Engraving on transparent glass

The reason for which researchers are currently investigating on laser glass engraving are: the identification of microcracks in the mass of the material and the depth, shape and dimensions of craters induced by laser [20, 74]. The studies that will improve research in this field will have to establish the admissible dimension of the microcracks and the craters that may appear

in the mass of the material after the laser inscription operation has been carried out. In general, engraving on the glass is the result of the generation of a succession of small cavities appearing in this material during the inscription processes. This induced cavities as a result of laser inscription on the glass is regulated by the reaction effect of pressures, i.e. vapour pressure and gravitational pressure. A cavity is formed when the vapour pressure exceeds the gravitational pressure, according to the findings in reference [74]. In practice, these phenomena, which occur as the laser beam intensity increases, define the stages of cratering in the mass of the glass material. Knowledge of the shape and dimensions of craters is very important to evaluate the quality of the fineness of the character printed on the glass materials [75].

We have already said above that during the interaction of the laser beam with glass materials craters and cracks in the material structure are formed. These are visible with the naked eye, and some microcracks are visible with the microscope. For the best understanding of how microcracks are generated on the surface or in the bulk of the transparent glass material, it is important to study in depth the thermal, physical and chemical phenomena that occur in the process of laser glass inscription [66, 76]. Figure 1.25 shows the laser treatment of glass surfaces followed by microscopic observation of samples with microcracks in the area adjacent to the engraving.

Actually, when the laser beam is applied to glass surfaces with short pulses duration, small craters appear. The quantity of material melted and evaporated over the duration of a laser pulse is of the order of milliseconds. This depends largely on the laser parameters and the nature of the material. Surface engraving is defined as repeated passes of the laser beam over the surface being treated. The appearance of the engraved surfaces is influenced by the shape and the dimension of the crater induced by laser. In [20], the author has shown from an experimental design that the shape of craters changes significantly from one case to another according to technological parameters. In order to observe the evolution of the shape of the crater at sight in the section and the quality of the resulting engraved surfaces, the author had described the effects of the action of laser parameters on the glass surfaces being engraved and presented the results on figure 1.26. These results represent a synthesis of the descriptions of the shape and dimensions of the resulting craters as a function of certain parameters.

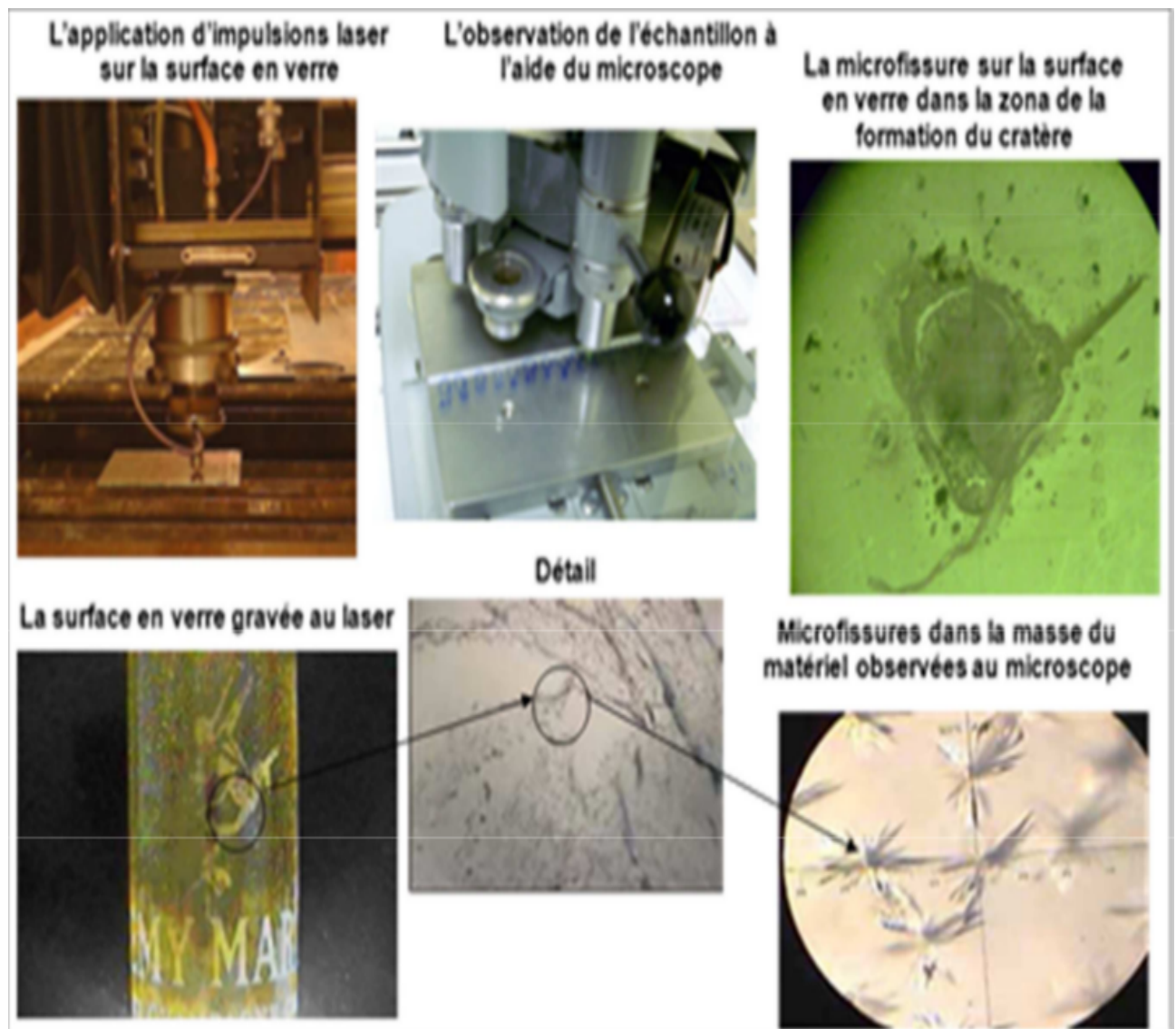


Figure 1.25: Microscopy observation of the microcrack induced by the laser in the glass float around the engraved zone [20].

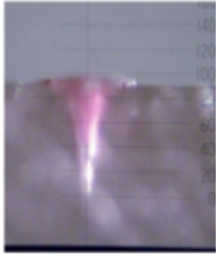
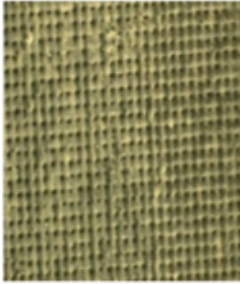

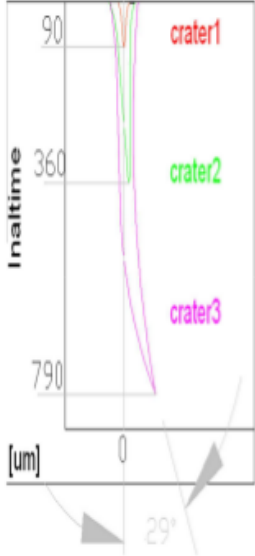

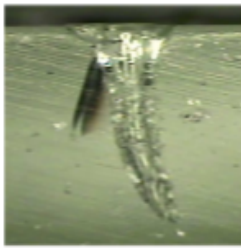

Valeur des paramètres Laser	Vue en section du cratère	Description des dimensions et de la forme du cratère	L'aspect des surfaces gravées	L'évaluation des surfaces
<p>P= 60 W $t_i = 0.6$ ms N°. Imp.=1</p>	<p>Cratère 1</p> 			<p>La surface gravée est très bonne</p>
<p>P =180 W $t_i = 0.6$ ms N°. Imp.=3</p>	<p>Cratère 2</p> 			<p>La surface gravée présente du matériau en excès dans la zone supérieure des cratères</p>
<p>P = 210 W $t_i = 0.6$ ms N°. Imp.=10</p>	<p>2Cratère 2</p> 			<p>La rugosité de la grande surface (Ra=30,49µm) et grande quantité de matériau en excès dans la zone supérieure des cratères</p>

Figure 1.26: Description of the effects of the laser parameters on the glass float surface engraved with CO_2 laser in the continuous-wave regime ($\lambda = 10.6\mu\text{m}$ and the maximum power $P = 60\text{W}$) [20].

Data matrix code engraving on transparent glass

The importance of laser engraving with high quality and precision on the glass is beneficial to the engraving of matrix codes. The data matrix offers the possibility to store a clearly defined amount of product information on a relatively small area. Researchers such as Dumont *et al* [66], have studied the quality of matrix code engraving on the glass material in pulse regime. Their objective was to observe the aspect of the matrix code which can be optimized by the optimal setting of the technological parameters such as; the laser power and the number of pulses. In the realization of these types of codes of high complexity and size, the use of laser inscription in pulse regime has been very flexible and effective. Figure 1.27 shows the glass engraving of a matrix code that is similar to the ideal model shown on the left side of the figure. The code was engraved by laser inscription with the wavelength $\lambda = 10.6\mu\text{m}$ with maximum power of $P = 1500\text{W}$ [20, 66]. In the composition of the matrix code, each laser pulse represents a pixel. On the right side of the figure 1.27 we can see the appearance of the craters formed by the laser pulses at different degrees of increase. The depth, the dimension

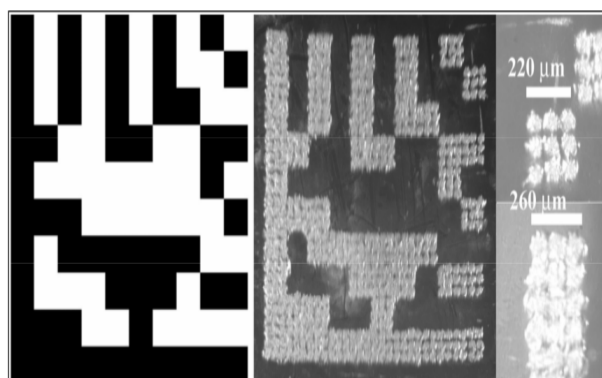


Figure 1.27: Data matrix engraved on glass material with CO_2 laser operating in pulse regime using wavelength of $10.6\mu\text{m}$, with a fluence of $7\text{J}/\text{cm}^2$ and 10 pulses [20].

and the shape of the craters formed in the glass during the laser inscription on this material are one of the key criteria for the appreciation of the qualitative aspects of laser engraving on glass. Figure 1.28 represented the engraved of the matrix code on the clear glass material when the craters generated in the mass of the glass are inhomogeneous. The authors of this work [66], presented on figure 1.28, reported that this unacceptable results is due to the fact that the applied ArF excimer laser energy (i.e. $F = 0.95\text{J}/\text{cm}^2$) was not high enough to engrave this material.

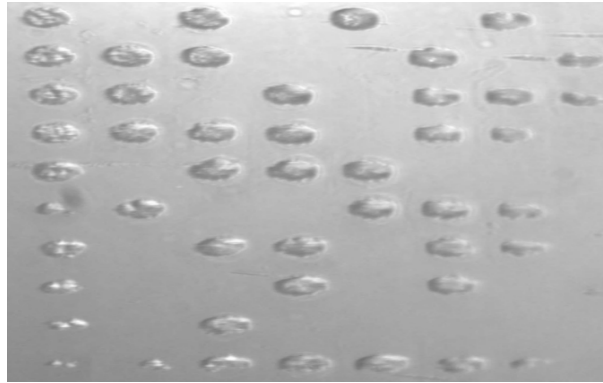


Figure 1.28: Data matrix engraved on clear glass material using ArF excimer laser with the wavelength of 193 nm, with a fluence of $F = 0.95 J/cm^2$ and 200 pulses [66].

In general, the specific geometric shape of the crater is that of a straight circular cone with very small dimensions [20]. For the best engraving in accordance with the finesse, the depths, shapes and dimensions of all the craters generated in the material by the action of the laser radiation on it should be the same.

Laser technologies are of particular interest in the field of transparent materials inscription. For such materials inscription, the lasers usually used, nanosecond pulse duration, have wavelengths most often in the ultraviolet range. However, for the ns-laser inscription, the pulse duration is larger than the time required for transfer of laser energy for absorption and conversion to heat energy which is responsible for laser machining. This heat energy diffuses from skin layer to the significant thickness of bulk material by conduction, and therefore re-solidified layer and microcracks are visible on the machined surface. Laser marking and engraving is now considered an area of interest for femtosecond technologies [77]. It is possible to reach, in femtosecond mode (1 femtosecond = 10^{-15} second), the laser ablation threshold of all types of materials: special metals and ceramics, organic or polymeric materials and transparent glass (amorphous or crystalline). The use of femtosecond pulses has opened many industrial and scientific perspectives, especially for transparent material engraving. Indeed, the field of engraving is a very active area of femtosecond applications. It is an industrial sector in strong development, for the needs of identification and traceability of industrial production and the fight against counterfeiting.

1.4 Femtosecond laser inscription on transparent material

In Petrovic *et al* [21], a model was proposed to describe the dynamics of femtosecond laser in laser inscription processes involving nonlinear transparent media with Kerr nonlinearity (as for instance fused silica materials [21]). In this model, the laser propagation in the material was accompanied by multiphoton ionization processes contributing in the generation of a free electron plasma. The model was represented by a complex Ginzburg-Landau (CGL) equation for the laser propagation in the Kerr optical medium, coupled to a rate equation describing time variation of the electron plasma. In this model, multiphoton ionization resulted in a higher (i.e. K)-order nonlinear term both in the CGL equation and the rate equation. In their work the authors [21] led their attention on thermal processes associated with laser propagation in the nonlinear transparent medium, by carrying out numerical simulations and establishing that multiphoton ionization processes would minimize drastically thermal drawbacks during macromachining processes involving femtosecond laser.

J. Krüger *et al* [2], has shown experimentally that during the transparent material inscription with a femtosecond laser in the presence of plasma generation, the craters generated in the material are inhomogeneous (i.e. Do not have the same depth, shape and size), when the laser fluence decrease from $F = 0.8\text{J}/\text{cm}^2$ to $F = 0.2\text{J}/\text{cm}^2$ (see figure 1.29).

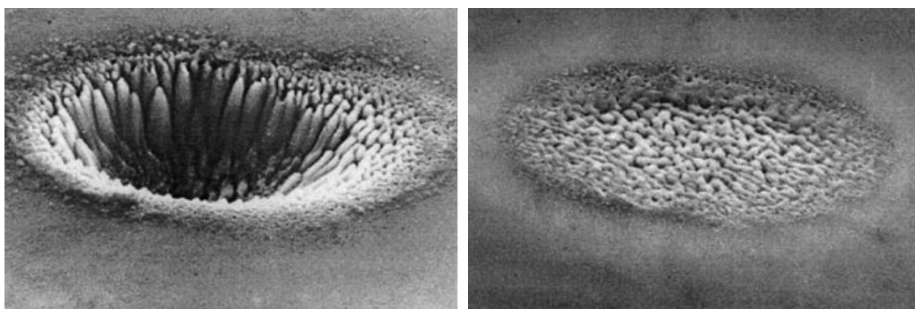


Figure 1.29: Laser ablation of transparent material with $F = 0.8\text{J}/\text{cm}^2$ (left) and $F = 0.2\text{J}/\text{cm}^2$ (right) both of them with $\lambda = 612\text{nm}$ and $T = 300$ femtosecond [2].

In this chapter, we introduced some basic concepts regarding lasers then we emphasized on femtosecond laser transparent material-interaction. We described the optical Kerr effect as

well as the main energy deposition mechanisms via the photoionization and formation of an electron-hole plasma. We also paid attention on the laser inscription process. For this last point, we presented the two methods used in the material inscription processes with lasers. In addition to this, we have presented the mark legibility characteristics as well as the important inscription parameters. To follow the objective of our dissertation, the review work on lasers marking and engraving in the inscription technology was done. In this cases, we presented the work done by some authors in the marking of transparent ceramic with Nd:YAG laser. Moreover, we have introduced another work done in the engraving of transparent glass material with CO_2 laser.

These literature review that we have done in this first chapter allowed us to identify one of the phenomenon (i.e. plasma generation in material), that affect the laser inscription process on the transparent material. In fact, femtosecond laser transparent material inscription is a nonlinear process, which induce the modification of the refractive index of this material via optical Kerr effect. This optical Kerr effect focuses the laser beam into the transparent material, producing ionization and generated an electron plasma whose density growths and affects the laser signal in the inscription process. As we mentioned in our general introduction, we are interesting on amorphous silica inscription with promise application in characters engraving. To be more specific, our objective is to optimize this inscription process. Where optimization is meant to provide an optimal combination of continuous-wave and femtosecond lasers parameters and amorphous silica properties that must be set for the best engraving finesse. To follow the goal of our work, in the next chapter, the amorphous silica properties as well as the theoretical model for lasers interacting with amorphous silica will be presented. This will be following by the methodology of our thesis.

Material, Theoretical Model and Methodology

The aim of this chapter, is to present some basic notion regarding the structures of crystalline and amorphous silica. In this purpose, the mean distances between the chemical bonds of each structure will be introducing as well as the bonds angles. Furthermore, the diagram of the phase transition paths between different categories of silica material will be presenting. Some important properties of fused silica will be also introduce. Then we shall build the model for laser used for the inscription processes on fused silica material. Finally this chapter will be ending with the methodology that we will be utilizing within the main part of our work.

Indeed, materials in the crystalline solid state is composed of a periodic arrangement (the lattice) and a pattern of atoms (their natures and relative positions). The lattice defines quantitatively the periodic nature of the crystal structure described by mesh parameters. The pattern concerns the chemical nature of the solid. The crystal is generated by applying to the basic group of atoms all the translations of the lattice. This structure is to be contrasted to the amorphous solid state for which we find neither periodicity nor order at a medium and long distance from the atom pattern. Glasses are the main representatives of this class of solids [78]. However, each atom has an electronic precession, the experimental proof of which was provided at the end of the 19th century by J. J. Thomson. We generally distinguish two families of electrons according to their energy bond. The core electrons are strongly connected to their parent atom and localized. Since this strong bond energy is of the order of a hundred electron volts, they are not accessible to the optical excitations used within this thesis. The electrons of valence are weakly linked and partially delocalized. They are responsible for many macroscopic properties in solid-state physics. In 1930, F. Bloch demonstrated the influence of electronic properties on the macroscopic behavior of matter in the crystalline solid-state using

band theory. This quantum theory is based on solving Schrödinger's equation, associated with a periodic description of the crystal. This provided a clear understanding of the existence of the band structure in the material. This demonstrates the existence of the bandgap i.e. of forbidden energy levels for the electron. The position of the electronic occupation levels with respect to this forbidden band has a strong influence on the physical, thermal, and optical properties of the material [78]. The position of the Fermi level E_F , which is the highest energy level occupied at 0 K, allows to categorize solids as, **Metals, insulators and Semiconductors**.

2.1 Crystalline and amorphous silica structures

Silica exist in a crystalline and non-crystalline form [44]. This material is the main composition of glasses. It is made of silicon and oxygen. This silicon atom is connected to 4 oxygen atoms forming silicon dioxide (SiO_2). The silicon is placed in 4 coordination and the oxygen atoms in 2 coordination as shown on figure 2.1. However, most of glasses used in research are made

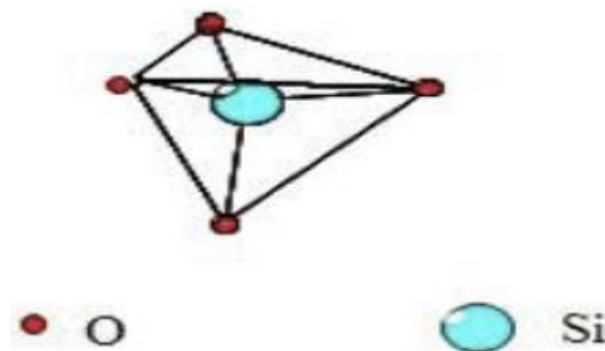


Figure 2.1: Tetrahedral pattern of silica [79].

by oxide silicon with the chemical formula (SiO_2). Glass based on this type of material is transparent in the ultraviolet, visible, and near-infrared [80]. Actually, quartz, tridymite, and cristobalite are the crystalline varieties of glass silica (SiO_2), while the non-crystalline form refer to amorphous silica [81]. Figure 2.2 represent the diagram of the phase transition from the crystalline forms to the amorphous form.

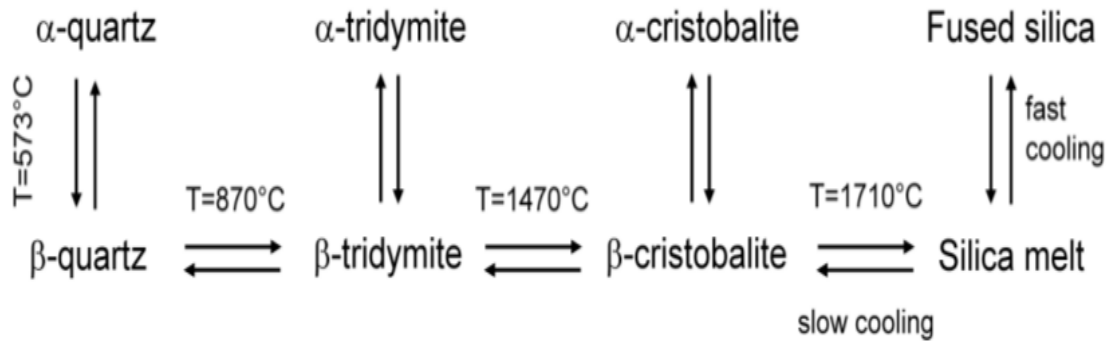


Figure 2.2: Diagram of the phase transition paths between different varieties of silica at 1 atmosphere pressure, as controlled by temperature [79].

2.1.1 Crystalline silica structure

In crystalline silica, the silicon and oxygen atoms are arranged in a fixed geometric pattern (see for instance figure 2.3) [82]. For this type of silica, the distances between $Si-O$ is 1.61\AA .

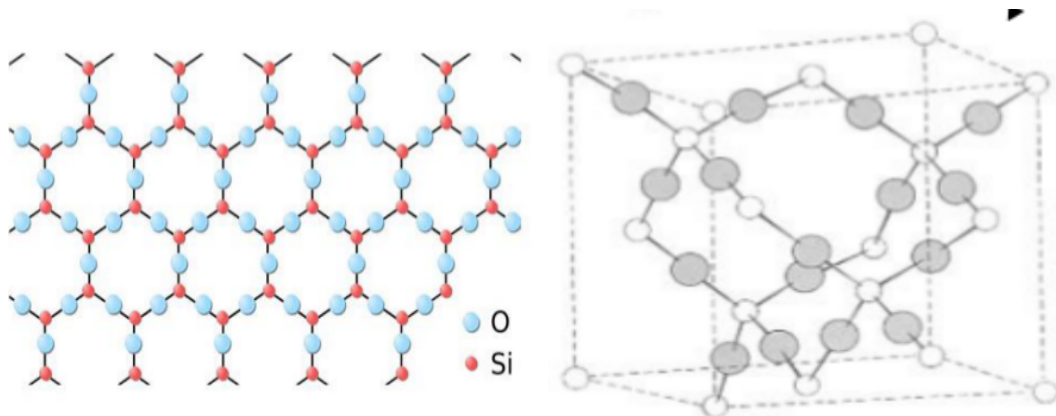


Figure 2.3: Crystalline structures of SiO_2 : 2D (left) and 3D (right) [83, 84].

The bonding between Si and O atoms is sufficiently strong that it forms very rigid structures with a $O-Si-O$ angle $\phi_T = 109.5^\circ$ [85, 86].

2.1.2 Amorphous silica structure

In amorphous silica also known as fused silica, no spatial ordering of the atoms is present (see figure 2.4). This disorder is due to the inability of the molecules to reorganize themselves to get a balanced structure. This structure is said to be disordered on a large scale. But

on an inter-atomic scale, the structure is orderly. It has a pattern that repeats itself but in different directions. The most important parameter is the mean equilibrium bond length of

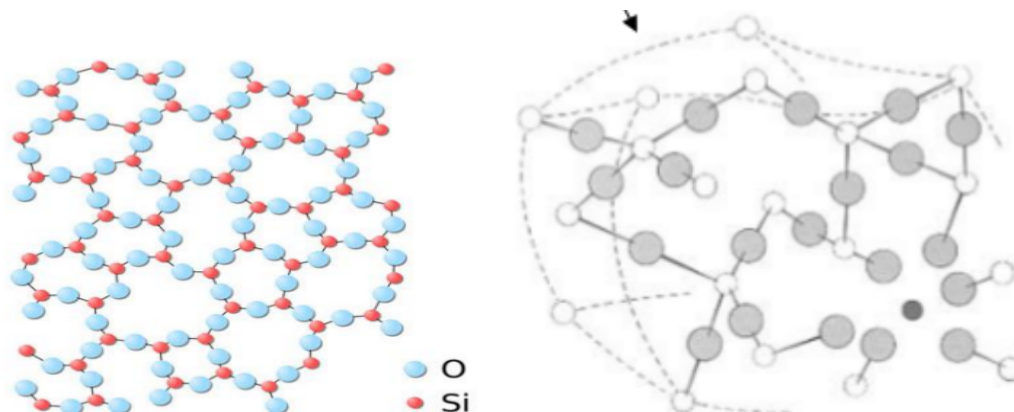


Figure 2.4: Amorphous structures of SiO_2 : 2D (left) and 3D (right) [83, 84].

$Si - O$, however, the mean distances between $O - O$ and $Si - Si$ could also be considered. These different distances between chemical bonds are $Si - O$ (1.6\AA), $O - O$ (2.6\AA) and $Si - Si$ (3.2\AA), as determined from X -rays diffraction [85]. The $Si - O - Si$ bond angles are about 144° .

According to what we have seen in the above two subsections, it is clear that the difference between crystalline silica and amorphous silica are highly visible. Actually, this difference in structure was revealed in X -ray diffraction by Zachariasen [87]. He showed that a crystalline structure had a spectrum with fine peaks corresponding to the different crystal planes whereas the spectrum of an amorphous structure was spread out. In general, the crystalline silica favours the diffraction phenomena when it interacts with an electromagnetic radiation. Therefore, among different categories of glasses that exist, fused silica glass has attracted considerable attention because of its favorable physical, chemical, and optical characteristics [88, 34]. In most of the modern industry, amorphous silica is used in numerous applications such as glassware in laboratory, lenses or beam splitters in optics, dielectric insulator in micro and optoelectronics, optical fiber in telecommunication etc..

2.2 Amorphous silica glass properties

Fused Silica has a remarkably low coefficient of thermal expansion, which varies only slightly with temperature [80]. This material characteristic imparts fused silica a high resistance to thermal shock, and makes it an excellent material for applications that require the utmost in dimensional stability over a large temperature range. Fused silica shows an almost perfect brittle elastic behavior at temperature lower than the transformation point. Some important properties of fused silica is given in table 2.1

Table 2.1: Some Important Properties of Amorphous Silica Glass

Coefficient of thermal expansion	$0.57 \times 10^{-6}/K$ over $0\text{ }^{\circ}C$ to $200\text{ }^{\circ}C$ temperature range [80]
Thermal conductivity	$1.38W/mK$, measured at $25\text{ }^{\circ}C$ [80]
Density	$2.202g/cm^3$ [80]
Elasticity modulus	$73GPa$ at $25\text{ }^{\circ}C$ [80]
Band gap	$E_g = 7.6eV$ [34]
Free electron mass	$m_e = 0.9 \times 10^{-30}kg$ [86]
Effective mass of electron	$m = 0.86m_e$ [86]
Electron trapping time	$\tau_s = 150\text{ fs}$ [35]
Group velocity dispersion coefficient	$k'' = 361\text{ fs}^2/cm$ [86]
Linear refractive index	$n_0 = 1.45$ [35]
Nonlinear refractive index	$n_2 = 3.54 \times 10^{-16}\text{ cm}^2/W$ [35]
Electron collision time	$t_0 = 1fs$ [35]
Maximum electron density	$\rho_{max} = 2.2 \times 10^{22}cm^{-3}$ [35]
Absorption coefficient	$\beta_n = 1.8 \pm 0.4 \times 10^{-5}\text{ cm}^{-1}$ [89]

Fused silica offers a set of optical characteristics that compare favorably with other optical materials. The optical properties of fused silica can be fully described in terms of transmission, absorption, reflection, dispersion and scattering. The description of these properties is based on the interaction of an electromagnetic wave with this material. To establish an optical description, two quantities are necessary i.e. the complex refractive index \tilde{n} and the dielectric function ϵ . These two quantities are related by $\tilde{n}^2 = \epsilon$. This index of refraction

depends on the wavelength of light propagating in this medium. It decreases as the wavelength increases, implying a dispersion of the optical field. In general, the dispersion is described from the wavenumber, which is a function of the frequency $k(\omega)$. From this, the group velocity is defined as $v_g = \partial\omega/\partial k$. As the first derivative of the dispersion relation affects only pulse propagation velocity, then the pulse shape is also altered by the second or higher order terms. The second derivative of the dispersion relation, which is related to the group velocity dispersion, which is the principal source of pulse spreading is $k'' = \partial^2 k/\partial\omega^2$, evaluated at $\omega = \omega_0$ where ω_0 is a center frequency. In the fused silica material, the dispersion is represented by the quantity [36]:

$$\Gamma_N = -i \frac{k''}{2} \frac{\partial^2 E}{\partial t^2}, \quad (2.1)$$

where E is the electric field of the electromagnetic wave passing through fused silica material. By setting $\theta_N = -k''/2$, equation (2.1) becomes:

$$\Gamma_N = i\theta_N \frac{\partial^2 E}{\partial t^2} \quad (2.2)$$

where θ_N is a group velocity dispersion. This quantity can be positive or negative. Actually, when θ_N is positive, it correspond to the normal dispersion regime and when θ_N is negative, it correspond to the anomalous dispersion regime.

In general, the propagation of laser beam into a material starts at its surface and the laser beam entering the material is given by the transmittance, T , which is related to the surface reflectance, R , as $T = 1 - R$. Indeed, the reflectivity R is given by the refractive index of the material and the surrounding media as well as the angle of incident. The reflectivity is polarization dependent and is expressed for s - and p - polarized light by the well-known Fresnel equations [90]:

$$R_s = \left(\frac{n_1 \cos(\theta_i) - n_2 \cos(\theta_t)}{n_1 \cos(\theta_i) + n_2 \cos(\theta_t)} \right)^2 \quad (2.3)$$

$$R_p = \left(\frac{n_1 \cos(\theta_t) - n_2 \cos(\theta_i)}{n_1 \cos(\theta_t) + n_2 \cos(\theta_i)} \right)^2 \quad (2.4)$$

P -polarized light has the electric field oscillating parallel to plane of incidence and s -polarized perpendicular, i.e. for normal incident R_p and R_s are identical.

The absorption properties of fused silica is defined by the Beer-Lambert Law that we have already introduced in chapter 1. Actually, the range of transparency of fused silica is mainly related to the composition of this material. It is delimited by two boundaries: The bandgap boundary and the multiphonon boundary. The first boundary is related to the absorption of optical field by electronic transitions, from the valence band to the conduction band. The second limit is related to the vibrations of the chemical bonds.

As a summary we could say that:

- ☞ Chemical properties: Fused silica is composed of pure SiO_2 in amorphous (non-crytalline) form. When compared to other optical glasses, fused silica has a much higher melting temperature. It is an extremely inert glass.
- ☞ Thermal properties: Fused silica has low coefficient of thermal expansion, which changes slightly with temperature. This makes it highly resistant to thermal shock, and is an excellent choice for application involving large temperature range. Thus, they are excellent thermal insulators.
- ☞ Optical properties: Fused silica possesses a set optical characteristics that makes them better than other optical material. It is transparent in the ultraviolet (UV), visible and near infrared. They respond nonlinearly to high intensity irradiations.
- ☞ Fused silica appears to be excellent electrical insulator.

Before going further, we would like to recall that our objective in this dissertation is to investigate the continuous-wave and femtosecond lasers inscriptions on amorphous silica glass. In this respect, it is important to introduce some characteristics of the above mentioned lasers in what will follow.

2.3 Characteristics of the lasers used for inscription on amorphous silica

In this application, lasers are designed to operate in specific regimes characterized by their powers and wavelength. Indeed, currently, femtosecond lasers are mostly used in the inscription processes. To this last point, since femtosecond lasers are optical fields with a duration far below picoseconds, they belong to a specific class of lasers known as ultrashort lasers. Lasers in this class operate typically in pulsed modes of relatively high powers, nevertheless in some contexts they can be tailored to operate in the continuous-wave regime. This is for instance the case when their input powers are below the typical power of a high-intensity optical pulse, or when the input field is of low power and is designed to grow upon propagation in the amorphous silica glass from continuous-wave mode to a high-intensity pulse.

2.3.1 Characteristic of continuous-wave laser

In general, for lasers operating in continuous-wave regime, the beam is uninterrupted because their output power is constant in time. Continuous-wave laser can be used to generate pulsed lasers via mode-locked system. Indeed, mode-locked is methods utilized to generate ultrashort pulse (i.e. femtosecond laser).

2.3.2 Characteristic of pulsed laser

Pulsed lasers are devices that deliver short or ultrashort pulses energy with higher peak powers. In this work, we are dealing with ultrashort pulse laser. This kind of laser is producing pulses in the order of femtosecond and its power is in the order of petawatts. Figure 2.5 shows the profile of continuous-wave and pulsed lasers in the time domains [91].

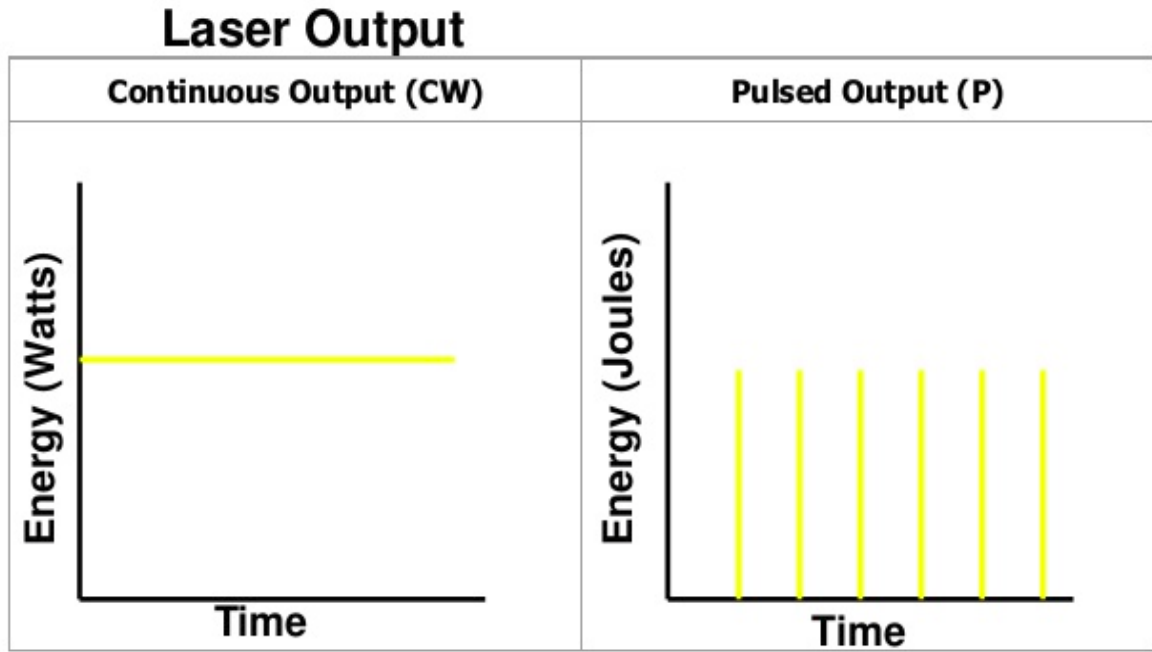


Figure 2.5: Continuous-wave laser output (left) and Pulsed laser output right [91].

The mostly type of femtosecond laser used in the laser inscription is the Ti:saphir ultrafast regenerative amplifier system with a center wavelength of 800 nm and the repetition rate of 1 kHz [35]. An experimental setup of femtosecond laser material inscription given in the literature is shown on figure 2.6.

As we are dealing with transparent amorphous silica, a single photon from the femtosecond laser beam cannot promote electron in the conduction band of this material, since the photon energy is small compared to the material band gap. Therefore the process will be required a minimum of two-photon. For the above femtosecond laser with the wavelength of 800 nm the energy for the single photon from the laser radiation can be calculated as:

$$E_L = \frac{hc}{\lambda} = \frac{6.62 \times 10^{-34} \times 3.10^8}{800.10^{-9}} = 2.48 \times 10^{-19} J, \quad (2.5)$$

$$E_L = 2.48 \times 10^{-19} J = \frac{2.48}{1.6} \times 1.6 \times 10^{-19} = 1.55eV \quad (2.6)$$

where, c is the speed of light and h is the Planck's constant. Because of the fact that a single photon from the femtosecond laser beam cannot promote electron in the conduction band of amorphous silica glass, let us compute the maximum number of photon that should

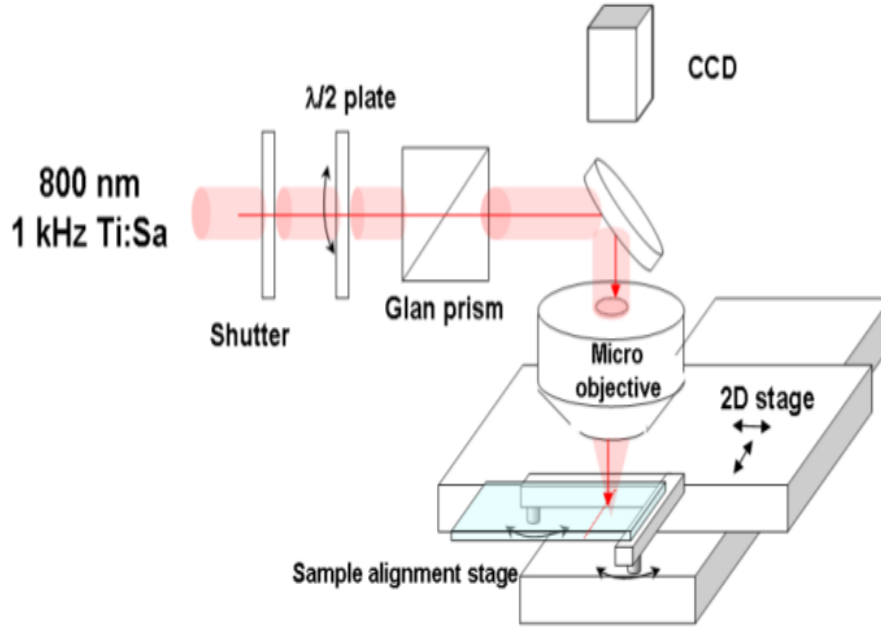


Figure 2.6: Experimental setup for implementation of plasma assisted material processing in the bulk of amorphous silica [83].

be required by this material to allow an electron to reach its conduction band as:

$$K E_L \geq E_g \implies K = \frac{E_g}{E_L}, \quad (2.7)$$

where E_L is the above value of single photon energy from the laser beam and K the maximum value of photon required by amorphous silica glass. The band gap of amorphous silica is $E_g = 7.6\text{eV}$ and it follows from this that:

$$K = \frac{7.6}{1.55} = 4.90 \approx 5. \quad (2.8)$$

2.4 Theoretical model for laser inscription on amorphous silica glass

We are already said in chapter 1 that Petrovic *et al.* [21] proposed the theoretical model for femtosecond laser inscription. This existing proposed model is a coupled equations, namely the first one, which describe the dynamics of the laser field and the second one for the time evolution of the plasma generated during the propagation of the optical field in amorphous

silica material. The model proposing by these authors are given by equations (2.9) and (2.10).

$$i\frac{\partial u}{\partial z} + \Delta_{\perp}u - \delta\frac{\partial^2 u}{\partial t^2} + \sigma|u|^2u = -i\gamma_0(1 - i\omega_0\tau_0)\rho u - i\mu|u|^{2K-2}u \quad (2.9)$$

$$\frac{\partial \rho}{\partial t} = \nu|u|^2\rho + |u|^{2K} \quad (2.10)$$

However, the model we are interest in is an extension of a version discussed in [21], where the extension is meant to take into account the contributions of electron-hole radiative recombination processes. This translates into an additional term in the Drude equation quadratic in the electron plasma density, competing with the avalanche impact ionization and the multiphoton ionization. In addition to this we also considered the plasma balance rate due to multi-photon absorptions in the plasma equation. These two consideration makes our model to be different from the one proposed by Petrovic *et al.* In general, the laser equation is modelled starting from Maxwell's equations while the plasma equation is derived according to Keldysh theory. This two key points of the modelling will be helped us to build our model. In this goal, some approximations will be considered and all those approximations will be discussed at every derivation step with the explanation of their physical meaning such that the final laser model will be well established.

2.4.1 Laser equation

As we mentioned above, we start our consideration from the Maxwell equations [92]:

$$\vec{\nabla} \times \vec{E}(\vec{r},t) = -\frac{\partial \vec{B}(\vec{r},t)}{\partial t} \quad (2.11)$$

$$\vec{\nabla} \times \vec{H}(\vec{r},t) = \vec{J}(\vec{r},t) + \frac{\partial \vec{D}(\vec{r},t)}{\partial t} \quad (2.12)$$

$$\vec{\nabla} \cdot \vec{E}(\vec{r},t) = \frac{\rho - \vec{\nabla} \cdot \vec{P}(\vec{r},t)}{\epsilon_0} \quad (2.13)$$

$$\vec{\nabla} \cdot \vec{B}(\vec{r},t) = 0 \quad (2.14)$$

$$\vec{D}(\vec{r},t) = \epsilon_0 \vec{E}(\vec{r},t) + \vec{P}(\vec{r},t), \quad (2.15)$$

where, $\vec{E}(\vec{r},t)$ and $\vec{H}(\vec{r},t)$ are respectively, the electric and magnetic fields, $\vec{P}(\vec{r},t)$ is the polarization, $\vec{B}(\vec{r},t)$ is an induced magnetization $\vec{B}(\vec{r},t) \simeq \mu_0 \vec{H}(\vec{r},t)$, $\vec{D}(\vec{r},t)$ is the electric displacement, ρ and $\vec{J}(\vec{r},t)$ are carrier and current densities respectively. ϵ_0 , μ_0 denote the permittivity and permeability of free space. $\vec{\nabla}$ represent usually a vector of first order spatial derivatives [34].

Replacing $\vec{B}(\vec{r},t) \simeq \mu_0 \vec{H}(\vec{r},t)$ into equation (2.12) and taking its derivative reads:

$$\vec{\nabla} \times \frac{\partial \vec{B}(\vec{r},t)}{\partial t} = \mu_0 \left(\frac{\partial \vec{J}(\vec{r},t)}{\partial t} + \frac{\partial^2 \vec{D}(\vec{r},t)}{\partial t^2} \right) \quad (2.16)$$

Taking equations (2.11) and (2.15) into equation (2.16) yields:

$$-\vec{\nabla} \times (\vec{\nabla} \times \vec{E}(\vec{r},t)) = \mu_0 \left(\frac{\partial \vec{J}(\vec{r},t)}{\partial t} + \epsilon_0 \frac{\partial^2 \vec{E}(\vec{r},t)}{\partial t^2} + \frac{\partial^2 \vec{P}(\vec{r},t)}{\partial t^2} \right) \quad (2.17)$$

By introducing the relationship $\vec{\nabla} \times (\vec{\nabla} \times \vec{E}(\vec{r},t)) = \vec{\nabla}(\vec{\nabla} \cdot \vec{E}(\vec{r},t)) - \Delta \vec{E}(\vec{r},t)$ into equation (2.17), we obtain:

$$\Delta \vec{E}(\vec{r},t) - \vec{\nabla}(\vec{\nabla} \cdot \vec{E}(\vec{r},t)) = \mu_0 \left(\frac{\partial \vec{J}(\vec{r},t)}{\partial t} + \epsilon_0 \frac{\partial^2 \vec{E}(\vec{r},t)}{\partial t^2} + \frac{\partial^2 \vec{P}(\vec{r},t)}{\partial t^2} \right). \quad (2.18)$$

In general, the current density $\vec{J}(\vec{r},t)$ responsible to the motion of free electrons is created by the ionization of atom in the medium whereas, the dynamics of the ions is discarded. According to the polarization $\vec{P}(\vec{r},t)$, it is responsible for the bound electron response driven by the femtosecond laser pulse. It is usually decomposed into a linear part $\vec{P}_L(\vec{r},t) \equiv P^{(1)}(\vec{r},t)$ and nonlinear part $\vec{P}_{NL}(\vec{r},t)$ satisfying $|P^{(1)}(\vec{r},t)| \gg |P_{NL}(\vec{r},t)|$ [93]. The linear part is related to the first-order susceptibility tensor $\chi^{(1)}$ and corresponds physically to the range of electric fields where most electrons are still bound to the nucleus. It follows from this that equation (2.18) can be written as:

$$\Delta \vec{E}(\vec{r},t) - \vec{\nabla}(\vec{\nabla} \cdot \vec{E}(\vec{r},t)) = \mu_0 \left(\frac{\partial \vec{J}(\vec{r},t)}{\partial t} + \epsilon_0 \frac{\partial^2 \vec{E}(\vec{r},t)}{\partial t^2} + \frac{\partial^2 \vec{P}(\vec{r},t)_L}{\partial t^2} + \frac{\partial^2 \vec{P}(\vec{r},t)_{NL}}{\partial t^2} \right) \quad (2.19)$$

To follow the ultimate goal of our work, we proceed by introducing some approximations that would help us to reduce the vectorial wave equation (2.19) to the scalar wave equation. Indeed, the electric field is assumed to remain linearly polarized along a direction \vec{e}_x transverse to the propagation axis. To be more explicit, the electric field and the medium response $(\vec{J}(\vec{r},t), \vec{P}(\vec{r},t))$ are transverse, which mean perpendicular to the propagation direction and determined by the wave vector \vec{k} . This standard assumption in propagation of electromagnetic fields means that the quantity $\vec{\nabla}(\vec{\nabla} \cdot \vec{E}(\vec{r},t))$ in equation (2.19) can be neglected. This remains valid as long as radiation are not too strongly focused. It follows then from this last assumption that, by projection along the polarization direction \vec{e}_x i.e. $\vec{E}(\vec{r},t) = E(\vec{r},t)\vec{e}_x$, $\vec{J}(\vec{r},t) = J(\vec{r},t)\vec{e}_x$, $\vec{P}(\vec{r},t) = P(\vec{r},t)\vec{e}_x$, equation (2.19) becomes [92]:

$$\Delta E(\vec{r},t) - \mu_0 \left(\epsilon_0 \frac{\partial^2 E(\vec{r},t)}{\partial t^2} + \frac{\partial^2 P_L(\vec{r},t)}{\partial t^2} \right) = \mu_0 \left(\frac{\partial J(\vec{r},t)}{\partial t} + \frac{\partial^2 P_{NL}(\vec{r},t)}{\partial t^2} \right) \quad (2.20)$$

Equation (2.20) is easier to handle in the Fourier domain since the computation of the polarization term present in this later equation is a little bit complicated in the temporal domain. Indeed for isotropic, homogeneous and non magnetizable media and spectral ranges far from any material resonance, the linear polarization term can be expressed in the frequency domain as:

$$\hat{P}_L(\vec{r},\omega) = \epsilon_0\chi^{(1)}(\omega)\hat{E}(\vec{r},\omega) \quad (2.21)$$

Where the scalar dielectric function $\epsilon(\omega)$ is defined by $\epsilon(\omega) = 1 + \chi^{(1)}(\omega)$.

Duel to the fact that $\chi^{(1)}(\omega)$ is complex-valued, the dielectric function $\epsilon(\omega)$ contains the information about material dispersion and the linear losses specified by the imaginary part of $\chi^{(1)}(\omega)$. In general when these losses are negligible, $\epsilon(\omega)$ is approximately real and can be represented as $\epsilon(\omega) = \epsilon_0\epsilon_r(\omega)$ meaning that the linear refractive index of the medium, enters the wave number of the laser field define as $k(\omega) = \sqrt{\epsilon(\omega)}\omega/c$. By convention, $n_0 \equiv n(\omega_0)$ for the central frequency $\omega_0 = 2\pi c/\lambda_0$ of a laser operating at a wavelength λ_0 and $k_0 \equiv k(\omega_0)$. In what follows it will be convenient to evaluate each side of equation (2.20). In this case let us call the left and the right hand sides A and B respectively, namely:

$$A = \Delta E(\vec{r},t) - \mu_0 \left(\epsilon_0 \frac{\partial^2 E(\vec{r},t)}{\partial t^2} + \frac{\partial^2 P_L(\vec{r},t)}{\partial t^2} \right) \quad (2.22)$$

$$B = \mu_0 \left(\frac{\partial J(\vec{r},t)}{\partial t} + \frac{\partial^2 P_{NL}(\vec{r},t)}{\partial t^2} \right) \quad (2.23)$$

a) Evaluation of the left hand side A

The Fourier transformation of equation (2.22) is:

$$\hat{A} = \Delta \hat{E}(\vec{r},\omega) + \frac{\omega^2}{c^2} \hat{E}(\vec{r},\omega) - \mathcal{F} \left[\mu_0 \frac{\partial^2 \vec{P}_L(\vec{r},t)}{\partial t^2} \right] \quad (2.24)$$

From the electric displacement we have:

$$\epsilon_0 \vec{E}(\vec{r},t) + \vec{P}(\vec{r},t) = \epsilon(\omega) \vec{E}(\vec{r},t) \quad (2.25)$$

When we multiply equation (2.25) by μ_0 and take its second derivation, it becomes:

$$\mu_0 \frac{\partial^2 \vec{P}_L(\vec{r},t)}{\partial t^2} + \frac{1}{c^2} \frac{\partial^2 \vec{E}(\vec{r},t)}{\partial t^2} = \frac{\epsilon_r(\omega)}{c^2} \frac{\partial^2 \vec{E}(\vec{r},t)}{\partial t^2} \quad (2.26)$$

Where $\mu_0\epsilon_0c^2 = 1$ and $\epsilon(\omega) = \epsilon_0\epsilon_r(\omega)$, with $\epsilon_r(\omega) = n^2(\omega)$ the refractive index. The Fourier transformation of equation (2.26) is given in this case by:

$$\mathcal{F} \left[\mu_0 \frac{\partial^2 \vec{P}_L(\vec{r}, t)}{\partial t^2} \right] - \frac{\omega^2}{c^2} \hat{E}(\vec{r}, \omega) = -\frac{n^2(\omega)\omega^2}{c^2} \hat{E}(\vec{r}, \omega) \quad (2.27)$$

$$-\mathcal{F} \left[\mu_0 \frac{\partial^2 \vec{P}_L(\vec{r}, t)}{\partial t^2} \right] = k^2(\omega) \hat{E}(\vec{r}, \omega) - \frac{\omega^2}{c^2} \hat{E}(\vec{r}, \omega) \quad (2.28)$$

Where $k(\omega) = n(\omega)\omega/c$ is the wavenumber. Replacing equation (2.28) into equation (2.24) yield:

$$\hat{A} = \Delta \hat{E}(\vec{r}, \omega) + k^2(\omega) \hat{E}(\vec{r}, \omega) \quad (2.29)$$

Let us consider first one Cartesian component of the electric field in a given point by $E(t)$. Thus we define the electric field as a superposition of monochromatic wave thus:

$$E(t) = \int_{-\infty}^{\infty} \hat{E}(\omega) e^{-i\omega t} d\omega \quad (2.30)$$

The equation describing the propagation of femtosecond laser that we are modelling in our thesis, is a source of ultra short pulse and this allows us to consider at this setp that the wave from the laser source is quasi-monochromatic with its spectrum placing around the central frequency of the laser. Indeed the wave will be considered as quasi-monochromatic if $(\delta\omega/\omega_0) \ll 1$, where $\delta\omega$ is a laser spectrum while ω_0 is a central frequency of the laser [34]. Physically, this means that, the optical field consists of one or small number of waves, where we can assume that the spread of the laser in frequency $\delta\omega$ of each of the waves is small compared to the carrier frequency ω_0 . This assumption $(\delta\omega/\omega_0) \ll 1$ is also called the slowly varying envelope approximation. Assuming at this step of our work that this approximation of quasi-monochromatic wave is valid, it is possible for us to write:

$$\omega = \omega_0 + \delta\omega \quad \text{with} \quad \frac{\delta\omega}{\omega_0} \ll 1 \quad (2.31)$$

By taking equation (2.31) into equation (2.30) we obtain:

$$E(t) = e^{-i\omega_0 t} \left(\int_{-\infty}^{\infty} \hat{E}(\omega) e^{-i\delta\omega t} d(\delta\omega) \right) = e^{-i\omega_0 t} U_s(t), \quad (2.32)$$

where $U_s(t)$ is the electric field components which is slowly varied in time. As we are dealing with a quasi-monochromatic wave, equation (2.29) can be written as:

$$\hat{A} = \Delta \hat{E}(\omega) + k^2(\omega_0 + \delta\omega) \hat{E}(\omega) \quad (2.33)$$

The wavenumber $k(\omega_0 + \delta\omega)$ usually described the chromatic dispersion of the laser as it propagates in a nonlinear medium. Indeed the group velocity v_g of the pulse laser can be calculated from $v_g = \partial\omega/\partial k$ evaluated at the center frequency ω_0 . Generally, the first derivative of the dispersion relation only affects the pulse propagation velocity and the pulse shape is altered by second or high order derivative. The second derivative of the dispersion relation is related to the group velocity dispersion and it is the principal source of pulse spreading [36, 94]. To take into account this phenomenon, we would use the Taylor expansion of the wavenumber $k(\omega_0 + \delta\omega)$ around the central frequency ω_0 in the second order:

$$\begin{aligned} k^2(\omega_0 + \delta\omega) &= k^2(\omega_0) + \left[\frac{d}{d\omega} (k^2(\omega)) \right]_{\omega=\omega_0} \delta\omega + \frac{1}{2!} \left[\frac{d^2}{d\omega^2} (k^2(\omega)) \right]_{\omega=\omega_0} (\delta\omega)^2 \\ &= k^2(\omega_0) + 2k_0 \left[\frac{dk}{d\omega} \right]_{\omega=\omega_0} \delta\omega + \left[\frac{dk}{d\omega} \right]_{\omega=\omega_0}^2 (\delta\omega)^2 + k_0 \left[\frac{d^2k}{d\omega^2} \right]_{\omega=\omega_0} (\delta\omega)^2 \\ &= k_0^2 + 2\frac{k_0}{v_g}(\delta\omega) + \left(\frac{1}{v_g^2} + k_0 k_0'' \right) (\delta\omega)^2, \end{aligned} \quad (2.34)$$

where $k_0 = k(\omega_0) = n_0\omega_0/c$ with $n_0 = n(\omega_0)$. $v_g = \left[\frac{d\omega}{dk} \right]_{\omega=\omega_0}$ represent the group velocity of the optical wave at the carried wave frequency ω_0 while k_0'' represent the variation of the group velocity. Replacing equation (2.34) into equation (2.33) and rewrite it in the Fourier space yields:

$$\begin{aligned} \hat{A} = \Delta \hat{E}(\omega) + k^2(\omega) \hat{E}(\omega) &= e^{-i\omega_0 t} \left[\Delta \int_{-\infty}^{\infty} \hat{E}(\omega) e^{-i\delta\omega t} d(\delta\omega) + k^2 \int_{-\infty}^{\infty} \hat{E}(\omega) e^{-i\delta\omega t} d(\delta\omega) \right] \\ &+ e^{-i\omega_0 t} \left[2\frac{k_0}{v_g} \int_{-\infty}^{\infty} \hat{E}(\omega) e^{-i\delta\omega t} (\delta\omega) d(\delta\omega) \right] \\ &+ e^{-i\omega_0 t} \left[\left(\frac{1}{v_g^2} + k_0 k_0'' \right) \int_{-\infty}^{\infty} \hat{E}(\omega) e^{-i\delta\omega t} (\delta\omega)^2 d(\delta\omega) \right] \end{aligned} \quad (2.35)$$

This latest equation is written in the time spaces as:

$$\begin{aligned} A &= \Delta E(\vec{r}, t) - \mu_0 \left(\epsilon_0 \frac{\partial^2 E(\vec{r}, t)}{\partial t^2} + \frac{\partial^2 P_L(\vec{r}, t)}{\partial t^2} \right) \\ &= e^{-i\omega_0 t} \left[\Delta U_s(t) + k_0^2 U_s(t) + 2i\frac{k_0}{v_g} \frac{\partial U_s(t)}{\partial t} - \left(\frac{1}{v_g^2} + k_0 k_0'' \right) \frac{\partial^2 U_s(t)}{\partial t^2} \right] \end{aligned} \quad (2.36)$$

As we already assumed above that an approximation of quasi-monochromatic wave is valid for the model that we are try to construct here, then we proceed to the factorization of the part of the electric field which is varied very fast in the z direction by writing:

$$U_s(x,y,z,t) = U(x,y,z,t)e^{ik_0z} \quad (2.37)$$

From equation (2.37), we can see appearing the quantity $U(x,y,z,t)$, which is the envelope of the electric field that is vary varying slowly in the space as well as in the time.

$$\frac{\partial U_s}{\partial t} = \frac{\partial U}{\partial t}e^{ik_0z}, \quad \frac{\partial^2 U_s}{\partial t^2} = \frac{\partial^2 U}{\partial t^2}e^{ik_0z}, \quad (2.38)$$

$$\Delta U_s = \left[\frac{\partial^2 U}{\partial z^2} + 2ik_0 \frac{\partial U}{\partial z} - k_0^2 U \right] e^{ik_0z} + \Delta_{\perp} U e^{ik_0z}, \quad (2.39)$$

where, $\Delta_{\perp} = \frac{\partial^2}{\partial x^2} + \frac{\partial^2}{\partial y^2}$. Replacing equations (2.38) and (2.39) into equation (2.36) reads:

$$A = e^{-i(\omega_0 t - k_0 z)} \left[\Delta_{\perp} U + \frac{\partial^2 U}{\partial z^2} + 2ik_0 \left(\frac{\partial U}{\partial z} + \frac{1}{v_g} \frac{\partial U}{\partial t} \right) - \left(\frac{1}{v_g^2} + k_0 k_0'' \right) \frac{\partial^2 U}{\partial t^2} \right]. \quad (2.40)$$

In order to follow the pulse in its motion with the group velocity v_g , we introduce the new time variable t' that would allow the pulse to change from the laboratory reference frame to the pulse local frame.

$$\begin{cases} t' = t - \frac{z}{v_g} \\ z = z' \end{cases} \implies \begin{cases} \frac{\partial}{\partial t} = \frac{\partial}{\partial t'} \\ \frac{\partial}{\partial z} = \frac{\partial}{\partial z'} - \frac{1}{v_g} \frac{\partial}{\partial t'} \\ \frac{\partial^2}{\partial z^2} = \frac{\partial^2}{\partial z'^2} - \frac{2}{v_g} \frac{\partial^2}{\partial z' \partial t'} + \frac{1}{v_g^2} \frac{\partial^2}{\partial t'^2} \end{cases} \quad (2.41)$$

where t' denotes the retard time in the pulse frame. According to v_g , we would like to underline that it represents a constant velocity corresponding to the change of reference frame. It is possible to chose v_g arbitrarily but a convenient choice is $v_g = 1/k_0'$, which coincides with the pulse group velocity obtained from the derivation of the dispersion relation in the medium $k(\omega)$ at the central frequency of the pulse ω_0 [94]. As a next step, we replaced equation (2.41) into equation (2.40) and we obtain:

$$\begin{aligned} A &= e^{-i(\omega_0 t - k_0 z)} \left[\Delta_{\perp} U + \frac{\partial^2 U}{\partial z'^2} - \frac{2}{v_g} \frac{\partial^2 U}{\partial z' \partial t'} + 2ik_0 \frac{\partial U}{\partial z'} - k_0 k_0'' \frac{\partial^2 U}{\partial t'^2} \right] \\ &= e^{-i(\omega_0 t - k_0 z)} \left[\Delta_{\perp} U + \frac{\partial^2 U}{\partial z'^2} + 2ik_0 \frac{\partial}{\partial z'} \left(1 + \frac{i}{k_0 v_g} \frac{\partial}{\partial t'} \right) U - k_0 k_0'' \frac{\partial^2 U}{\partial t'^2} \right] \end{aligned} \quad (2.42)$$

The validity of the model that we are building requires that the second-order derivative with respect to z' of the envelope function U should be small as compared with $2k_0 (\partial U/\partial z')$ meaning that $(\partial^2 U/\partial z'^2) \ll 2k_0 (\partial U/\partial z')$ [94, 34]. This inequality, is usually referred to as the paraxiality assumption. Physically, this approximation means that the laser field amplitude and phase are evolving sufficiently slowly along the propagation direction z' . It follows then from this approximation that equation (2.42) becomes:

$$A = e^{-i(\omega_0 t - k_0 z)} \left[\Delta_{\perp} U + 2ik_0 \frac{\partial}{\partial z} \left(1 + \frac{i}{k_0 v_g} \frac{\partial}{\partial t} \right) U - k_0 k_0'' \frac{\partial^2 U}{\partial t^2} \right] \quad (2.43)$$

b) Study of the right hand side B

Let us evaluate now the right hand side of equation (2.20) as we call:

$$B = \mu_0 \left(\frac{\partial J(\vec{r}, t)}{\partial t} + \frac{\partial^2 P_{NL}(\vec{r}, t)}{\partial t^2} \right). \quad (2.44)$$

Indeed, to explicit the expression of the current density J appearing in equation (2.44), we used the Sprangle *et al* [95, 96] method, which is base on the continuity and fluid velocity equations given by:

$$\frac{\partial \rho}{\partial t} + \vec{\nabla} \cdot (\rho \vec{v}_e) = G \quad (2.45)$$

$$m_e \rho \frac{\partial \vec{v}_e}{\partial t} = \rho e \vec{E} - m_e G \vec{v}_e - m_e \rho \omega_c \vec{v}_e, \quad (2.46)$$

where, G is the electron source term proportional to the ionization rate, $\omega_c = 1/\tau_0$ is the frequency of electron collision with the neutral atoms, m_e is the electron mass while ρ and \vec{v}_e are the electron density and velocity respectively. To follows the objective of our modelling, we first multiply equation (2.45) by e and obtain:

$$e \frac{\partial \rho}{\partial t} + \vec{\nabla} \cdot (\rho e \vec{v}_e) = eG. \quad (2.47)$$

Taking the current density in the form $\vec{J} = \rho e \vec{v}_e$ and introducing it into equation (2.47) reads:

$$e \frac{\partial \rho}{\partial t} + \vec{\nabla} \cdot \vec{J} = eG \quad (2.48)$$

Maxwell equation yields $\vec{\nabla} \cdot \vec{J} = 0$ and it follows from this that:

$$\frac{\partial \rho}{\partial t} = G \quad (2.49)$$

Substituting equation (2.49) into equation (2.46) yields:

$$\begin{aligned} e\rho\frac{\partial\vec{v}_e}{\partial t} &= \frac{\rho e^2\vec{E}}{m_e} - e\vec{v}_e\frac{\partial\rho}{\partial t} - \omega_c\rho e\vec{v}_e \\ \implies e\rho\frac{\partial\vec{v}_e}{\partial t} + e\vec{v}_e\frac{\partial\rho}{\partial t} &= \frac{\rho e^2\vec{E}}{m_e} - \omega_c\rho e\vec{v}_e \end{aligned} \quad (2.50)$$

Using the relation $\vec{J} = \rho e\vec{v}_e$ that we introduced above, we derived:

$$\frac{\partial\vec{J}}{\partial t} = \frac{\partial}{\partial t}(\rho e\vec{v}_e) = e\rho\frac{\partial\vec{v}_e}{\partial t} + e\vec{v}_e\frac{\partial\rho}{\partial t} \quad (2.51)$$

From equation (2.51), the relationship given by equation (2.50) can be simplifying as:

$$\frac{\partial\vec{J}}{\partial t} = \frac{\rho e^2\vec{E}}{m_e} - \omega_c\vec{J} \quad (2.52)$$

As we defined above, $\vec{J} = J\vec{e}_x$ and $\vec{E} = E\vec{e}_x$ therefore equation (2.52) becomes:

$$\frac{\partial J}{\partial t} = \frac{\rho e^2 E}{m_e} - \omega_c J \quad (2.53)$$

To solve equation (2.53), we chose the form of the solution to be $J = j(t)e^{-\omega_c t}$ and it follows from this latest quantity that:

$$\frac{\partial J}{\partial t} = \frac{\partial j(t)}{\partial t}e^{-\omega_c t} - \omega_c j(t)e^{-\omega_c t} \quad (2.54)$$

Replacing equation (2.54) into equation (2.53) reads:

$$\frac{\partial j}{\partial t} = \frac{e^2}{m_e}\rho(t)E(t)e^{\omega_c t} \implies j(t) = \frac{e^2}{m_e} \int_{-\infty}^t \rho(t')E(t')e^{\omega_c t'} dt' \quad (2.55)$$

$$J(t) = j(t)e^{-\omega_c t} = \frac{e^2}{m_e}e^{-\omega_c t} \int_{-\infty}^t \rho(t')E(t')e^{\omega_c t'} dt' \quad (2.56)$$

To write the expression of the current density J , we consider the fact that the electrical field of the laser is propagates at the carried frequency ω_0 meaning that, $E(t) = U_s(t)e^{-i\omega_0 t}$ thus:

$$J(t) = \frac{e^2}{m_e}e^{-\omega_c t} \int_{-\infty}^t \rho(t')U_s(t')e^{-i\omega_0 t'} e^{\omega_c t'} dt' \quad (2.57)$$

Taking equation (2.57) into equation (2.53) yields:

$$\frac{\partial J}{\partial t} = \frac{e^2}{m_e}\rho(t)U_s(t)e^{-i\omega_0 t} - \frac{e^2}{m_e}\omega_c \int_{-\infty}^t \rho(t')U_s(t')e^{-i\omega_0 t'} e^{-\omega_c(t-t')} dt' \quad (2.58)$$

To compute the integral given by formula (2.58), we change the variable by considering that $y = t - t'$. Therefore equation (2.58) becomes:

$$\frac{\partial J}{\partial t} = \frac{e^2}{m_e} \rho(t) U_s(t) e^{-i\omega_0 t} \left[1 - \omega_c \int_0^{+\infty} e^{(i\omega_0 - \omega_c)y} dy \right], \quad (2.59)$$

we consider that $\rho(t)$ and $U_s = U e^{ik_0 z}$ are varied very slowly with $e^{(i\omega_0 - \omega_c)t}$ and that the electron are moving in the opposite direction of the current. Thus we obtain finally the evolution of J :

$$\begin{aligned} \frac{\partial J}{\partial t} &= -\frac{i\omega_0 e^2 \omega_c}{m_e (\omega_c^2 + \omega_0^2)} \left(1 - \frac{i\omega_0}{\omega_c} \right) \rho U e^{-i(\omega_0 t - k_0 z)} \\ &= -\frac{i\omega_0 e^2 \omega_c}{m_e (\omega_c^2 + \omega_0^2)} (1 - i\omega_0 \tau_0) \rho U e^{-i(\omega_0 t - k_0 z)} \end{aligned} \quad (2.60)$$

Let us now write the expression of the nonlinear polarization.

$$\begin{aligned} P_{NL} &= \frac{3}{4} \epsilon_0 \chi^{(3)} |E(t)|^2 E(t), \quad \text{with } E(t) = U(x, y, z, t) e^{-i(\omega_0 t - k_0 z)} \\ &= \frac{3}{4} \epsilon_0 \chi^{(3)} |U|^2 U e^{-i(\omega_0 t - k_0 z)} \end{aligned} \quad (2.61)$$

By taking the second derivation of formula (2.61) with respect to time, we obtain:

$$\frac{\partial^2 P_{NL}}{\partial t^2} = -\frac{3}{4} \omega_0^2 \epsilon_0 \chi^{(3)} |U|^2 U e^{-i(\omega_0 t - k_0 z)} \quad (2.62)$$

Combining equation (2.60) with equation (2.62), we obtain the right hand side of equation (2.20):

$$B = -\mu_0 \left[\frac{i\omega_0 e^2 \omega_c}{m_e (\omega_c^2 + \omega_0^2)} (1 - i\omega_0 \tau_0) \rho U + \frac{3}{4} \omega_0^2 \epsilon_0 \chi^{(3)} |U|^2 U \right] e^{-i(\omega_0 t - k_0 z)} \quad (2.63)$$

After eliminating the part of the electric field that is moving very fast, we obtain from the expressions of A and B that the evolution of the envelope of the electric field of the laser is given by:

$$\Delta_{\perp} U + 2ik_0 \frac{\partial}{\partial z} \left(1 + \frac{i}{k_0 v_g} \frac{\partial}{\partial t} \right) U - k_0 k_0'' \frac{\partial^2 U}{\partial t^2} = -\frac{i\mu_0 \omega_0 e^2}{m_e \omega_c (1 + \omega_0^2 \tau_0^2)} (1 - i\omega_0 \tau_0) \rho U - \frac{3}{4} \omega_0^2 \mu_0 \epsilon_0 \chi^{(3)} |U|^2 U$$

that also,

$$T \frac{\partial U}{\partial z} = \frac{i}{2k_0} \Delta_{\perp} U - \frac{ik_0''}{2} \frac{\partial^2 U}{\partial t^2} - \frac{\sigma_e}{2} (1 - i\omega_0 \tau_0) \rho U + \frac{3i}{8k_0} \omega_0^2 \mu_0 \epsilon_0 \chi^{(3)} |U|^2 U \quad (2.64)$$

Where, $T = \left(1 + \frac{i}{k_0 v_g} \frac{\partial}{\partial t} \right)$ is an operator and $\sigma_e = \frac{\mu_0 \omega_0 e^2}{k_0 m_e \omega_c (1 + \omega_0^2 \tau_0^2)}$ is the cross section for electron-neutral inverse bremsstrahlung. Actually, σ_e leads to avalanche ionization. We have seen above that $k_0 = (n_0 \omega_0)/c$ which imply that $\omega_0^2 = (c^2 k_0^2)/n_0^2$. Substituting this last relation into equation (2.64) and take $n_2 = \frac{3\chi^{(3)}}{8n_0^2}$ yields:

$$T \frac{\partial U}{\partial z} = \frac{i}{2k_0} \Delta_{\perp} U - \frac{ik_0''}{2} \frac{\partial^2 U}{\partial t^2} - \frac{\sigma_e}{2} (1 - i\omega_0 \tau_0) \rho U + ik_0 n_2 |U|^2 U \quad (2.65)$$

Introduction of multi-photon ionization processes in the laser equation

Equation (2.65) above which, describes the propagation of femtosecond laser in transparent material is not complete. Indeed the effects of multi-photon ionization (**MPI**) of the laser which leads to the generation of free electron in the material has to be introduced in the propagation equation meaning that:

$$T \frac{\partial U}{\partial z} = \frac{i}{2k_0} \Delta_{\perp} U - \frac{ik_0''}{2} \frac{\partial^2 U}{\partial t^2} - \frac{\sigma_e}{2} (1 - i\omega_0 \tau_0) \rho U + ik_0 n_2 |U|^2 U - \frac{\beta_{MPA}(|U|)}{2} U \quad (2.66)$$

It has been reported from the literature that, the quantity $\beta_{MPI}(|U|)$ can be expressed in different forms depending of the type of ionization. The quantity $\beta_{MPI}(|U|)$ would have the form of K -photons absorption if we are dealing with the multi-photon ionization and would have the tunnelling absorption form or a generalized form based on the Keldysh consideration that we have introduced in chapter 1. Actually, the function $\beta_{MPI}(|U|)$ takes the losses caused by photo-ionization into account which means that it represents physically the dissipative function in the model. In this thesis, we are dealing with the multiphoton ionization (**MPI**) and therefore the dissipative function takes the form $\beta_{MPI}(|U|) \rightarrow \beta^{(K)} |U|^{2K-2}$ where $\beta^K = K \bar{h} \omega_0 \sigma_e \rho_{nt}$ is the coefficient of multiphoton absorption (**MPA**) [97]. The order of the (**MPA**) is obtained from $K = \text{mod}(E_g / \bar{h} \omega_0) + 1$, which is the minimum number of photons of energy $\bar{h} \omega_0$ needed to overcome the energy gap E_g for liberating an electron.

c) Final laser equation

The quantity $ik_0 n_2 |U|^2 U$ which denotes the Kerr nonlinear effect in equation (2.66) has to be completed by multiplying it with T^2 and this to make our model to be valid with the one in the literature. Taking this into account in the mentioned above equation and after multiplying with the inverse operator T^{-1} the ultimate propagation equation reads:

$$\frac{\partial U}{\partial z} = \frac{i}{2k_0} T^{-1} \Delta_{\perp} U - \frac{ik_0''}{2} \frac{\partial^2 U}{\partial t^2} - \frac{\sigma_e}{2} (1 - i\omega_0 \tau_0) T^{-1} \rho U + ik_0 n_2 T |U|^2 U - \frac{\beta^{(K)}}{2} |U|^{2K-2} U \quad (2.67)$$

In this model we limited to the second order dispersion relation obtained from a Taylor expansion around ω_0 and as a consequence of this, the operator T^{-1} in front of the chromatic dispersion will be neglected. Actually the operator T^{-1} introduces a space-time focusing in front of the diffraction term ($T^{-1} \Delta_{\perp} U$). The nonlinearities of the envelope function ($T |U|^2 U$) are also affected by the operator T corresponding physically to a self-steepening [97, 34, 94].

Equations (2.67) describe wave diffraction, Kerr focusing response, plasma absorption and defocussing, chromatic dispersion with a self-consistent action of deviation from the classical slowly-varying envelope approximation through space-time focusing and self-steepening operators respectively. In this dissertation, emphasis is laid on the spatial dynamics of the pulsed beams. Hence, for sake of simplicity, we limited at the second order dispersion and $T, T^{-1} \rightarrow 1$. These assumptions are justified by the slowly varying envelope approximation condition that we introduced at the beginning of this section. It follows from this that the final laser equations that our objective was to model is:

$$\frac{\partial U}{\partial z} = \frac{i}{2k_0} \Delta_{\perp} U - \frac{ik_0''}{2} \frac{\partial^2 U}{\partial t^2} - \frac{\sigma_e}{2} (1 - i\omega_0\tau_0) \rho U + ik_0 n_2 |U|^2 U - \frac{\beta^{(K)}}{2} |U|^{2K-2} U \quad (2.68)$$

2.4.2 Equation for the plasma generation in amorphous silica glass

The evolution equation for the electron plasma density is governed by a rate equation in the form [93, 98, 99]:

$$\frac{\partial \rho}{\partial t} = (W_{MPI} + W_{AI}) \rho_{nt} - \alpha_0 \rho^2 \quad (2.69)$$

where, W_{MPI} and W_{AI} denotes multiphoton (**MPI**) and avalanche ionization rate respectively whereas the quantity $(-\alpha_0 \rho^2)$ stand for radiative electron recombination. According to Keldysh theory, optical field ionization in the (**MPI**) regime occurs with a rate [94]:

$$W_{MPI} = \sigma_K I^K = \sigma_K |U|^{2K} \quad (2.70)$$

which is valid for the laser intensities in the range $10^{13} - 10^{14}$ W/cm². The rate for avalanche ionization is proportional to the pulse intensity:

$$W_{AI} = \frac{\sigma(\omega_0)}{n_0^2 E_g \rho_{nt}} \rho I = \frac{\sigma(\omega_0)}{E_g \rho_{nt}} \rho |U|^2 \quad (2.71)$$

Where $\sigma(\omega_0) \equiv \sigma_0$ is the cross section for inverse Bremsstrahlung evaluated at the central frequency ω_0 of the laser pulse and E_g is the ionization energy. Replacing equations (2.70) and (2.71) into (2.69) yields:

$$\frac{\partial \rho}{\partial t} = \left[\frac{\sigma(\omega_0)}{n_0^2 E_g \rho_{nt}} \rho |U|^2 + \sigma_K |U|^{2K} \right] \rho_{nt} - \alpha_0 \rho^2 \quad (2.72)$$

The ionization of the medium implies the absorption of a large number of photons, which means that $E_g = K\hbar\omega_0$. As we already mentioned above that in the limit of (**MPI**), we

have $\beta^K = K\bar{h}\omega_0\sigma_K\rho_{nt}$, which imply that, $\sigma_K\rho_{nt} = \beta^K/K\bar{h}\omega_0$. Taking this two last quantities into account, we rewrite equation (2.72) as:

$$\frac{\partial\rho}{\partial t} = \frac{\sigma_0}{n_0^2 E_g} \rho |U|^2 + \frac{\beta^{(K)}}{K\bar{h}\omega_0} |U|^{2K} - \alpha_0 \rho^2 \quad (2.73)$$

It is worth noticing that the plasma density ρ is also a slowly varying entity, like U . It does not take into account the fast small-scale motion (~ 1 nm) of the electrons. We assumed a free electron gas on a positive background. This background are the ions, which provide the shielding of the electron charges. Because the mass of the ions is ~ 30000 times the electron mass, we neglect ion motions and therefore their contribution to the evolution of plasma equation.

Equations (2.74) and (2.75) are the theoretical. From these coupled equations we shall derive easily the theoretical model dedicated to our study. Indeed those two last coupled equations must be supplemented with initial and boundary conditions.

$$\frac{\partial U}{\partial z} = \frac{i}{2k_0} \Delta_{\perp} U - \frac{ik_0''}{2} \frac{\partial^2 U}{\partial t^2} - \frac{\sigma_e}{2} (1 - i\omega_0\tau_0) \rho U + ik_0 n_2 |U|^2 U - \frac{\beta^{(K)}}{2} |U|^{2K-2} U \quad (2.74)$$

$$\frac{\partial\rho}{\partial t} = \frac{\sigma_0}{n_0^2 E_g} \rho |U|^2 + \frac{\beta^{(K)}}{K\bar{h}\omega_0} |U|^{2K} - \alpha_0 \rho^2 \quad (2.75)$$

In general, when the femtosecond laser have not yet interact with the fused silica material, we have $\rho(0) = 0$, which physically corresponds to the absence of free charges in the media. According to the intensity distribution at the boundary, it is usually given by either Gaussian or super-Gaussian beam shapes [100]:

$$U(0,t) = \xi_0 \exp\left(-\frac{r^{2N}}{w_0^{2N}} - ik_0 \frac{r^2}{2f} - \frac{t^2}{t_p^2}\right), \quad (2.76)$$

which may be focused through a lens of focal length f . Here, $r^2 = x^2 + y^2$, w_0 is the beam waist and t_p (the $1/e_0^2$ pulse half-width) is such that its full-width-at-half-maximum (FWHM) equals $\Delta t = \sqrt{2 \ln 2} t_p$. For Gaussian beams ($N = 1$), $\xi_0 = \sqrt{2P_{in}/\pi w_0^2}$ including the input power $P_{in} = \int |U|^2 d\vec{r}$. Under conditions of linear focusing, the input Gaussian beam comes to focus at longitudinal position $d = f/(1 + f^2/z_0^2)$, where $z_0^2 = \pi w_0^2 n_0/\lambda_0$ is the Reyleigh range (diffraction length of the collimated beam) of the input beam. The size of the laser beam w_f at the focus is $(w_f/w_0)^2 = (f^2/z_0^2)/(1 + f^2/z_0^2) = z_f/z_0$, with z_f the Reyleigh range of the focused beam.

2.4.3 Theoretical model

The model that we will be using in the next chapter is the dimensionless form of equations (2.74) and (2.75).

Dimensionless equations

To facilitate the analysis, it is often convenient to rescale the model equations and write them in a dimensionless form. For our system, we introduce the following scales [99, 100]:

$$t \longrightarrow t_p t, r \longrightarrow w_f r, z \longrightarrow 4z_f z, U \longrightarrow \sqrt{2P_{in}/\pi w_f^2} u, \rho \longrightarrow \rho_{BD} \rho$$

Where ρ_{BD} is the prescribed breakdown electron plasma density. The use of w_f and z_f as transverse and longitudinal length units, respectively, is appropriate because the pulse intensity is high near the focal point ($z = f$) where the plasma is expected to be generated in a volume of $2\pi w_f^2 z_f$. Introducing the above scales into equations (2.74) and (2.75) reads:

$$i \frac{\partial u}{\partial z} + \Delta_{\perp} u - \delta \frac{\partial^2 u}{\partial t^2} + \sigma |u|^2 u = -i\gamma_0 (1 - i\omega_0 \tau_0) \rho u - i\mu |u|^{2K-2} u \quad (2.77)$$

$$\frac{\partial \rho}{\partial t} = \nu |u|^2 \rho + \alpha |u|^{2K} - a \rho^2 \quad (2.78)$$

where,

$$\sigma = 8 \frac{P_{in}}{P_{cr}}, \delta = \frac{2k_0'' z_f}{t_p^2}, \gamma_0 = 2z_z \sigma_e \rho_{BD}, \mu = 2z_f \beta^{(K)} \left(\frac{2P_{in}}{\pi w_f^2} \right)^{K-1}, \nu = \frac{2\sigma_0 P_{in} t_p}{n_0^2 E_g \pi w_f^2}, a = \alpha_0 t_p \rho_{BD},$$

$$P_{cr} = \frac{\lambda_0^2}{2\pi n_0 n_2} \text{ and } \alpha = \frac{\beta^{(K)} t_p}{K \hbar \omega_0 \rho_{BD}} \left(\frac{2P_{in}}{\pi w_f^2} \right)^K.$$

To be more explicit on the physical meaning of each coefficients appearing in equations (2.77) and (2.78) as well as each term present in those two equations, we specify that z is the propagation distance, K is a photon number, t is the propagation time, τ_0 is the lifetime of the electron plasma, ω_0 is the plasma frequency [101], γ_0 is the strength of coupling of the electron plasma to the laser field, u is the normalized envelope of the laser field, ρ is the normalized plasma density [21], δ is the group-velocity dispersion coefficient with $\delta = \pm 1$ depending on whether the group-velocity dispersion is in the anomalous or normal regime respectively, σ is the kerr nonlinearity coefficient, ν is one photon-induced cascade ionization rate while α is the plasma balance rate due to K -photon absorptions, and μ is the strength of nonlinearity induced by multi-photon absorption processes. The first term in the right-hand-side of equation 2.77 accounts for the absorption and defocusing by plasma, while the second term accounts for

K -photon absorption. For the left-hand-side, the three first terms describes the diffraction, transverse modulations and dispersion of the laser field respectively during its propagation and the last term contribute for the Kerr effect. According to equation 2.78, the first term on the right-hand-side describes growth of the electron plasma by cascade (avalanche) ionization, whereas the second term is the contribution of multi-photon absorption (MPA), and the third term describes the electron-ion recombinations processes in the plasma. Actually, the electron-ion recombination phenomena contribute to the loss of the generation of free electrons for the further plasma and for the processes to occurs, two charged particles are requires thus its proportionality to ρ^2 in the above equation [36, 94, 97].

For the above model, its linear solution will represent the continuous-wave laser while its nonlinear solution will denote the pulsed laser (i.e. femtosecond laser).

2.5 Methodology

In the next chapter, we will examine the continuous-wave and femtosecond laser stability (i.e. spot) for different ranges of values of characteristic parameters of the model given in equations (2.77) and (2.78). In this goal we shall examine laser stability in this proposed model, taking into consideration multi-photon absorptions, plasma generation and radiative recombination processes. For a start, we shall examine laser stability in our model by neglecting the effects of radiative recombination processes in the plasma generated. Then the analysis will take into account the effect of radiative recombination on the continuous-wave laser stability. To do this, we will carry out a modulational instability analysis of the model starting from a continuous-wave input field in steady state, and explore the regions of cw stability and instability through a global spectral map generated for different sets of values of characteristic parameters of the model. This modulational instability technique will involve the linearization of the laser propagation equation around a continuous-wave (cw) input intensity, which leads to a linear-stability problem for which the Green-function technique, as well as the linear-matrix approach, contribute in the formulation of system stability. Our study will closely follow the standard analysis [102, 103], which rests on the assumption that pulses will be favoured in the regions where characteristic parameters of the model act against the stability of continuous-waves. However, the modulational instability analysis provides relevant information about

the self-starting conditions, but do not actually help identify the exact forms of the pulse and multiple-pulse structures stabilized in the pulsed regime [104]. The reason is that the modulational-instability method deals strictly with plane waves and its instability can only allow us to predict a distinct operation regime. To determine the exact structures governing the pulse regime, we must solve the complex Ginzburg-Landau equation (CGLE) numerically. In this respect, the dynamical approach must enable us to explore all the possible operation regimes inherent to the stability of the present model in the nonlinear regime. Therefore, in addition to the modulational instability analysis, we shall investigate the femtosecond laser dynamics and stability in the full nonlinear regime by transforming the model equations into a system of four equations of first order ordinary differential equation and solve it by means of fourth-order Runge-Kutta algorithm.

2.5.1 Fourth-order Runge Kutta algorithm

The most widely known member of the Runge Kutta family is generally referred to as "RK4", the "classic Runge-Kutta method" or simply as "the Runge-Kutta method".

Let an initial value problem be specified as follows [105]:

$$\frac{dy}{dt} = f(t,y), \quad y(t_0) = y_0. \quad (2.79)$$

Here y is an unknown function (scalar or vector) of time t , which we would like to approximate; we are told that dy/dt , the rate at which y changes, is a function of t and of y itself. At the initial time t_0 the corresponding y value is y_0 . The function f and the initial conditions t_0, y_0 are given. Now pick a step-size $h > 0$ and define:

$$y_{n+1} = y_n + \frac{1}{6}h (k_1 + 2k_2 + 2k_3 + k_4) \quad (2.80)$$

$$t_{n+1} = t_n + h, \quad \text{for } n = 0,1,2,3,\dots, \quad (2.81)$$

using:

$$k_1 = f(t_n, y_n) \quad (2.82)$$

$$k_2 = f\left(t_n + \frac{h}{2}, y_n + h\frac{k_1}{2}\right) \quad (2.83)$$

$$k_3 = f\left(t_n + \frac{h}{2}, y_n + h\frac{k_2}{2}\right) \quad (2.84)$$

$$k_4 = f(t_n + h, y_n + hk_3). \quad (2.85)$$

Here y_{n+1} is the RK4 approximation of $y(t_{n+1})$, and the next value y_{n+1} is determined by the present value y_n plus the weighted average of four increments, where each increment is the product of the size of the interval, h , and an estimated slope specified by function f on the right-hand side of the differential equation.

- ☞ k_1 is the slope at the beginning of the interval, using y (Euler's method);
- ☞ k_2 is the slope at the midpoint of the interval, using y and k_1 ;
- ☞ k_3 is again the slope at the midpoint, but now using y and k_2 ;
- ☞ k_4 is the slope at the end of the interval, using y and k_3 .

In averaging the four slopes, greater weight is given to the slopes at the midpoint. If f is independent of y , so that the differential equation is equivalent to a simple integral, then RK4 is Simpson's rule. The RK4 method is a fourth-order method, meaning that the local truncation error is on the order of $O(h^5)$, while the total accumulated error is on the order of $O(h^4)$.

In many practical applications the function f is independent of t (so called autonomous system, or time-invariant system, especially in physics), and their increments are not computed at all and not passed to function f , with only the final formula for t_{n+1} used.

Our theoretical model is a function of the parameter K , which represent the number of absorbed photon in the process of femtosecond laser inscription. Because amorphous silica glass required the absorption of two photon (i.e. $K = 2$), from the laser beam to break its chemical bond and that we have found that for the case of our study the maximum number photon required to promote an electron in the conduction band of amorphous silica glass is $K = 5$. Therefore, within chapter 3, we shall be varied K as $K = 2,3,4,5$.

In this chapter, we have introduce some important properties of amorphous silica glass. We also built the theoretical model of femtosecond laser as well as the model described the time evolution of the plasma density induce by this laser in the amorphous silica material. The coupled equations (2.77) and (2.78) will be used to optimize the process of femtosecond laser inscription on amorphous silica within chapter 3.

Results and Discussion

Our main objective in this chapter is to explore analytically and numerically, conditions under which the laser will be stable while operating in the continuous wave regime or in the pulse regime for the above model given by equations (2.77) and (2.78). In this goal, we are going to separate this chapter in three main parts. In the first part, we will first of all neglect the radiative recombination process in the plasma equation (i.e. $-a\rho^2$), then we shall examine the stability of the new model obtained by means of the modulational instability approach. Actually, for this model, the modulational instability analysis stands for the most reliable analytical approach by which the laser stability can be effectively singled out in the distinct possible regimes of its operation. For the second part, an improvement of this theoretical model will be attempted to take into consideration physical processes which were ignored in the first part of our investigation in this chapter, i.e. the radiative recombination phenomena ($-a\rho^2$). This second part will be followed by the third part where, we will be investigated on the nonlinear solution of the model. To follow the ultimate goal of our study, in the full nonlinear regime an ansatz will be introduced to represent the femtosecond laser as a pulse field with a real amplitude and real phase. With the help of this ansatz the system dynamics will be transformed into a set of four first-order ordinary differential equations. This set of first-order ordinary differential equations will be solved numerically using a fourth-order Runge-Kutta algorithm. In this goal, we shall be plotted dynamical quantities of the model for different values of radiative recombination coefficient \mathbf{a} starting with $\mathbf{a}=\mathbf{0}$ (i.e. when there is no radiative recombination).

3.1 Stability investigation of the continuous-wave laser inscription on amorphous silica glass in the presence of plasma generation

3.1.1 Model without recombination processes in the plasma generated

Ignoring transverse modulations of the optical field for simplicity (but without loss of generality), in equations (2.77) and (2.78), it follows from this that the model dedicated to the study of the first part of this chapter is given by:

$$i\frac{\partial u}{\partial z} - \delta\frac{\partial^2 u}{\partial t^2} + \sigma|u|^2u = -i\gamma_0(1 - i\omega_0\tau_0)\rho u - i\mu|u|^{2K-2}u \quad (3.1)$$

$$\frac{\partial \rho}{\partial t} = \nu|u|^2\rho + \alpha|u|^{2K} \quad (3.2)$$

3.1.2 Steady states solutions of the laser in the continuous-wave regime

We seek for the solutions of the two above coupled equations (3.1) and (3.2). In general, there will be a two possibles solutions, namely continuous-wave solutions and pulsed-wave solutions. For this section, we shall be dealing with the continuous-wave solutions of the above model in which its stability will be examined starting from the steady states. To investigate the continuous-wave solutions let us rewrite the optical field in steady state as:

$$u(z) = \sqrt{I_0} \exp(iqz), \quad \rho = \rho_0, \quad (3.3)$$

where $\rho = \rho_0$ is the plasma density in the steady state, I_0 is the continuous-wave input power and q is the wavenumber. Replacing this into equations (3.1) and (3.2) yields:

$$-q\sqrt{I_0} + \sigma I_0\sqrt{I_0} = -i\gamma_0(1 - i\omega_0\tau_0)\rho_0\sqrt{I_0} - \mu I_0^{K-1}\sqrt{I_0} \quad (3.4)$$

$$\rho_0 = -\frac{\alpha}{\nu} I_0^{K-1} \quad (3.5)$$

From equation (3.4), we obtain:

$$-q + \sigma I_0 = -i\gamma_0\rho_0 - \gamma_0\omega_0\tau_0\rho_0 - i\mu I_0^{K-1} \quad (3.6)$$

Equation (3.6) can be written as:

$$(-q + \sigma I_0 + \gamma_0 \omega_0 \tau_0 \rho_0) + i(\gamma_0 \rho_0 + \mu I_0^{K-1}) = 0 \quad (3.7)$$

Equation (3.7) is a complex equation which is zero iff the real part and the imaginary part are both equal to zero. It follows from this property that equation (3.7) becomes:

$$\begin{cases} -q + \sigma I_0 + \gamma_0 \omega_0 \tau_0 \rho_0 & = 0 \\ \gamma_0 \rho_0 + \mu I_0^{K-1} & = 0 \end{cases} \quad (3.8)$$

thus,

$$q = \sigma I_0 + \gamma_0 \omega_0 \tau_0 \rho_0. \quad (3.9)$$

Actually, the steady states of the propagation equations (3.1) and (3.2) correspond to a laser field and plasma density with time and space independent amplitudes. This means that:

$$\frac{\partial u}{\partial z} \Big|_{u=u_0} = 0 \quad \text{and} \quad \frac{\partial u}{\partial t} \Big|_{u=u_0} = 0 \quad (3.10)$$

Taking these two condition into equations (3.1) and (3.2) reads:

$$\sigma |u_0|^2 u_0 = -i\gamma_0 (1 - i\omega_0 \tau_0) \rho_0 u_0 - i\mu |u_0|^{2K-2} u_0 \quad (3.11)$$

$$\rho_0 = -\frac{\alpha}{\nu} |u_0|^{2K-2} \quad (3.12)$$

Substituting equation (3.12) into equation (3.11) yields:

$$\sigma |u_0|^2 - \frac{\alpha \gamma_0 \omega_0 \tau_0}{\nu} |u_0|^{2K-2} + i \left(\mu - \frac{\alpha \gamma_0}{\nu} \right) |u_0|^{2K-2} = 0 \quad (3.13)$$

Separating real part from the imaginary part, equation (3.13) gives rise to:

$$\sigma |u_0|^2 - \frac{\alpha \gamma_0 \omega_0 \tau_0}{\nu} |u_0|^{2K-2} = 0 \quad (3.14)$$

$$\mu - \frac{\alpha \gamma_0}{\nu} = 0 \quad (3.15)$$

Clearly, equation (3.15) suggests that $\alpha \gamma_0 = \mu \nu$. Equation (3.14) yields:

$$|u_0|^{2K-4} = \frac{\sigma \nu}{\alpha \gamma_0 \omega_0 \tau_0} \implies |u_0|^2 = \left(\frac{\sigma \nu}{\alpha \gamma_0 \omega_0 \tau_0} \right)^{\frac{1}{K-2}} \quad (3.16)$$

Defining an input power $I_0 = |u_0|^2$, equation (3.1) suggests that for a continuous-wave to be stable in steady state the input power I_0 should fulfill the condition:

$$I_0 = \left(\frac{\sigma \nu}{\alpha \gamma_0 \omega_0 \tau_0} \right)^{\frac{1}{K-2}} \quad (3.17)$$

The above condition leads to the following expression for the steady-state plasma density:

$$\begin{aligned} \rho_0 &= -\frac{\alpha}{\nu} |u_0|^{2K-2} \\ &= -\frac{\mu}{\gamma_0} \left(\frac{\sigma\nu}{\alpha\gamma_0\omega_0\tau_0} \right)^{\frac{K-1}{K-2}}, \end{aligned} \quad (3.18)$$

a relation valid provided $\alpha\gamma_0 = \mu\nu$ (which follows from the requirement that I_0 must be always real). According to formula (3.9), at steady state the cw modulation wavenumber q is fixed by the input intensity I_0 as well as the equilibrium plasma density ρ_0 . Since these two quantities appear to be completely determined by characteristic parameters of the model, q too should be fixed by characteristic parameters of amorphous silica glass.

From the minus sign in the expression of ρ_0 given by formula (3.18), we infer that characteristic parameters of the coupled set (3.1) and (3.2) cannot be chosen of arbitrary signs. Indeed values of δ , σ and γ_0 considered in ref. [21] were all positive, however the Kerr coefficient σ can readily be fixed in the positive branch, whereas the group-delay dispersion δ may also assume negative values corresponding to an anomalous dispersion regime. In this case, the propagation equation (3.1) can be assimilated with an inhomogeneous self-focusing Nonlinear Schrödinger equation with complex coefficients [106, 107] the nonlinear solution of which is a pulse soliton. However, μ , α and γ_0 can be chosen unconditionally positive or negative although formula (3.18) imposes that α and ν should be of opposite signs, while μ can be chosen negative provided γ_0 is positive. It is also instructive to stress, concerning the presence of the term proportional to μ in the propagation equation (3.1), that this term accounts for a nonlinear gain generated by multiphoton absorption processes. Physical contexts with $K = 2$ are common in mode-locked laser systems with fast saturable absorbers (see e.g. [103, 108, 109, 110]).

The presence of the multiphoton ionization coefficient μ in equation (3.18) is equally of great physical significance, indeed it suggests that the plasma density at the steady state is an increasing function of the multiphoton parameter K . This parameter also appears to affect the continuous-wave field intensity, as evidenced by formula (3.1). More explicitly equation (3.1) shows that depending on values of characteristic parameters of the model, multiphoton ionization processes will lower or increase the threshold input power required for laser operation in the continuous-wave regime.

3.1.3 Continuous-wave laser frequency in the steady state

The continuous-wave laser energy required to promote an electron in the conduction band of amorphous silica with bandgap $E_g = 7.6$ eV is given by:

$$K\hbar\omega_l = E_g \implies \omega_l = \frac{2\pi E_g}{Kh} \quad (3.19)$$

It follows from equation (3.19) that a Continuous-wave laser frequency in the steady state is:

$$\omega_l = \frac{2 \times 3.14 \times 7.6 \times 1.6 \times 10^{-19}}{5 \times 6.62 \times 10^{-34}} \quad (3.20)$$

$$= 2.3 \text{ rad/s} \quad (3.21)$$

$$= 2.3 \times 10^{-15} \text{ rad/fs} \quad (3.22)$$

3.1.4 Laser fluence in the steady state

The femtosecond laser fluence also known as energy density in the steady state is given by [2]:

$$F(z) = (1 - R)F_0 e^{-\beta_n z}, \quad (3.23)$$

where, $\beta_n = 1.8 \pm 0.4 \times 10^{-5} \text{ cm}^{-1}$ [89] is the absorption coefficient of amorphous silica, R is the small laser beam reflectivity on this material surface, z is the local coordinate perpendicular to the surface of amorphous silica and F_0 is the maximum laser fluence at the surface of the material targeted by the present study. The maximum laser fluence is given by:

$$F_0 = \frac{I_0}{S_0} T = \left(\frac{\sigma \nu}{\alpha \gamma_0 \omega_0 \tau_0} \right)^{\frac{1}{K-2}} T \quad (3.24)$$

where I_0 is the above input power, T is the time interval over which the continuous wave laser interacts with amorphous silica and $S_0 = 1 \text{ cm}^2$ is the area where the laser radiation is focusing. Introducing equation (3.24) into (3.23) we obtain the continuous wave laser fluence at the steady state as:

$$F(z) = (1 - R) \left(\frac{\sigma \nu}{\alpha \gamma_0 \omega_0 \tau_0} \right)^{\frac{1}{K-2}} T e^{-\beta_n z}. \quad (3.25)$$

The focusing system controls the laser beam spot size on amorphous silica is an important system part. The area diameter of the focused laser beam defined engraving line width and the real engraving efficiency and the penetrating depth of the laser beam. The diameter depends on the lens focal length and the laser beam deviation. Actually the origin of the laser

beam deviation is the presence of the plasma generated during the laser inscription process. However, this plasma perturbed and induced the instability of the laser during engraving process. Theoretically this can be translated into a modulational-instability analysis in which the laser stability is evaluated through a small perturbation parameter whose amplitude growth enough to destabilized the laser beam during inscription on amorphous silica. To this aim, in the next section we shall discuss the stability of the continuous-wave laser in steady state, considering a small perturbation which amplitude can grow or decreases in time.

3.1.5 Modulational-instability analysis of the laser in the continuous-wave regime

A modulational instability analysis is a theory in which a uniform train of oscillatory waves of moderate amplitude loses energy to a small perturbation with nearly the same frequency and direction in the steady state. To investigate the stability of the continuous-wave field and the plasma density in their steady states, we consider a small-amplitude perturbation such that solutions to equation (3.1) and equation (3.2) can be rewritten as:

$$u(z,t) = [u_0 + a_1(z,t)] \exp(iqz), \quad (3.26)$$

$$\rho(t) = \rho_0 + \tilde{\rho}(t), \quad (3.27)$$

where $a_1(z,t)$ and $\tilde{\rho}$ are the small-amplitude perturbation coupled to the steady-state continuous-wave laser field and the plasma density, respectively. Substituting formula (3.27) into equations (3.1) and (3.2) reads:

$$i \frac{\partial u}{\partial z} - \delta \frac{\partial^2 u}{\partial t^2} + \sigma |u|^2 u = -i\gamma (1 - i\omega_0 \tau_0) [\rho_0 + \tilde{\rho}(t)] u - i\mu |u|^{2K-2} u \quad (3.28)$$

$$\frac{\partial \rho}{\partial t} = \nu |u|^2 [\rho_0 + \tilde{\rho}(t)] + \alpha |u|^{2K} \quad (3.29)$$

The linearization of equations (3.28) and (3.29) around u_0 are:

$$|u|^2 = (u_0 + a_1)(u_0 + a_1^*) \approx [u_0^2 + u_0(a_1 + a_1^*)] \quad (3.30)$$

$$|u|^2 u \approx [u_0^3 + u_0^2(2a_1 + a_1^*)] e^{iqz} \quad (3.31)$$

$$|u|^{2K-2} u \approx u_0^{2K-2} [u_0 + Ka_1 + (K-1)a_1^*] e^{iqz} \quad (3.32)$$

$$|u|^{2K} \approx u_0^{2K} + K(a_1 + a_1^*)u_0^{2K-1} \quad (3.33)$$

Replacing these above quantities given by formula (3.30), (3.31), (3.32) and (3.33) into equations (3.28) et (3.29) yields:

$$i \frac{\partial a}{\partial z} - \delta \frac{\partial^2 a}{\partial t^2} + (a_1 + a_1^*) \Gamma_K^{(1)} + i\gamma_0(1 - i\omega_0\tau_0)u_0\tilde{\rho} = 0, \quad (3.34)$$

$$\frac{\partial \tilde{\rho}}{\partial t} = \nu u_0^2 \tilde{\rho} + \Gamma_K^{(2)}(a_1 + a_1^*), \quad (3.35)$$

where, $\Gamma_K^{(1)} = \sigma u_0^2 + i\mu(K-1)u_0^{2(K-1)}$ and $\Gamma_K^{(2)} = \frac{\mu\nu}{\gamma_0}(K-1)u_0^{2K}$.

The first-order linear inhomogeneous equation (3.35) is solved by means of Green's function. Actually, for this case the Green function can be defined as:

$$G(t, t') = H(t - t') \exp[-\nu u_0^2(t' - t)], \quad (3.36)$$

where $H(t - t')$ is the Heaviside function satisfying the following properties:

$$H(t - t') = \begin{cases} 1 & \text{if } t > t' \\ 0 & \text{if } t < t' \end{cases} \quad (3.37)$$

Therefore it follows from this technique that the solution of the linear inhomogeneous equation (3.35) can be written as:

$$\begin{aligned} \tilde{\rho}(t) &= \Gamma_K^{(2)} \int_{-\infty}^t G(t, t')(a_1 + a_1^*) dt' \\ \tilde{\rho}(t) &= \Gamma_K^{(2)} \int_{-\infty}^t H(t - t') \exp[-\nu u_0^2(t' - t)] (a_1 + a_1^*) dt' \\ \tilde{\rho}(t) &= \Gamma_K^{(2)} \int_{-\infty}^t (a_1 + a_1^*) \exp[-\nu u_0^2(t' - t)] dt', \quad \text{for } t > t'. \end{aligned} \quad (3.38)$$

We formally choose the perturbation parameter in the following form:

$$a_1(z,t) = A_1 \exp(\kappa z + i\Omega t), \quad a_1^*(z,t) = A_2 \exp(\kappa z + i\Omega t), \quad (3.39)$$

where a_1^* is its complex conjugate. κ in the above is the spatial amplification coefficient of the perturbation coupled to the amplitude of the steady-state cw laser, and Ω is the perturbation modulation frequency. By introducing the above form of the cw laser perturbation parameters into equation (3.38), we find:

$$\tilde{\rho}(t) = \frac{(A_1 + A_2)\Gamma_K^{(2)}}{i\Omega - \nu u_0^2} \exp(\kappa z + i\Omega t) \quad (3.40)$$

Because of the presence of the complex conjugate of a^* in the linear equation (3.34), we must take into consideration the complex conjugate of this equation, which is:

$$-i \frac{\partial a_1^*}{\partial z} - \delta \frac{\partial^2 a_1^*}{\partial t^2} - (a_1 + a_1^*)\Gamma_K^{(1)*} - i\gamma_0(1 + i\omega_0\tau_0)u_0\tilde{\rho} = 0, \quad (3.41)$$

Substituting formula (3.40) and (3.39) into equations (3.34) and (3.41), we obtain the following 2×2 matrix equation for the perturbation amplitudes $A_{1,2}$:

$$\begin{aligned} \kappa \begin{pmatrix} A_1 \\ A_2 \end{pmatrix} &= \left[\begin{pmatrix} M_1 & M_2 \\ M_2^* & M_1^* \end{pmatrix} - M_0 \begin{pmatrix} 1 & 1 \\ 1 & 1 \end{pmatrix} \right] \begin{pmatrix} A_1 \\ A_2 \end{pmatrix} \\ &- P \begin{pmatrix} N_1 & N_1 \\ N_1^* & N_1^* \end{pmatrix} \begin{pmatrix} A_1 \\ A_2 \end{pmatrix}, \end{aligned} \quad (3.42)$$

in which:

$$M_1 = i(\delta\Omega^2 + \sigma u_0^2), \quad M_2 = i\sigma u_0^2, \quad (3.43)$$

$$\begin{aligned} M_0 &= \mu(K-1)u_0^{2(K-1)}, \\ P &= \frac{\gamma_0\Gamma_K^{(2)}}{i\Omega - \nu u_0^2}, \quad N_1 = 1 - i\omega_0\tau_0. \end{aligned} \quad (3.44)$$

The secular equation of the above matrix equation, which is a quadratic polynomial in κ , admits the following two possible roots:

$$\begin{aligned} \kappa_{1,2} &= -\mu(K-1)u_0^{2(K-1)} \left(1 - \frac{\nu u_0^2}{\nu u_0^2 - i\Omega} \right) \\ &\pm \sqrt{(M_0 + P)^2 - (\delta\Omega^2 + \sigma u_0^2)^2 - 2P\delta\Omega^2\omega_0\tau_0 + \sigma^2 u_0^4}, \end{aligned} \quad (3.45)$$

By considering the expressions of M_0 and P above, we obtained:

$$M_0 + P = \mu(K - 1)u_0^{2K-2} \left(1 - \frac{\nu u_0^2}{\nu u_0^2 - i\Omega} \right) \quad (3.46)$$

Equation (3.46) into formula (3.45) yields:

$$\begin{aligned} \kappa_{1,2} = & -\mu(K - 1)u_0^{2(K-1)} \left(1 - \frac{\nu u_0^2}{\nu u_0^2 - i\Omega} \right) \\ & \pm \sqrt{\left[\mu(K - 1)u_0^{2K-2} \left(1 - \frac{\nu u_0^2}{\nu u_0^2 - i\Omega} \right) \right]^2 - (\delta\Omega^2 + \sigma u_0^2)^2 - 2P\delta\Omega^2\omega_0\tau_0 + \sigma^2 u_0^4}, \end{aligned} \quad (3.47)$$

where subscripts 1 and 2 refer to the plus and minus signs respectively. As they stand the two eigenvalues $\kappa_{1,2}$ are functions of several parameters, making their interpretation a cumbersome though eventually a physically rich problem. In the subsequent analysis we intend to proceed step by step by considering characteristic parameters of importance in the model, and examining their specific physical influences on the cw stability in different ranges of values of the modulation frequency Ω . However before we proceed to this analysis, it is interesting to remark that at zero modulation frequency (i.e. $\Omega = 0$) the two eigenvalues are zero. This means that the perturbation amplitudes in this case are constant and therefore the cw regime is expected to be always stable. For nonzero values of the modulation frequency, the problem of cw stability is more subtle as we already argued. In general the problem will strongly depend on values (including signs) of the model parameters. To this last point, we emphasized that for negative values of the group-delay dispersion δ (i.e. in the anomalous dispersion regime) equation (3.1) is equivalent to a perturbed Nonlinear Schrödinger equation, where the perturbation coefficients include real and complex parameters. So the nonlinear solution to the field equation in this case is dominantly either a sech-type pulse [106] or a periodic pulse lattice of pulses [111, 112], which characteristic parameters (average amplitude, duration and repetition rate) are modulated by the perturbations [113, 107]. On the contrary if the dispersion is normal (i.e. when δ is positive), the nonlinear optical medium will be self-defocusing and physical conditions become unstable for sech structures. Nevertheless such conditions favor pulse-soliton boundstates such as dark soliton structures (see e.g. [114]).

The main information suggested by the above discussion is that to gain a substantial insight onto the continuous-wave stability at non-zero modulation frequency, we must treat the two distinct physical contexts of anomalous and normal dispersions. We shall follow an analysis which involves a broad range of values of the modulation frequency, hence leading to a

global mapping of the two eigenvalues in the parameter space $Re(\kappa) - Im(\kappa)$ where Re and Im refer to real and imaginary parts of their argument, respectively. All our analysis will be done in the frequency range $-5 \leq \Omega \leq 5$, while we fix $\gamma_0 = 0.1$ and $\sigma = 0.8$. Other characteristic parameters appearing in equations (3.1) and (3.2) will be varied.

Effects of changing sign of the group-delay dispersion

Figures 3.1 and 3.2 are parametric maps of κ_1 (full curve) and κ_2 (dashed curve) corresponding to $\delta < 0$ and $\delta > 0$ respectively, for four different values of K namely $K = 2, 3, 4, 5$. Here the avalanche coefficient was fixed to $\nu = 0.5$, and values of other characteristic parameters are given in the captions.

According to Fig. 3.1, continuous-wave will be stabilized by small values of the multiphoton parameter K (two top graphs and the left bottom graph). As K increases the continuous-wave regime gets gradually destabilized, on the figure one can notice that when $K = 5$, the real and imaginary parts of the two eigenvalues are both strictly positive suggesting an exponential growth of the perturbation amplitude. Oppositely, when $\delta > 0$ the continuous-wave regime will be unstable for any value of K . Note the small windows around the origin of the parametric map and growing as K increases, which simply reflects the cw stability we discussed earlier in the case of zero modulation frequency. The widening of this windows with increasing K suggests the possibility of a stable cw mode at nonzero, but extremely small values of the modulation frequency Ω when K becomes very large values.

Effects of varying the avalanche coefficient ν

To look at the effects of varying the avalanche coefficient ν on the cw stability, in Figs. 3.3 and 3.4 we represent the parametric maps now considering a smaller value of this coefficient i.e. $\nu = 0.05$. On observation of Figs. 3.3 and 3.4 it is transparent that decreasing ν creates favorable condition for cw modes, moreover the cw stability is seen to be strengthened by an increase of K .

Influence of the plasma frequency ω_0

Analytical expressions of the two eigenvalues $\kappa_{1,2}$ in formula (3.45), indicate that changing the value of ω_0 for fixed values of other parameters, can result in the change of sign of the

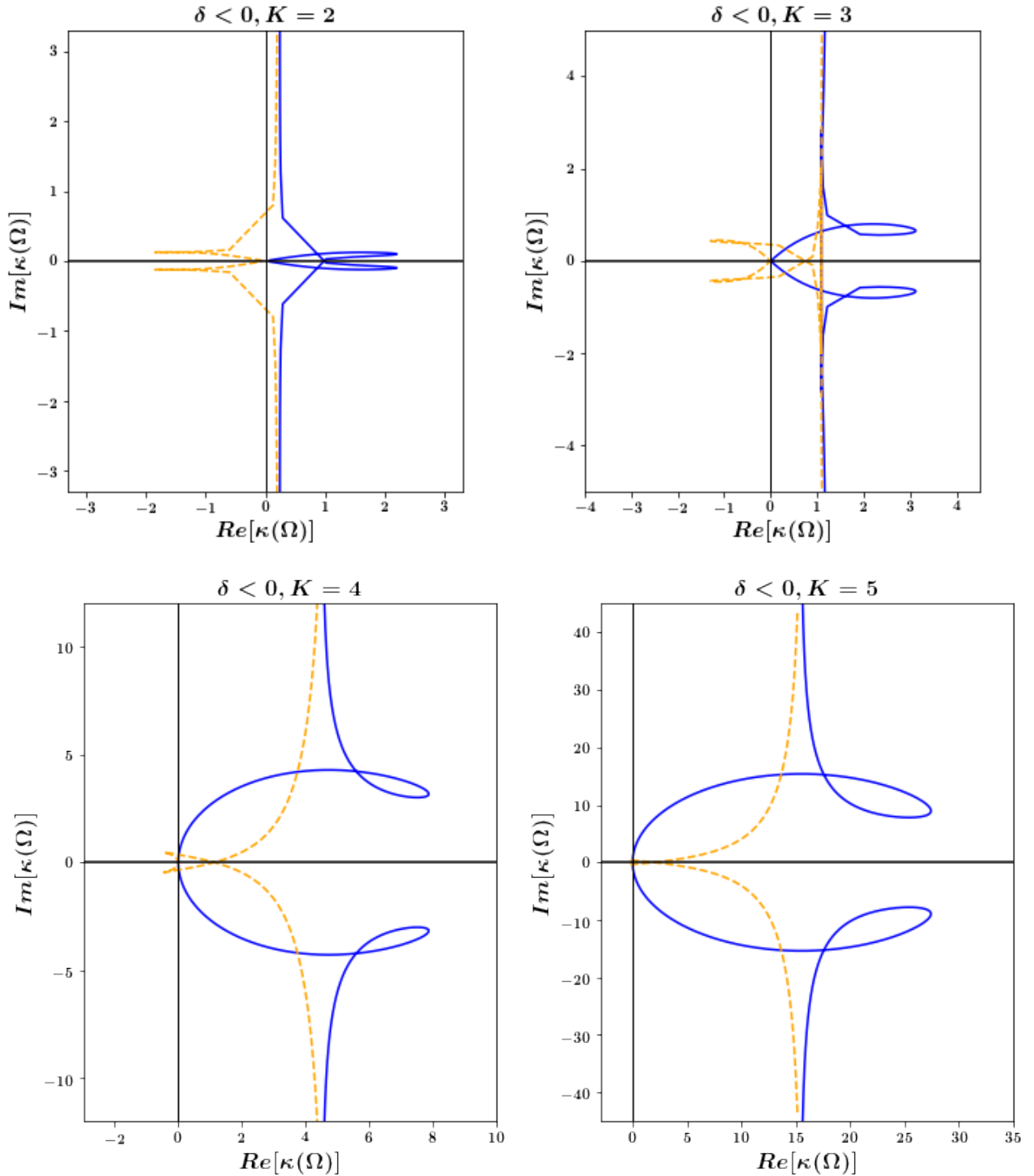


Figure 3.1: Imaginary versus real parts of κ_1 (full curve) and κ_2 (dashed curve), for $I_0 = 2.5$, $\nu = 0.5$, $\gamma_0 = 0.1$, $\omega_0\tau_0 = 0.2$, $\sigma = 0.8$, $\mu = -0.1$ and $\delta = -0.5$. The four graphs are for $K = 2, 3, 4, 5$, as indicated in the graphs.

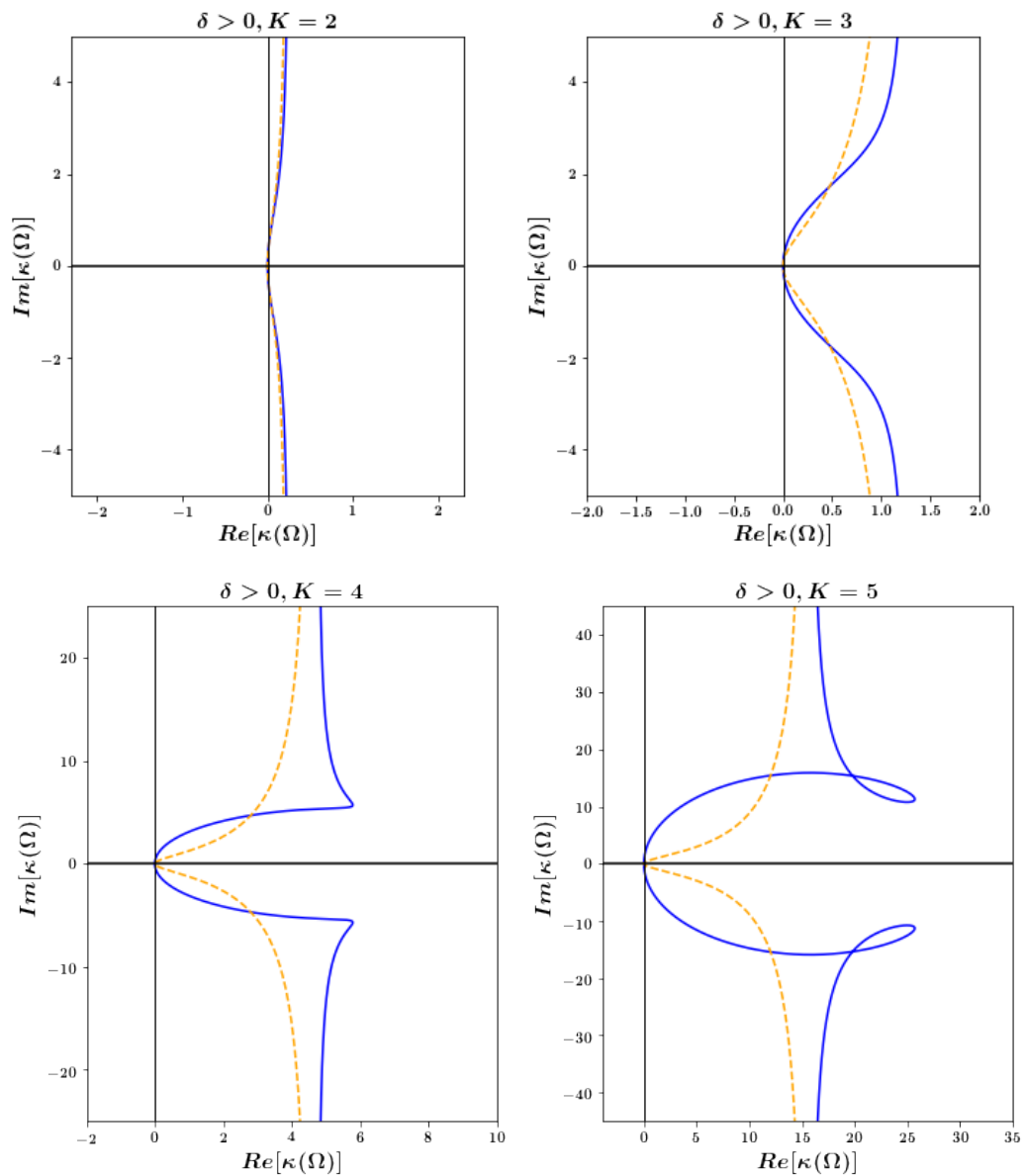


Figure 3.2: Imaginary versus real parts of κ_1 (full curve) and κ_2 (dashed curve), for $K = 2, 3, 4, 5$. Other parameter values are $I_0 = 2.5$, $\nu = 0.5$, $\gamma_0 = 0.1$, $\omega_0\tau_0 = 0.2$, $\sigma = 0.8$, $\mu = -0.1$ and $\delta = 0.5$.

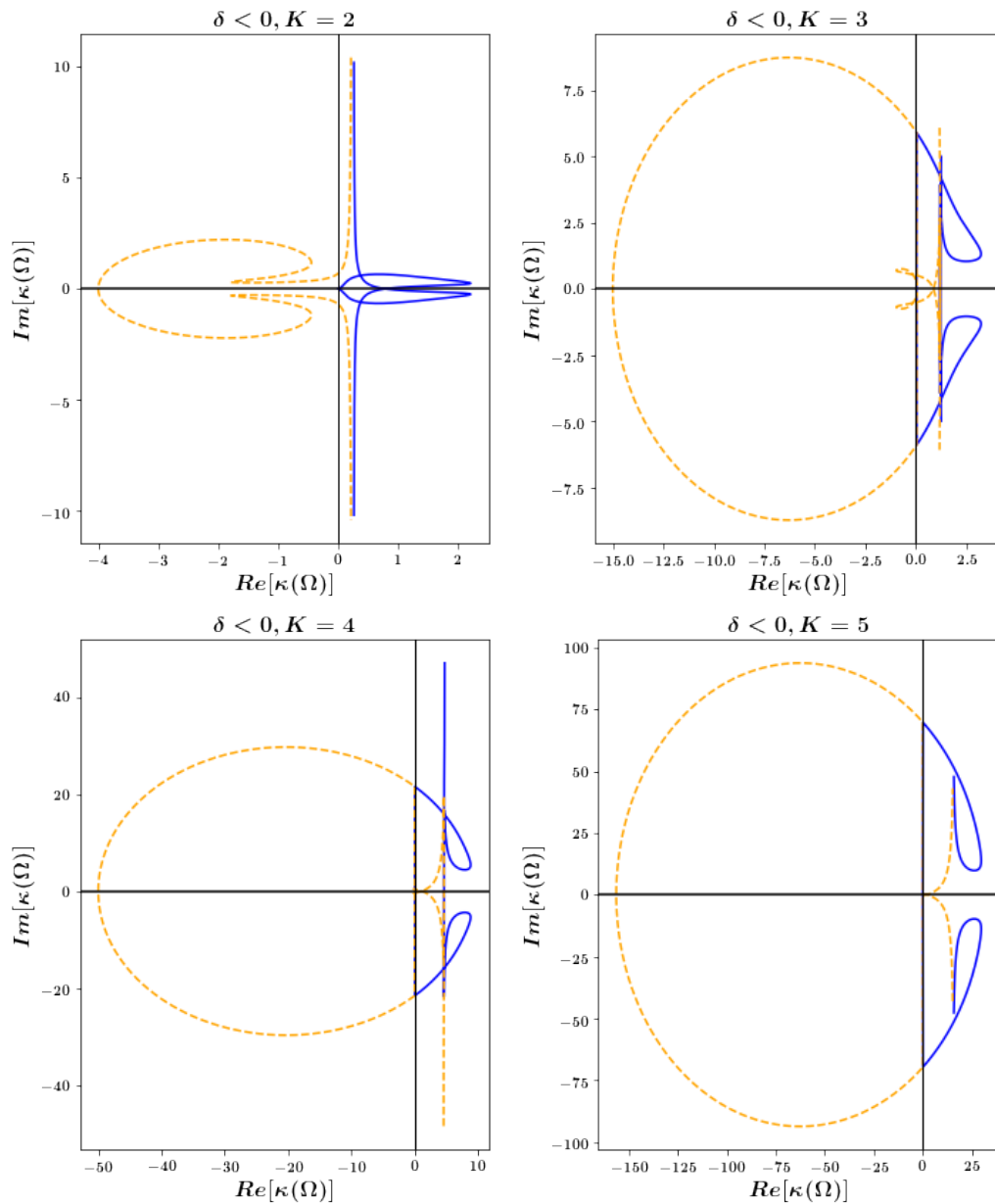


Figure 3.3: Imaginary versus real parts of κ_1 (full curve) and κ_2 (dashed curve), for $K = 2, 3, 4, 5$. Other parameter values are $I_0 = 2.5$, $\nu = 0.05$, $\gamma_0 = 0.1$, $\omega_0\tau_0 = 0.2$, $\sigma = 0.8$, $\mu = -0.1$ and $\delta = -0.5$.

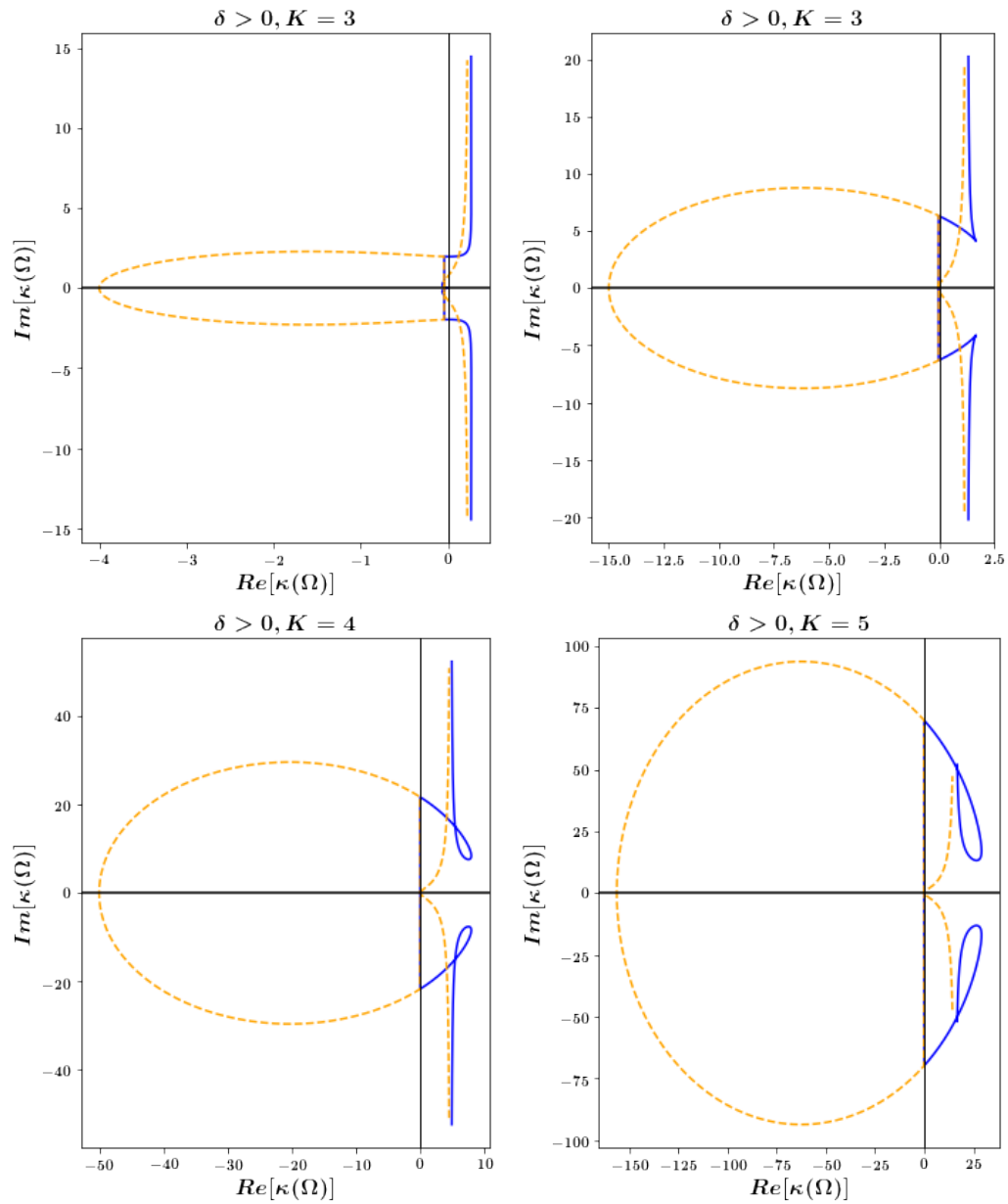


Figure 3.4: Imaginary versus real parts of κ_1 (full curve) and κ_2 (dashed curve), for $K = 2, 3, 4, 5$. Other parameter values are $I_0 = 2.5$, $\nu = 0.05$, $\gamma_0 = 0.1$, $\omega_0\tau_0 = 0.2$, $\sigma = 0.8$, $\mu = -0.1$ and $\delta = 0.5$

quantity in the square root. This means that the plasma frequency could stand for another possible relevant physical parameter of the model. To gain sight of what its variation entails on the cw stability, the parametric maps were generated for a relatively larger value of this parameter, $\omega_0 = 0.44$ rad/fs. Results are presented in figure 3.5 in the case of anomalous dispersion ($\delta = -0.5$), and figure 3.6 for the normal dispersion ($\delta = 0.5$). Graphs of figure 3.5 display behaviours which are fairly qualitatively similar to the behaviours observed in figure 3.1, except for some differences in shape profiles of the curves. However the physical interpretations of the two figures are the same. On the other hand figure 3.6 is quite suggestive of a stable continuous-wave regime for all the values of K we have chosen. In fact the later behaviours can be understood that at relatively high values of the plasma frequency in the normal dispersion regime and positive μ , cw modes will be always favored. As the four graphs of figure 3.6 suggest the continuous-wave regime will be more and more stable as K increases.

3.1.6 Summary

At zero modulation frequency of the perturbation parameter, the laser in continuous-wave regime will be always stable irrespective of values of characteristic parameters of the model. In this case the desire size of the characters will be possible to engrave on amorphous silica. At non-zero modulation frequency, when $\delta < 0$ as shown in figure 3.1, continuous-wave is stabilized by small values of photon number K . As K increases the cw regime gets gradually destabilized. This means that, when the absorption is low (i.e. $K = 2, 3$), the characters started forming on amorphous silica and when the photon number increases gradually (i.e. $K = 4$) the size of the character start to reduce and becomes very small when the photon number is large (i.e. $K = 5$). However, when $\delta > 0$ as shown in figure 3.2, the continuous-wave is always unstable then, engraving on amorphous silica in the continuous-wave mode is not possible for this case and therefore it is not possible to obtain the desire size of engraving characters that required the continuous-wave laser inscription. According to figures 3.3 and 3.4, the cw stability is seen to be strengthened by an increase of K . This means that it is possible to engrave the desire size of characters on amorphous silica in the continuous-wave regime. On figure 3.5 in the case of anomalous dispersion ($\delta < 0$), the graphs display the behaviours which are fairly qualitatively similar to the behaviours observed in figure 3.1, except for some differences in shape profiles of the curves. Therefore, the interpretations of the two figures are the same. On the other hand,

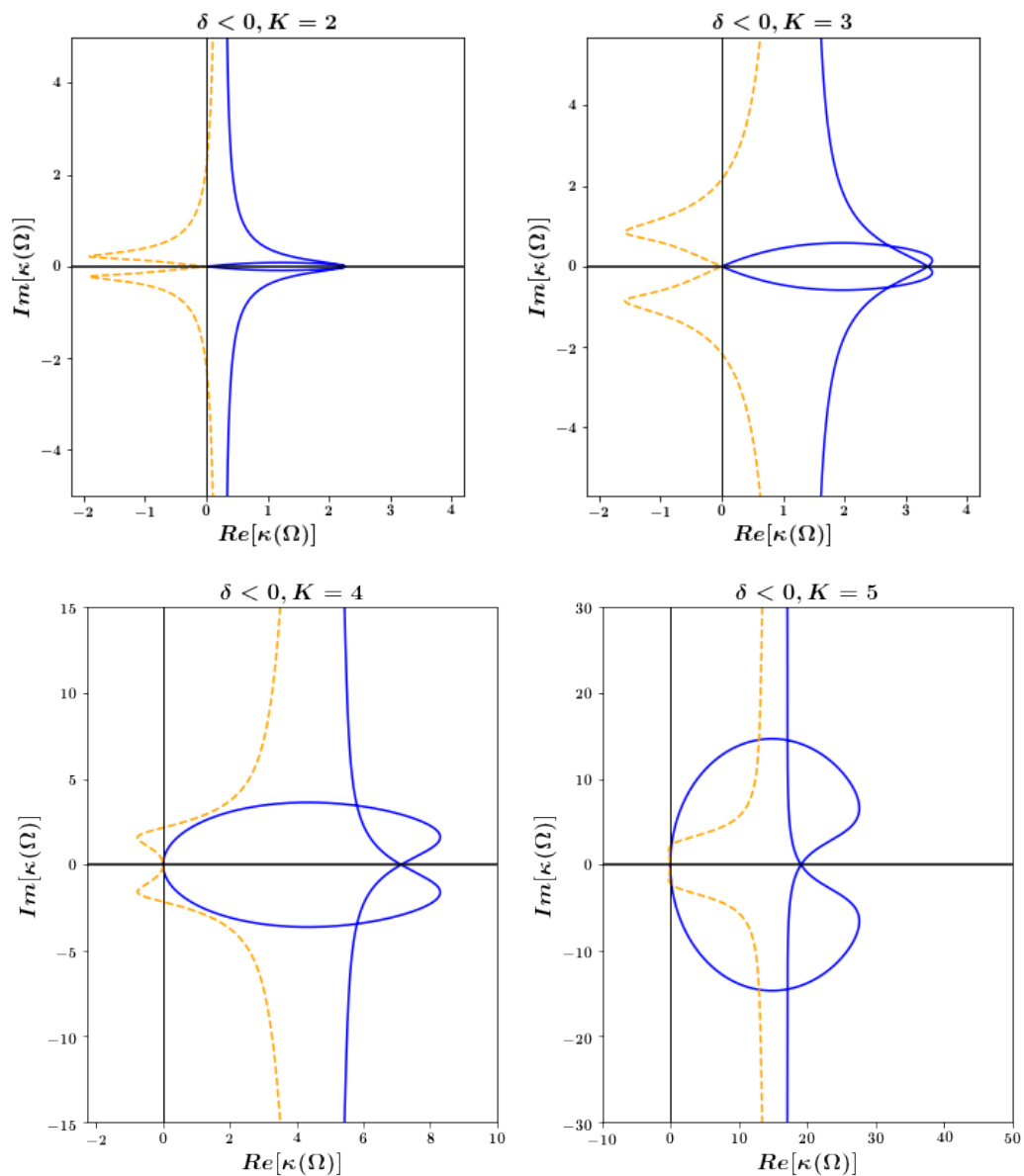


Figure 3.5: Imaginary versus real parts of κ_1 (full curve) and κ_2 (dashed curve), for $K = 2, 3, 4, 5$. Other parameter values are $I_0 = 2.5$, $\nu = 0.5$, $\gamma_0 = 0.1$, $\omega_0\tau_0 = 1.1$, $\sigma = 0.8$, $\mu = -0.1$ and $\delta = -0.5$

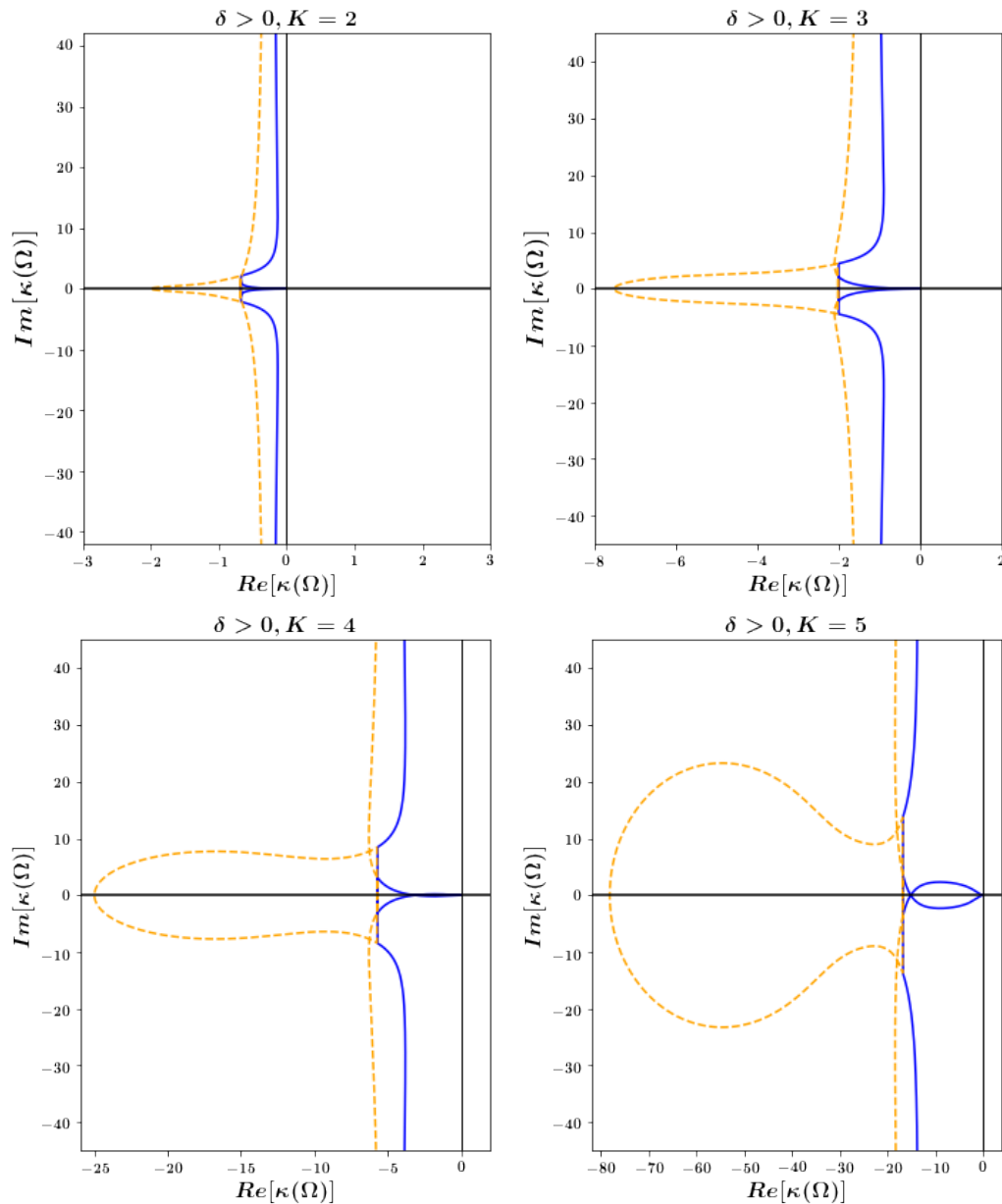


Figure 3.6: Imaginary versus real parts of κ_1 (full curve) and κ_2 (dashed curve), for $K = 2, 3, 4, 5$. Other parameter values are $I_0 = 2.5$, $\nu = 0.5$, $\gamma_0 = 0.1$, $\omega_0\tau_0 = 1.1$, $\sigma = 0.8$, $\mu = 0.1$ and $\delta = 0.5$.

figure 3.6 ($\delta > 0$), suggested that the continuous-wave will be always stable for all the values of K . This means that the inscription processes is optimum and the desire size of characters is possible to be engraved on amorphous silica.

3.2 Stability investigation of the continuous-wave laser inscription on amorphous silica glass in the presence of plasma generated: effect of radiative recombination

To follow the objective of our work, we introduced an addition physical quantity in the above equation (3.2) and obtain equation (3.49). Remark that this equation (3.49) differs from previous ones. Indeed equation (3.49) takes into consideration all together the contributions from avalanche impact ionization (first term), multiphoton ionization (second term) and electron-hole radiative recombination (last term). The model that we will be using for our study in this section is given by the couple equations (3.48)-(3.49).

$$i\frac{\partial u}{\partial z} - \delta\frac{\partial^2 u}{\partial t^2} + \sigma|u|^2u = -i\gamma_0(1 - i\omega_0\tau_0)\rho u - i\mu|u|^{2K-2}u \quad (3.48)$$

$$\frac{\partial \rho}{\partial t} = \nu|u|^2\rho + \alpha|u|^{2K} - a\rho^2 \quad (3.49)$$

3.2.1 Steady states solutions

In this second part of our investigation, we shall be looked at the effect of radiative recombination processes on the stability properties of the cw laser field. Being two nonlinear equations, general solutions to the coupled set equation (3.48)-(3.49) are nonlinear waves. Nevertheless provided specific conditions, linear solutions including harmonic waves and continuous-wave can also exist for the same set. Thus steady-state continuous-wave solutions to equation (3.48)-(3.49) can be expressed

$$u(z) = \sqrt{I_p} \exp(iP_c z), \quad \rho = \rho_0 \quad (3.50)$$

Substituting these into the coupled set (3.48)-(3.49) reads:

$$-P_c\sqrt{I_p} + \sigma I_p\sqrt{I_p} = -\gamma_0(1 - i\omega_0\tau_0)\rho_0\sqrt{I_0} - i\mu I_p^{K-1}\sqrt{I_p} \quad (3.51)$$

$$0 = \nu I_p\rho_0 + \alpha I_p^K - a\rho_0^2 \quad (3.52)$$

Equations (3.51) and (3.52) can be simplify as:

$$-P_c + \sigma I_p = -\gamma_0(1 - i\omega_0\tau_0)\rho_0 - i\mu I_p^{K-1} \quad (3.53)$$

$$0 = \nu I_p\rho_0 + \alpha I_p^K - a\rho_0^2 \quad (3.54)$$

Rearranged equations (3.53) and (3.54) yields:

$$(-P_c + \sigma I_p + \gamma_0\omega_0\tau_0\rho_0) + i(\gamma_0\rho_0 + \mu I_p^{K-1}) = 0 \quad (3.55)$$

$$\rho_0^2 - \frac{\nu I_p}{a}\rho_0 - \frac{\alpha}{a}I_p^K = 0 \quad (3.56)$$

Equation (3.56) is a quadratic equation which is easy to solve. Indeed computing the discriminant of equation (3.56) reads:

$$\Delta = \frac{\nu^2 I_p^2}{a^2} \left(1 + \frac{4a\alpha}{\nu^2} I_p^{K-2} \right) \quad (3.57)$$

Using Δ , it follows that the solution of equation (3.56) that we considered is:

$$\rho_0 = \frac{\nu I_p}{2a} \left(1 - \sqrt{1 + \frac{4a\alpha}{\nu^2} I_p^{K-2}} \right) \quad (3.58)$$

Introducing equation (3.58) into equation (3.55) yields:

$$\left[-P_c + \sigma I_p + \gamma_0\omega_0\tau_0 \frac{\nu I_p}{2a} \left(1 - \sqrt{1 + \frac{4a\alpha}{\nu^2} I_p^{K-2}} \right) \right] + i \left[\gamma_0 \frac{\nu I_p}{2a} \left(1 - \sqrt{1 + \frac{4a\alpha}{\nu^2} I_p^{K-2}} \right) + \mu I_p^{K-1} \right] = 0 \quad (3.59)$$

Equation (3.59) is a complex equation and it is equal to zero if both the real part and the imaginary part is zero. Thus it follows from this that equation (3.59) gives rise to:

$$P_c = \sigma I_p + \gamma_0\omega_0\tau_0 \frac{\nu I_p}{2a} \left(1 - \sqrt{1 + \frac{4a\alpha}{\nu^2} I_p^{K-2}} \right) \quad (3.60)$$

$$\gamma_0 \frac{\nu I_p}{2a} \left(1 - \sqrt{1 + \frac{4a\alpha}{\nu^2} I_p^{K-2}} \right) + \mu I_p^{K-1} = 0 \quad (3.61)$$

As we did in the first part of this chapter, meaning that at the steady state the propagation equations (3.48) and (3.49) correspond to a laser field and plasma density with time and space independent amplitudes. Thus:

$$\frac{\partial u}{\partial z} \Big|_{u=u_0} = 0 \quad \text{and} \quad \frac{\partial u}{\partial t} \Big|_{u=u_0} = 0 \quad (3.62)$$

Taking these two condition into equations (3.48) and (3.49) reads:

$$\sigma|u_0|^2 u_0 = -i\gamma_0 (1 - i\omega_0\tau_0) \rho_0 u_0 - i\mu|u_0|^{2K-2} u_0 \quad (3.63)$$

$$0 = \nu|u_0|^2 \rho_0 + \alpha|u_0|^{2K} - a\rho_0^2 \quad (3.64)$$

The solution of equation (3.64) is given by:

$$\rho_0 = \frac{\nu|u_0|^2 - \sqrt{\nu^2|u_0|^4 + 4a\alpha|u_0|^{2K}}}{2a} \quad (3.65)$$

Defined $I_p = |u_0|^2$, $I_p^2 = |u_0|^4$, $I_p^K = |u_0|^{2K}$ and $I_p^{K-1} = |u_0|^{2K-2}$ then formula (3.65) becomes:

$$\rho_0 = \frac{\nu I_p}{2a} \left(1 - \sqrt{1 + \frac{4a\alpha}{\nu^2} I_p^{K-2}} \right) \quad (3.66)$$

Equation (3.63) can be simplify as:

$$\sigma I_p = -i\gamma_0 (1 - i\omega_0\tau_0) \rho_0 - i\mu I_p^{K-1} \quad (3.67)$$

Substituting equation formula (3.66) into equation (3.67) yields:

$$\left[\sigma I_p + \omega_0\tau_0\gamma_0 \frac{\nu I_p}{2a} \left(1 - \sqrt{1 + \frac{4a\alpha}{\nu^2} I_p^{K-2}} \right) \right] + i \left[\gamma_0 \frac{\nu I_p}{2a} \left(1 - \sqrt{1 + \frac{4a\alpha}{\nu^2} I_p^{K-2}} \right) + \mu I_p^{K-1} \right] = 0 \quad (3.68)$$

Separating real part from the imaginary part in equation (3.68) reads:

$$\sigma I_p + \omega_0\tau_0\gamma_0 \frac{\nu I_p}{2a} \left(1 - \sqrt{1 + \frac{4a\alpha}{\nu^2} I_p^{K-2}} \right) = 0 \quad (3.69)$$

$$\gamma_0 \frac{\nu I_p}{2a} \left(1 - \sqrt{1 + \frac{4a\alpha}{\nu^2} I_p^{K-2}} \right) + \mu I_p^{K-1} = 0 \quad (3.70)$$

From equation (3.70) we derived:

$$\gamma_0 \frac{\nu I_p}{2a} \left(1 - \sqrt{1 + \frac{4a\alpha}{\nu^2} I_p^{K-2}} \right) = -\mu I_p^{K-1} \quad (3.71)$$

Replacing equation (3.71) into equation (3.69) yields:

$$\sigma I_p - \mu\omega_0\tau_0 I_p^{K-1} = 0 \quad (3.72)$$

$$\implies \mu\omega_0\tau_0 I_p^{K-1} = \sigma \quad (3.73)$$

$$\implies I_p^{K-2} = \frac{\sigma}{\mu\omega_0\tau_0} \quad (3.74)$$

$$\implies I_p = \left(\frac{\sigma}{\mu\omega_0\tau_0} \right)^{\frac{1}{K-2}} \quad (3.75)$$

As a summary, at the steady state in the presence of electron-hole radiative recombination, we have:

$$P_c = \sigma I_p + \gamma \omega_0 \tau_0 \rho_0, \quad (3.76)$$

$$I_p = \left(\frac{\sigma}{\mu \omega_0 \tau_0} \right)^{\frac{1}{K-2}}, \quad (3.77)$$

$$\rho_0 = \frac{\nu}{2a} I_p \left[1 - \sqrt{1 + \frac{4a\alpha\sigma}{\nu^2 \mu \omega_0 \tau_0}} \right], \quad (3.78)$$

Here P_c , the cw wavenumber, is fixed by the input power $I_p = |u_0|^2$ as well as the equilibrium value ρ_0 of the electron plasma density ρ . Given that these two last quantities (i.e. I_p and ρ_0) depend on characteristic parameters of the model, they cannot be arbitrary and hence can be tuned by varying characteristic parameters of the model.

3.2.2 Laser fluence

Let us now computing the **laser fluence** that require the laser to be stable at steady state. In general, this physical quantity can be calculated using the input power at the steady state [2]. Therefore utilizing the expression of cw laser input power given in formula (3.77), we obtain:

$$F_1(z) = (1 - R) F'_0 e^{-\beta_n z}, \quad (3.79)$$

with, β_n the absorption coefficient of the material, R the small laser reflectivity on the material surface, z is the local coordinate perpendicular to the surface of the sample and F'_0 is the maximum laser fluence at the surface of the specimen which can be computed as:

$$F'_0 = \frac{I_p}{S'_0} T_0 = \left(\frac{\sigma}{\mu \omega_0 \tau_0} \right)^{\frac{1}{K-2}} T_0 \quad (3.80)$$

where I_p is the above input power, T_0 is the time interval over which the continuous wave laser interacts with the material and $S'_0 = 1 \text{ cm}^2$ is the area where the laser radiation is focusing. Introducing equation (3.80) into (3.79) we obtain the continuous wave laser fluence at the steady state as:

$$F_1(z) = (1 - R) \left(\frac{\sigma}{\mu \omega_0 \tau_0} \right)^{\frac{1}{K-2}} T_0 e^{-\beta_n z}. \quad (3.81)$$

3.2.3 Benjamin-Feir instability analysis of a continuous-wave

Let us now examine the stability of the above continuous-wave regime. To this aim, we carry out a modulational-instability analysis of an input field u_0 co-propagating with a continuous-

wave signal. In this purpose we consider a small perturbation $f(z,t)$ to the cw $\sqrt{I_p}$, and $\delta\rho(t)$ a small deviation of plasma density from the steady-state, such that solutions to equation (3.48) and (3.49) can now read:

$$u(z,t) = [u_0 + f(z,t)] \exp(iP_c z) \quad (3.82)$$

$$\rho(t) = \rho_0 + \delta\rho(t) \quad (3.83)$$

Replacing the above solutions in equations (3.48) and (3.49) and linearizing around u_0 , we find:

$$i \frac{\partial f}{\partial z} - \delta \frac{\partial^2 f}{\partial t^2} + (f + f^*) C_K^{(1)} + i\gamma_0(1 - i\omega_0\tau_0)u_0\delta\rho(t) = 0, \quad (3.84)$$

$$\frac{\partial \delta\rho(t)}{\partial t} - q_0\delta\rho(t) = (f + f^*) C_K^{(2)}, \quad (3.85)$$

where,

$$C_K^{(1)} = \sigma u_0^2 + i\mu(K-1)u_0^{2K-2}, \quad C_K^{(2)} = \frac{1}{\gamma_0}(\alpha\gamma_0 K - \mu\nu)u_0^{2K-1}, \quad (3.86)$$

and $q_0 = \nu u_0^2 + \frac{2a\mu}{\gamma_0} u_0^{2K-2}$.

f^* denotes the complex conjugate of f in the linear equation (3.84). Because of the present of f^* in equation (3.84), we must consider its complex conjugate yielding:

$$-i \frac{\partial f^*}{\partial z} - \delta \frac{\partial^2 f^*}{\partial t^2} + (f^* + f) C_K^{(1)*} - i\gamma_0(1 + i\omega_0\tau_0)u_0\delta\rho(t) = 0. \quad (3.87)$$

With this consideration, as a solution of equations (3.84) and (3.87), we write formally $f(z,t) = A_1 \exp(\kappa z + i\Omega t)$ and $f^*(z,t) = A_2 \exp(\kappa z + i\Omega t)$, with κ the spatial amplification factor of the perturbation and Ω the associate time-modulation frequency. The first-order inhomogeneous linear equation (3.85) can be solved by means of Green's function technique, yielding:

$$\delta\rho = C_K^{(2)} \int_{-\infty}^t (f + f^*) e^{-q_0(t'-t)} dt' \quad (3.88)$$

$$= \frac{(A_1 + A_2) C_K^{(2)}}{i\Omega - \nu u_0^2 - \frac{2a\mu}{\gamma_0} u_0^{2K-2}} \exp(\kappa z + i\Omega t). \quad (3.89)$$

By taking equation (3.89) into equations (3.84) and (3.87), we obtain the following eigenvalue problem:

$$\kappa \begin{pmatrix} A_1 \\ A_2 \end{pmatrix} = \left[\begin{pmatrix} M_1 & M_2 \\ M_2^* & M_1^* \end{pmatrix} - S_0 \begin{pmatrix} 1 & 1 \\ 1 & 1 \end{pmatrix} \right] \begin{pmatrix} A_1 \\ A_2 \end{pmatrix} - T_0 \begin{pmatrix} N_1 & N_1 \\ N_1^* & N_1^* \end{pmatrix} \begin{pmatrix} A_1 \\ A_2 \end{pmatrix} \quad (3.90)$$

where,

$$M_1 = i(\delta\Omega^2 + \sigma u_0^2), \quad M_2 = i\sigma u_0^2, \quad (3.91)$$

$$S_0 = \mu(K - 1)u_0^{2K-2}, \quad N_1 = 1 - i\omega_0\tau_0 \quad (3.92)$$

$$T_0 = \frac{(K\alpha\gamma_0 - \mu\nu)u_0^{2K}}{i\Omega - \nu u_0^2 - \frac{2a\mu}{\gamma_0}u_0^{2K-2}} \quad (3.93)$$

The determinant of the above matrix equation gives rise to a quadratic polynomial in the eigenvalue κ , the two possible roots of which are the dispersion relations:

$$\kappa_{1,2} = -\mu(K - 1)u_0^{2K-2} \left[1 + \frac{\gamma_0(K\alpha\gamma_0 - \mu\nu)u_0^2}{\mu(K-1)(i\Omega\gamma_0 - \nu u_0^2\gamma_0 - 2a\mu u_0^{2K-2})} \right] \pm \sqrt{(S_0 + T_0)^2 - (\delta\Omega^2 + \sigma u_0^2)^2 + \sigma^2 u_0^4 - 2T_0\delta\Omega^2\omega_0\tau_0} \quad (3.94)$$

where the subscripts 1,2 refer to the plus (+) and minus (-) sign solutions respectively. More explicitly the two solutions formula (3.94) represent two possible amplification factors for the field during the cavity round-trips z , for the same modulation frequency Ω . In general these two solutions will lead to the following stability properties:

- ☞ When the real part of κ is zero, continuous wave fields will be always stable irrespective of the sign of its imaginary part,
- ☞ When the real part of κ is negative, continuous wave fields will be asymptotically stable (i.e. they are stabilized after some roundtrips) irrespective of the sign of its imaginary part,
- ☞ When the real part of κ is positive, continuous wave fields will be always unstable.

Given that the two eigenvalues are functions of the modulation frequency Ω , we find it more appropriate to first consider the cw stability at zero modulation frequency. In this later case the eigenvalues are:

$$\begin{aligned}\kappa_1 &= 0, \\ \kappa_2 &= -2\mu(K-1)u_0^{2K-2} + \frac{2\gamma_0(K\alpha\gamma_0 - \mu\nu)u_0^{2K}}{\nu u_0^2\gamma_0 + 2a\mu u_0^{2K-2}}\end{aligned}\quad (3.95)$$

It turns out that laser self-starting (i.e. cw instability) will be favored provided $\kappa_2 > 0$, or in terms of formula (3.95);

$$a < \frac{K\gamma(\alpha\gamma_0 - \mu\nu)}{2\mu^2(K-1)I_p^{K-2}}\quad (3.96)$$

Quantitatively, this condition implies two possible characteristic values of the radiative recombination coefficient a above which laser self-starting can occur: One is negative for $\alpha\gamma_0 < \mu\nu$ and hence is nonphysical, whereas the positive and physical one is conditioned by $\alpha\gamma_0 > \mu\nu$ and is:

$$a_{th} = \frac{K\gamma_0(\alpha\gamma_0 - \mu\nu)}{2\mu^2(K-1)I_p^{K-2}}.\quad (3.97)$$

In concrete terms the quantity a_{th} sets a threshold value of the electron-ion radiative recombination coefficient, above which the laser will self-start.

Due to the strong dependence of $\kappa_{1,2}$ in equation 3.94 on the modulation frequency, discussing cw stability from the analytical expressions of $\kappa_{1,2}$ for arbitrary nonzero values of Ω is far from being an easy task. Therefore we resort to a global analysis, by mapping the two eigenvalues onto a plane $Re(\kappa) - Im(\kappa)$ describing a two-dimensional complex parameter space, where $Re(\kappa)$ and $Im(\kappa)$ are real and imaginary parts respectively of the eigenvalue κ . In this parametric representation, the modulation frequency Ω plays the role of a parameter and so can span a broad range of values, which in our case will be the finite interval $-5 \leq \Omega \leq 5$.

The first figures that we considered are parametric representations of $Im(\kappa)$ as a function of $Re(\kappa)$, for some selected combinations of values of key characteristic parameters of the model. To be more explicit, the four graphs in figures 3.7 and 3.8 represent $Im(\kappa)$ as a function of $Re(\kappa)$, for $K = 2, 3, 4$ and 5 . Values of model parameters are given in the captions, and different curves in each graph correspond to different values of the radiative recombination coefficient a . Recall that the sign of δ determines the dispersion regime indeed a positive δ

3.2. STABILITY INVESTIGATION OF THE CONTINUOUS-WAVE LASER INSCRIPTION ON AMORPHOUS SILICA GLASS IN THE PRESENCE OF PLASMA GENERATED: EFFECT OF RADIATIVE RECOMBINATION

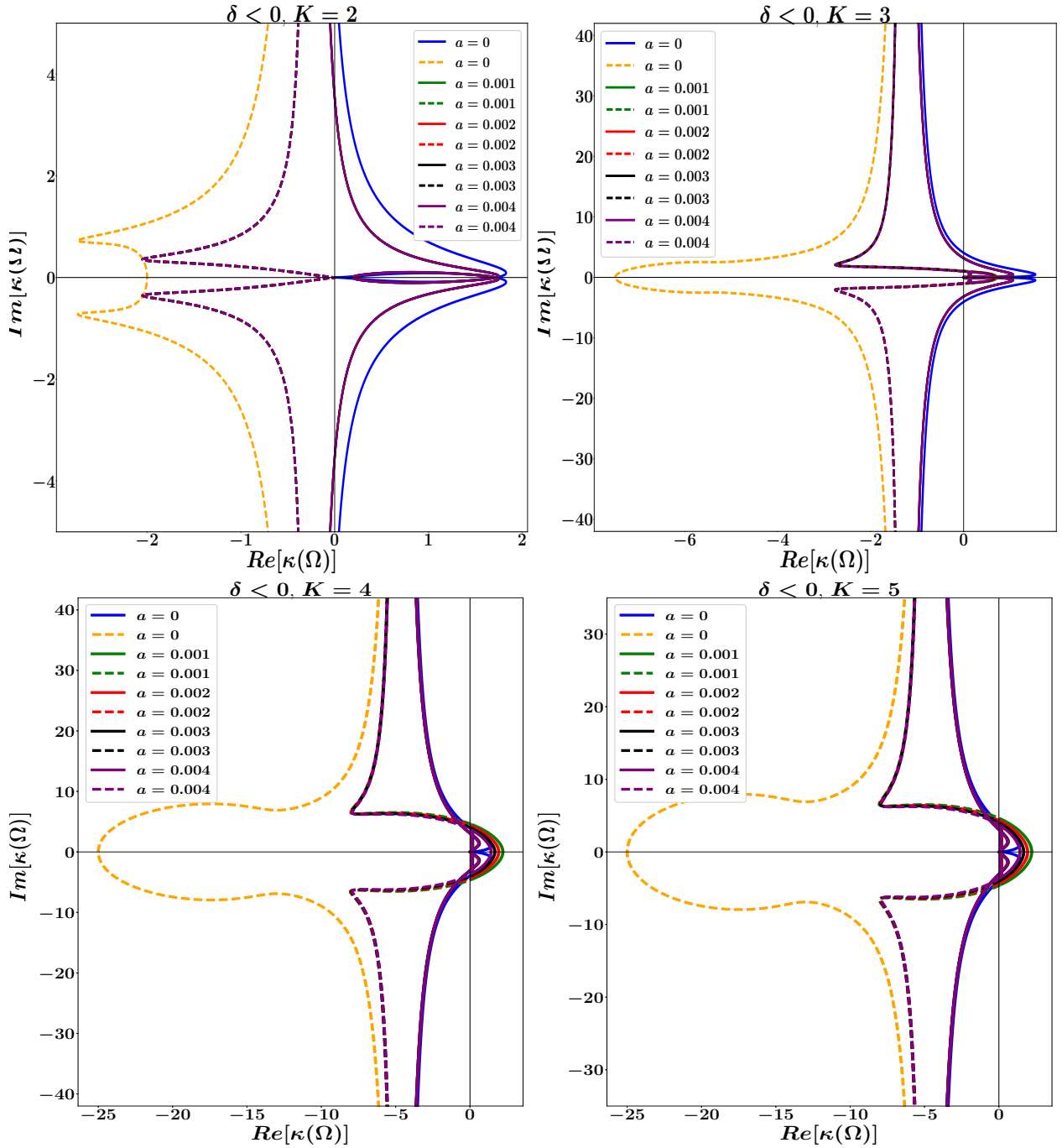


Figure 3.7: Imaginary versus real parts of κ_1 (full curve) and κ_2 (dashed curve) for $K = 2, 3, 4, 5$. The radiative recombination coefficient a is varied as $a = 0, 0.001, 0.002, 0.003, 0.004$. $\alpha = 0.6, \nu = 0.5, \mu = 0.1, I_p = 2.5, \omega_0\tau_0 = 0.2, \sigma = 0.8, \delta = -0.5, \gamma_0 = 0.1$.

3.2. STABILITY INVESTIGATION OF THE CONTINUOUS-WAVE LASER INSCRIPTION ON AMORPHOUS SILICA GLASS IN THE PRESENCE OF PLASMA GENERATED: EFFECT OF RADIATIVE RECOMBINATION

corresponds to a normal group-velocity dispersion, whereas a negative δ will correspond to an anomalous group-velocity dispersion well known to favor the generation of pulse structures, of course provided the intrinsic refractive index of the amorphous silica is of a self-focusing Kerr nonlinearity. Figure 3.7 suggests that small values of photon number K are expected

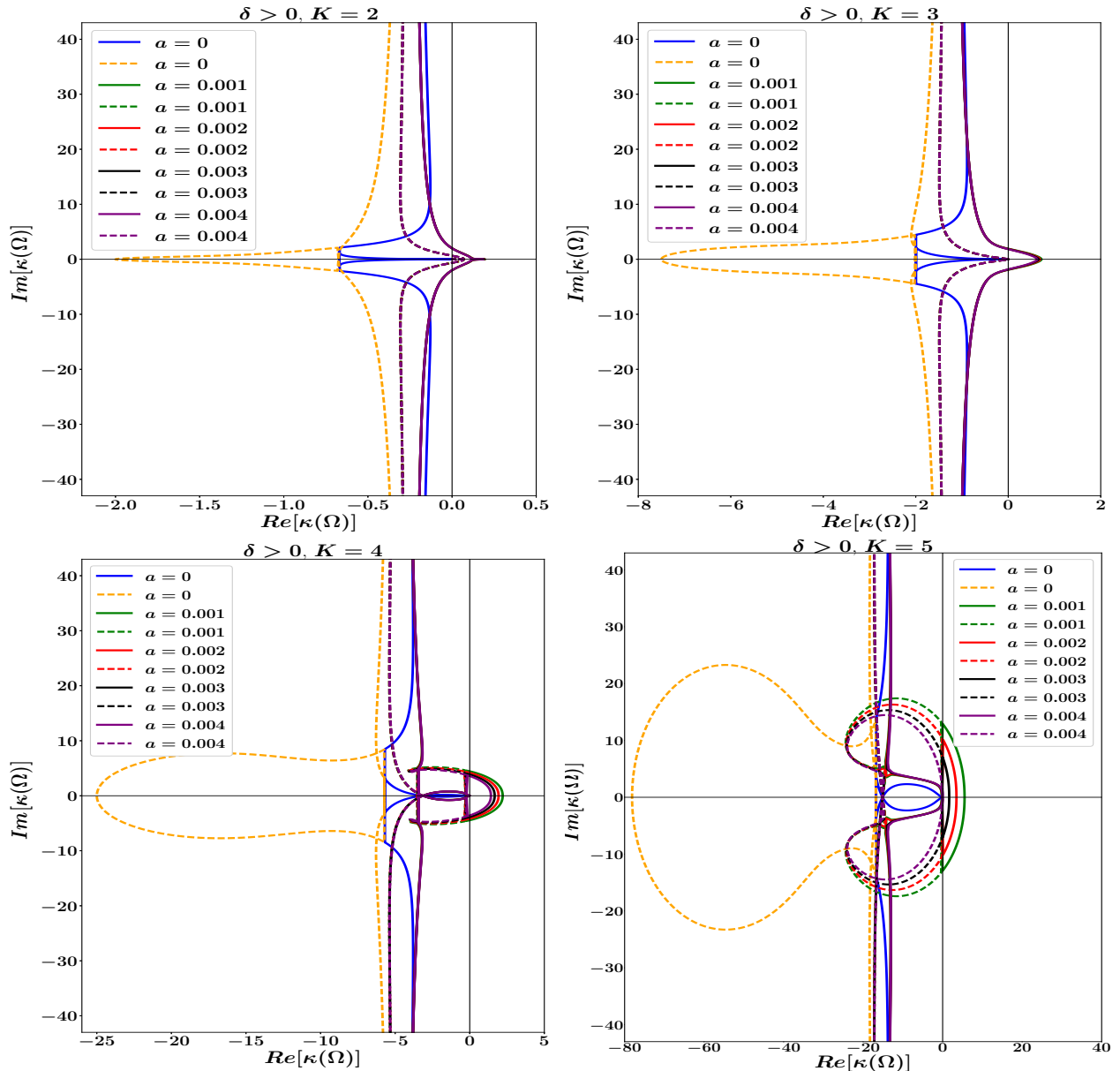


Figure 3.8: Imaginary versus real parts of κ_1 (full curve) and κ_2 (dashed curve) for $K = 2, 3, 4, 5$. The radiative recombination coefficient a is varied as $a = 0, 0.001, 0.002, 0.003, 0.004$. $\alpha = 0.6, \nu = 0.5, \mu = 0.1, I_p = 2.5, \omega_0\tau_0 = 0.2, \sigma = 0.8, \delta = 0.5, \gamma_0 = 0.1$.

to favor laser self-starting in the anomalous dispersion regime. As K increases, the real part

of the largest eigenvalue associated to the higher values of radiative recombination coefficient gradually shifts near the negative branch but still positive and consequently, the continuous wave regime is unstable. On the contrary figure 3.8 indicates that in the normal dispersion regime, continuous wave operation will be stable for higher values of radiative recombination coefficient $\mathbf{a=0.004\ m^3\ fs^{-1}}$ as well as the multi-photon absorption rate $K = 5$.

3.2.4 Summary

At zero modulation frequency of the perturbation parameter, we obtained from formula (3.94) two eigenvalues which are κ_1 and κ_2 . We found that, the cw laser will be always stable for $\kappa_1 = 0$ and $\kappa_2 < 0$, meaning that for the laser operating in the continuous-wave mode, it will be possible to engrave the desire size of characters on amorphous silica. At non-zero modulation frequency for $\delta < 0$, figure 3.7 shown that the continuous wave laser will self-start. For this case engraving on amorphous silica in the continuous-wave regime is not optimal. However, for $\delta > 0$ as shown in figure 3.8, the continuous wave laser is stable for $K = 5$ suggesting an optimum condition to engrave a desire size of characters on amorphous silica. In this case the best value of radiative recombination coefficient involving in the process is $\mathbf{a=0.004\ m^3\ fs^{-1}}$.

3.3 Stability investigation of pulsed laser inscription on amorphous silica glass

In the full nonlinear regime of inscription on amorphous silica, solutions to the femtosecond laser equation (3.48) are high-intensity fields which can be represented as real-amplitude pulses, undergoing spatio-temporal modulations

$$u(t,z) = g(\tau) \exp i [\phi(\tau) - \omega z], \quad (3.98)$$

g and ϕ represent respectively the real laser amplitude and the modulation phase. We introduce a reduced time as $\tau = t - vz$, in where v is the pulse inverse velocity, t the physical time of the pulse propagation and ω is the nonlinear shift of the propagation constant. Letting $g(z,t) \equiv g(\tau)$, $\phi \equiv \phi(\tau)$, and using equation (3.98) to compute the different quantities appearing in

equations (3.48) and (3.49) yields:

$$\frac{\partial u}{\partial z} = (-vg' - i(v\phi' + \omega)g) \exp i(\phi(\tau) - \omega z) \quad (3.99)$$

$$\frac{\partial^2 u}{\partial t^2} = (g'' + i\phi''g + 2i\phi'g' - \phi'^2g) \exp i(\phi(\tau) - \omega z) \quad (3.100)$$

$$|u|^2 u = g^3 \exp i(\phi(\tau) - \omega z) \quad \text{and} \quad |u|^{2K-2} u = g^{2K-1} \exp i(\phi(\tau) - \omega z). \quad (3.101)$$

Inserting equations (3.99), (3.100) and (3.101) into equation (3.48) and equation (3.49) reads:

$$\begin{cases} -ivg' + (v\phi' + \omega)g - \delta(g'' + i\phi''g + 2i\phi'g' - \phi'^2g) + \sigma g^3 = -i\gamma_0(1 - i\omega_0\tau_0)\rho g - i\mu g^{2K-1} \\ \rho' - \nu g^2\rho - \alpha g^{2K} + a\rho^2 = 0 \end{cases} \quad (3.102)$$

The system of equation (3.102) can be putting in the form:

$$\begin{cases} [(vM + \omega + \delta M^2 + \gamma_0\omega_0\tau_0\rho)g - \delta y' + \sigma g^3] + i[(\delta M' - \gamma_0\rho)g + (v + 2\delta M)y - \mu g^{2K-1}] = 0 \\ \rho' - \nu g^2\rho - \alpha g^{2K} + a\rho^2 = 0 \end{cases} \quad (3.103)$$

Separating real parts from the imaginary parts, we obtain the following sets of coupled first-order nonlinear ordinary differential equations:

$$(vM + \omega + \delta M^2 + \gamma_0\omega_0\tau_0\rho)g - \delta y' + \sigma g^3 = 0 \quad (3.104)$$

$$(\delta M' - \gamma_0\rho)g + (v + 2\delta M)y - \mu g^{2K-1} = 0 \quad (3.105)$$

$$\rho' - \nu g^2\rho - \alpha g^{2K} + a\rho^2 = 0, \quad (3.106)$$

where each prime denotes the derivative with respect to τ and $M = \phi'$ is the instantaneous frequency whereas $g' = y$. The parameters v and ω are eigenvalues of equations (3.104) and (3.105). Pulse solutions exist only at certain values of v and ω . Let us focus on the system dynamics in the particular case $v = 0$ i.e zero-velocity. For this value of v the set of coupled first-order nonlinear ordinary differential equations (3.104)-(3.106) reduces to:

$$\begin{cases} (\omega + \delta M^2 + \gamma_0\omega_0\tau_0\rho)g - \delta y' + \sigma g^3 = 0 \\ (\delta M' - \gamma_0\rho)g + 2\delta M y - \mu g^{2K-1} = 0 \\ \rho' - \nu g^2\rho - \alpha g^{2K} + a\rho^2 = 0 \end{cases} \quad (3.107)$$

Separating derivatives in equations (3.107) and combine the obtaining system with equation (3.106), we get:

$$\begin{cases} M' = \frac{\gamma_0 \rho}{\delta} - \frac{2My}{g} + \frac{\mu g^{2K-2}}{\delta} \\ y' = \frac{(\omega + \delta M^2 + \gamma_0 \omega_0 \tau_0 \rho)g}{\delta} + \frac{\sigma g^3}{\delta} \\ g' = y \\ \rho' = \nu g^2 \rho + \alpha g^{2K} - a \rho^2 \end{cases} \quad (3.108)$$

Our first interest will be on the singular solutions to this system of equations (3.108), which are their fixed points, with the aim to probe the effects of important characteristic parameters of the model such as the radiative recombination coefficient \mathbf{a} and the multiphoton absorption rate K , on equilibrium solutions of the laser amplitude g and instantaneous frequency M , as well as of the electron plasma density ρ .

3.3.1 Fixed-point solutions

Singular solutions to the set of first-order nonlinear ordinary differential equations (3.108), which are their fixed points are obtaining by setting $M' = 0$, $y' = 0$, $g' = 0$ and $\rho' = 0$. These fixed points, are the roots of the following nonlinear system:

$$\begin{cases} \frac{\gamma_0 \rho}{\delta} - \frac{2My}{g} + \frac{\mu g^{2K-2}}{\delta} = 0 \\ \frac{(\omega + \delta M^2 + \gamma_0 \omega_0 \tau_0 \rho)g}{\delta} + \frac{\sigma g^3}{\delta} = 0 \\ y = 0 \\ \nu g^2 \rho + \alpha g^{2K} - a \rho^2 = 0 \end{cases} \quad (3.109)$$

This system can be simplify as:

$$\gamma_0 \rho + \mu g^{2K-2} = 0 \implies \gamma_0 \rho = -\mu g^{2K-2} \quad (3.110)$$

$$\omega + \delta M^2 + \gamma_0 \omega_0 \tau_0 \rho + \sigma g^2 = 0 \quad (3.111)$$

$$\nu g^2 \rho + \alpha g^{2K} - a \rho^2 = 0 \quad (3.112)$$

Replacing equation (3.110) into equations (3.111) and (3.112) gives rise to the system:

$$\begin{cases} \omega + \delta M^2 + \sigma g^2 - \mu \omega_0 \tau_0 g^{2K-2} = 0 \\ (\alpha \gamma_0 - \mu \nu) g^{2K} - a \gamma_0 \rho^2 = 0 \end{cases} \quad (3.113)$$

From this system we derive:

$$M^2 = \frac{1}{\delta} [\mu\omega_0\tau_0g^{2K-2} - \omega - \sigma g^2] \quad (3.114)$$

$$\rho = g^K \sqrt{\left(\frac{\alpha\gamma_0 - \mu\nu}{a\gamma_0}\right)} \quad (3.115)$$

Remarkable enough, formula (3.115) suggests that irrespective of the value of K , the electron plasma density ρ will be zero when the laser amplitude g is zero.

Figure 3.9 represents the variations of the two fixed points of the laser amplitude g as a function of ω , for $K = 2, 3, 4, 5$ and values of model parameters given in the captions. It should be noted that by fixed points of g we understand its extrema, i.e. its maximum and minimum which are obtained by annihilating M in formula (3.114). According to figure 3.9, for $K = 2$ the laser dynamics is dominated by weakly nonlinear pulse trains with maximum amplitudes for $\omega = 0$. An increase of K (see graphs for $K = 3, 4$ and 5) favors strongly nonlinear pulse trains of larger amplitudes. In this case, the inscription processes will be optimized and therefore will produce a very fine characters on the material. We have also plotted the instantaneous frequency M as a function of the amplitude g of laser (figure 3.10), and the laser amplitude g as function of the electron plasma density ρ (figure 3.11), for four different values of K . Remark that the expression of M given in formula (3.114) does not contains the radiative recombination coefficient \mathbf{a} but is controlled mainly by the laser propagation constant ω , whereas g as a function of ρ extracted from equation (3.115) depends on \mathbf{a} but not on ω . Therefore, we have chosen to plot M as a function of g by considering two cases i.e., the case $\omega = 0$ and the case of finite nonzero value of ω as one sees in figure 3.10. The different curves in the graphs of figure 3.10 show that M is enhanced by an increase of g , and that there is a threshold value of the amplitude beyond which the instantaneous frequency is expected to decrease to zero. As it is apparent, this threshold value of g (and consequently of M) is decreased with an increase of K . To be more explicit, in this graphs, we observed that either $\omega = 0$ or $\omega = 0.5$, for $K = 2$, the instantaneous frequency increases linearly with the amplitude g , suggesting a single-mode laser characterized by one instantaneous frequency for a given value of the laser amplitude. However, as the photon number increases (see graphs for $K = 3, 4$ and 5), the instantaneous frequency M increases until a maximum and then starts decreasing. This non-linear behaviour of the instantaneous frequency M with an increase of K and decreases of the laser amplitude g is marked by the emergence of two amplitudes having

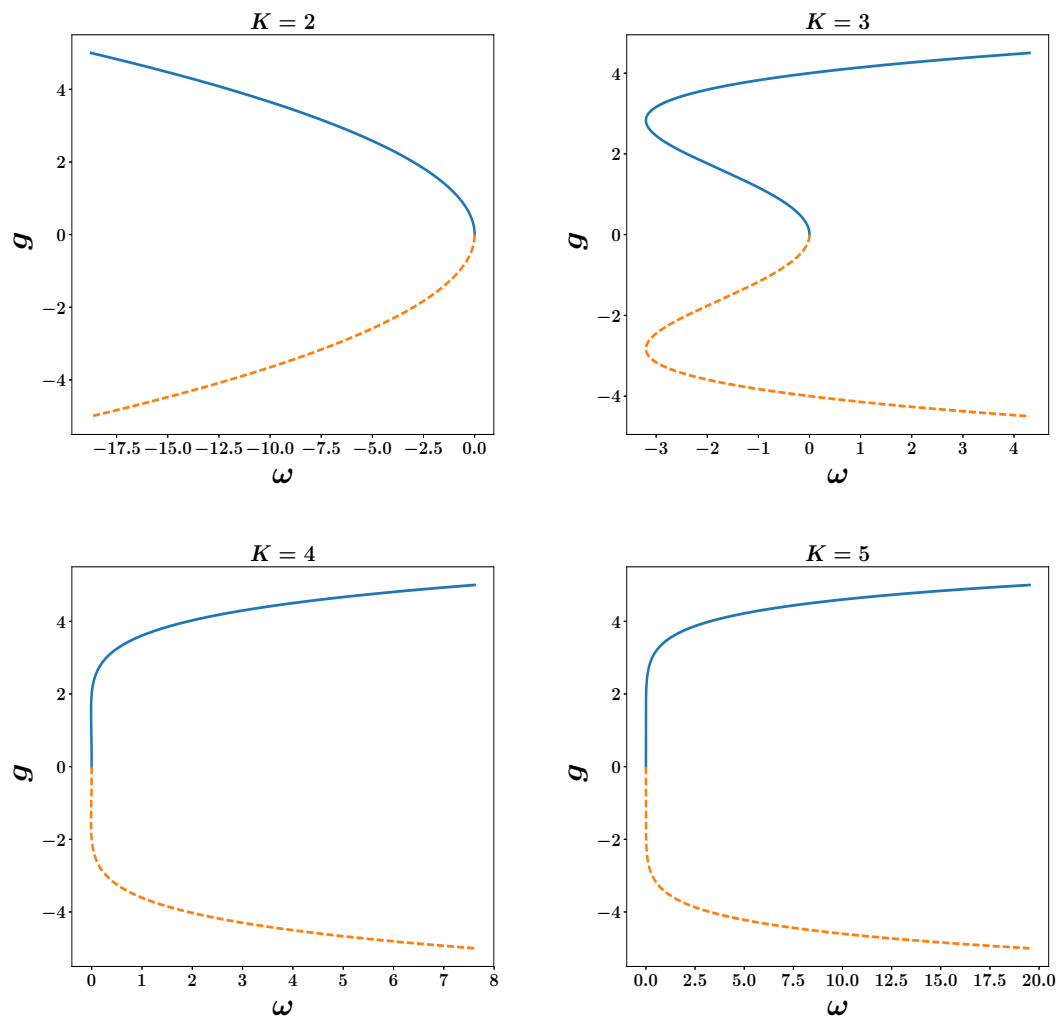


Figure 3.9: Fixed points of the laser amplitude g as a function of ω , for $K = 2, 3, 4, 5$, $\sigma = 0.8$, $\omega_0\tau_0 = 0.2$, $\mu = 0.25$.

the same frequency, thus suggesting two distinct laser modes with a common instantaneous frequency. Such behaviour indicates that, the continuous-wave laser becomes more and more unstable as a single-mode field and bifurcates into a two-mode field. This bifurcation is of a period-doubling type, and indicates that a further increase in the photon number and the decrease of the laser amplitude should lead to a regime in which the laser can no more operate as a continuous wave. Therefore, for this case it is not possible for the inscription processes to print a fine characters on amorphous silica and it will be only possible to print a very fine character on amorphous silica. In figure 3.11, the fixed point of the electron plasma density is always zero at zero amplitude of the laser whatever the value of K , consistently with what we learned from formula (3.115). However for all the values of K , as the recombination phenomena becomes more and more strong (i.e. $\mathbf{a} = 0.001, 0.002, 0.003$ and 0.004), the plasma density decrease leading to the stability of the laser amplitude. This decreasing of the plasma density will allow the inscription process to be optimized and therefore, the fine character will be possible to engrave on amorphous silica in the equilibrium state of the non-linear regime.

3.3.2 Pulses stability

Considering the full nonlinear dynamics regime of femtosecond laser inscription, the set of first-order ordinary differential equations (3.108) was solved numerically using a fourth-order Runge-Kutta algorithm. Because equations (3.48)-(3.49) involve several parameters, all of which cannot be varied in this study, we fixed most parameters except two ones i.e. the multiphoton absorption rate K , which was given the four different values $K = 2, 3, 4, 5$, and the radiative recombination coefficient \mathbf{a} which was varied in three distinct ranges of values where three distinct behaviors were noticed. Figures 3.12 and 3.13 are time variations of the laser amplitude $g(t)$ and of the electron plasma density $\rho(t)$, for four distinct values of K and values of model parameters listed in the figure captions. For these two graphs the laser frequency have been taken to be $\omega = 1.3$ rad/fs. In figures 3.14 and 3.17 we also plotted respectively $\rho(t)$ and $g(t)$ but with $\omega = 1.5$ rad/fs. Note that for each graph, we plotted dynamical quantities of the model for different values of radiative recombination coefficient \mathbf{a} starting with $\mathbf{a}=\mathbf{0}$ (i.e. when there is no radiative recombination). Our objective in so doing was to highlight the qualitative and quantitative influences of \mathbf{a} , on the system dynamics. Indeed, to show the impact of radiative recombination processes on the femtosecond laser

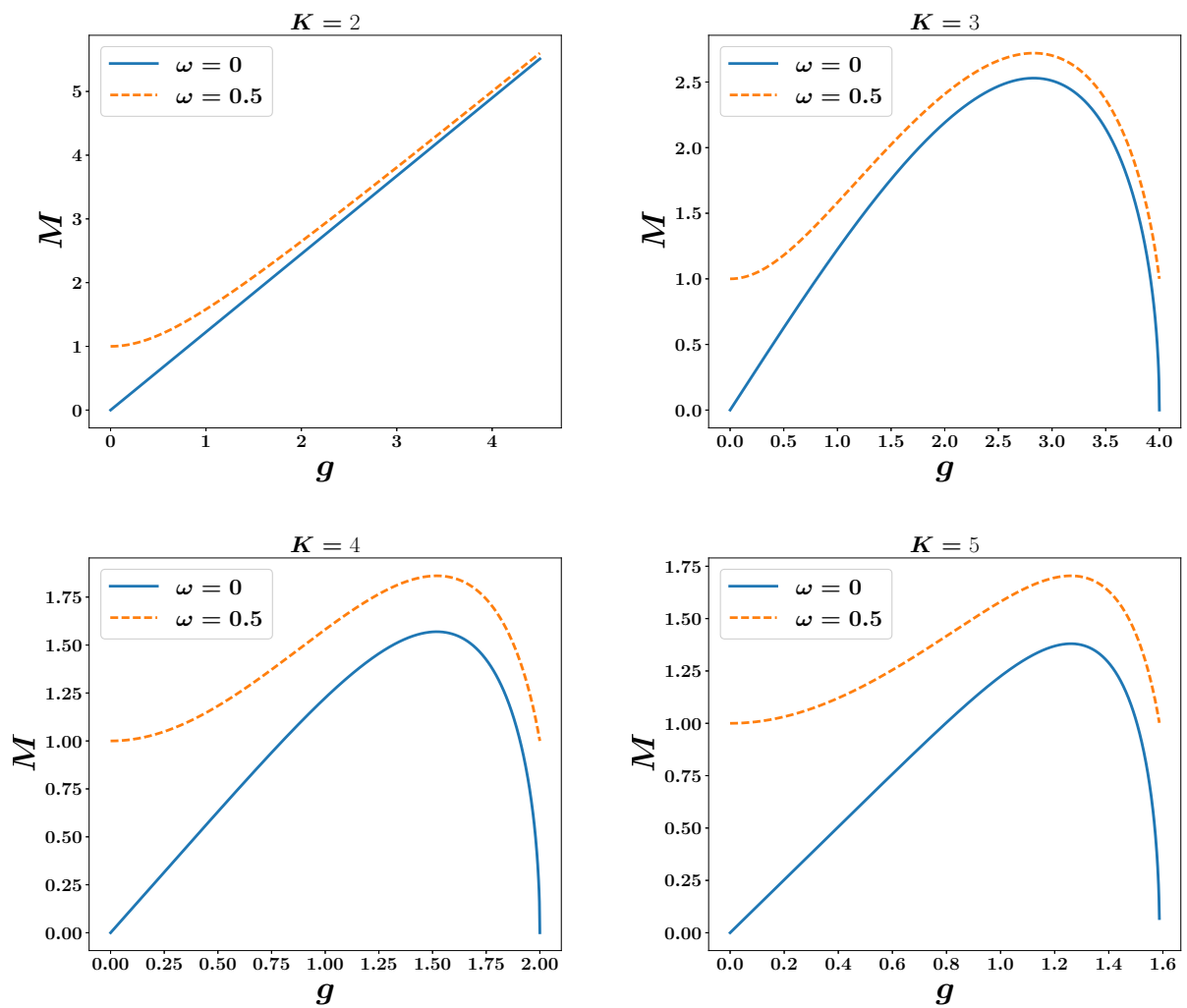


Figure 3.10: Variation of the instantaneous frequency M with the amplitude g of laser, for $K = 2, 3, 4, 5$ and two different values of ω indicated in the graphs. $\sigma = 0.8$, $\omega_0\tau_0 = 0.2$, $\mu = 0.25$, $\delta = -0.5$.

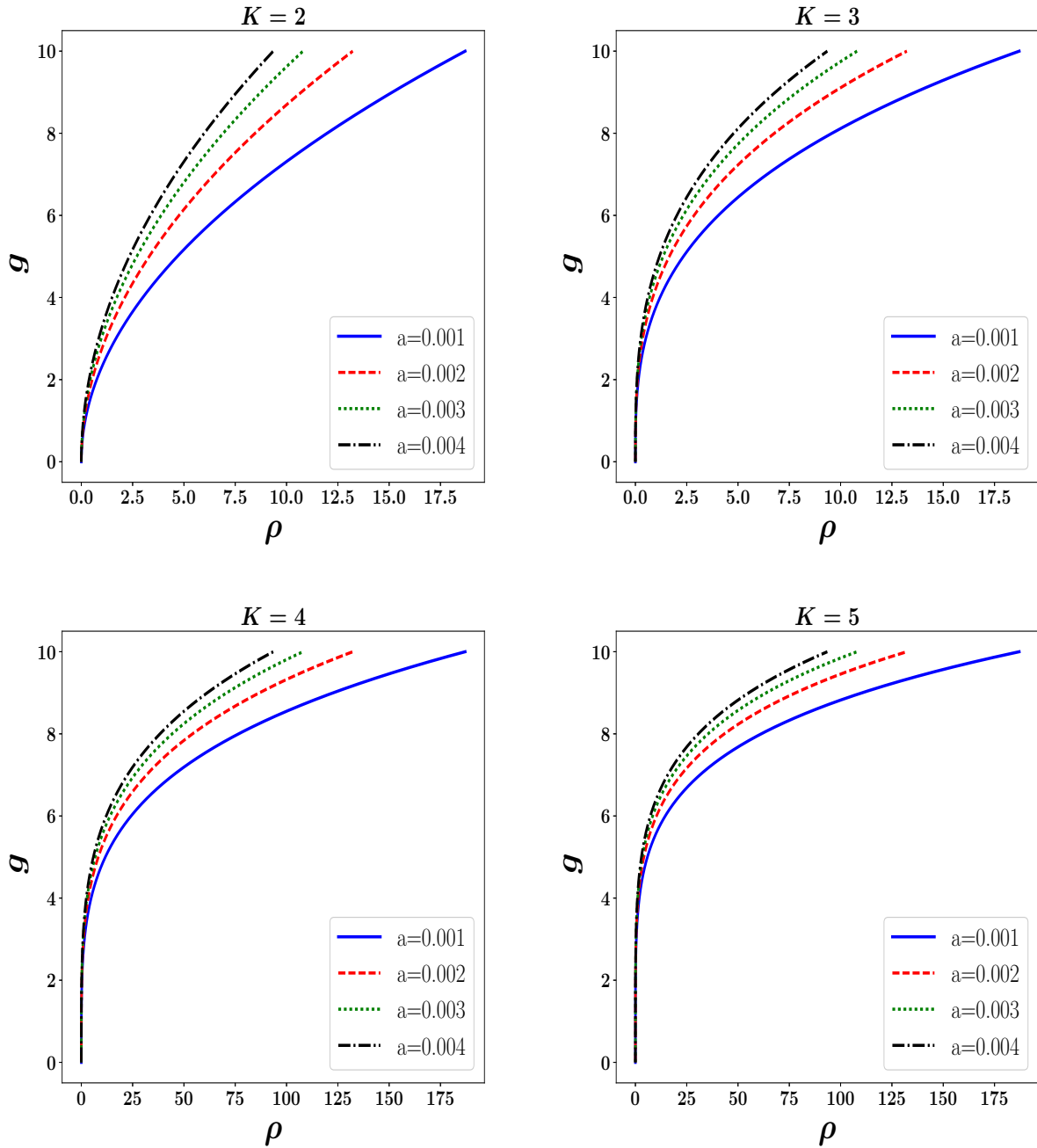


Figure 3.11: Variation of the laser amplitude g with the electron plasma density ρ , for $K = 2, 3, 4, 5$ and different values of the radiative recombination coefficient a indicated in the graphs. $\nu = 0.1, \alpha = 0.6, \gamma_0 = 0.1, \mu = 0.25$.

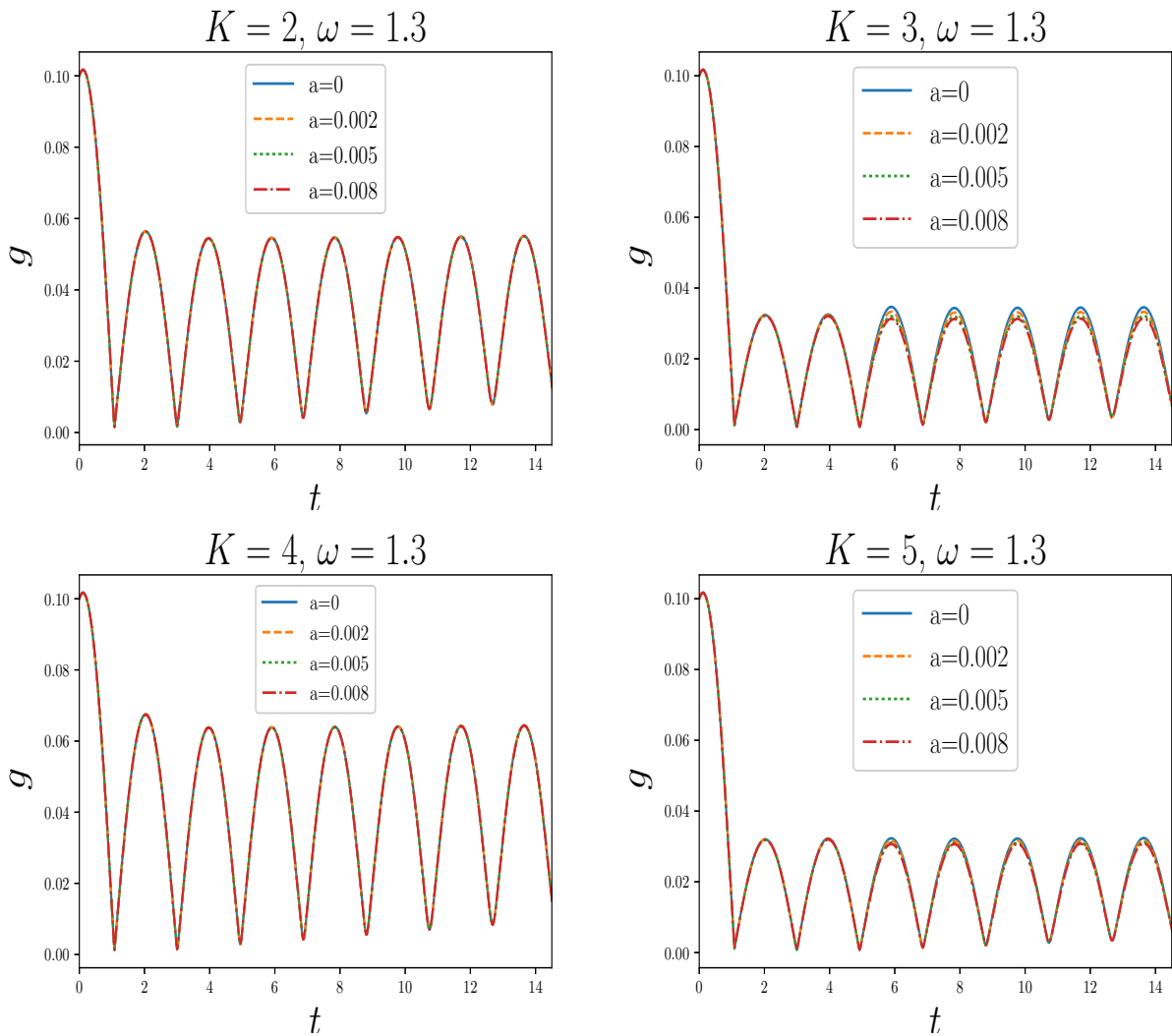


Figure 3.12: Time variation of the laser amplitude g , for $K = 2, 3, 4, 5$ and different values of the radiative recombination coefficient a indicated in the graphs. $\sigma = 0.8, \omega_0 = 1.38, \tau_0 = 0.58, \delta = -0.5, \mu = 0.5, \nu = 0.5, \gamma_0 = 0.18, \alpha = 0.6$.

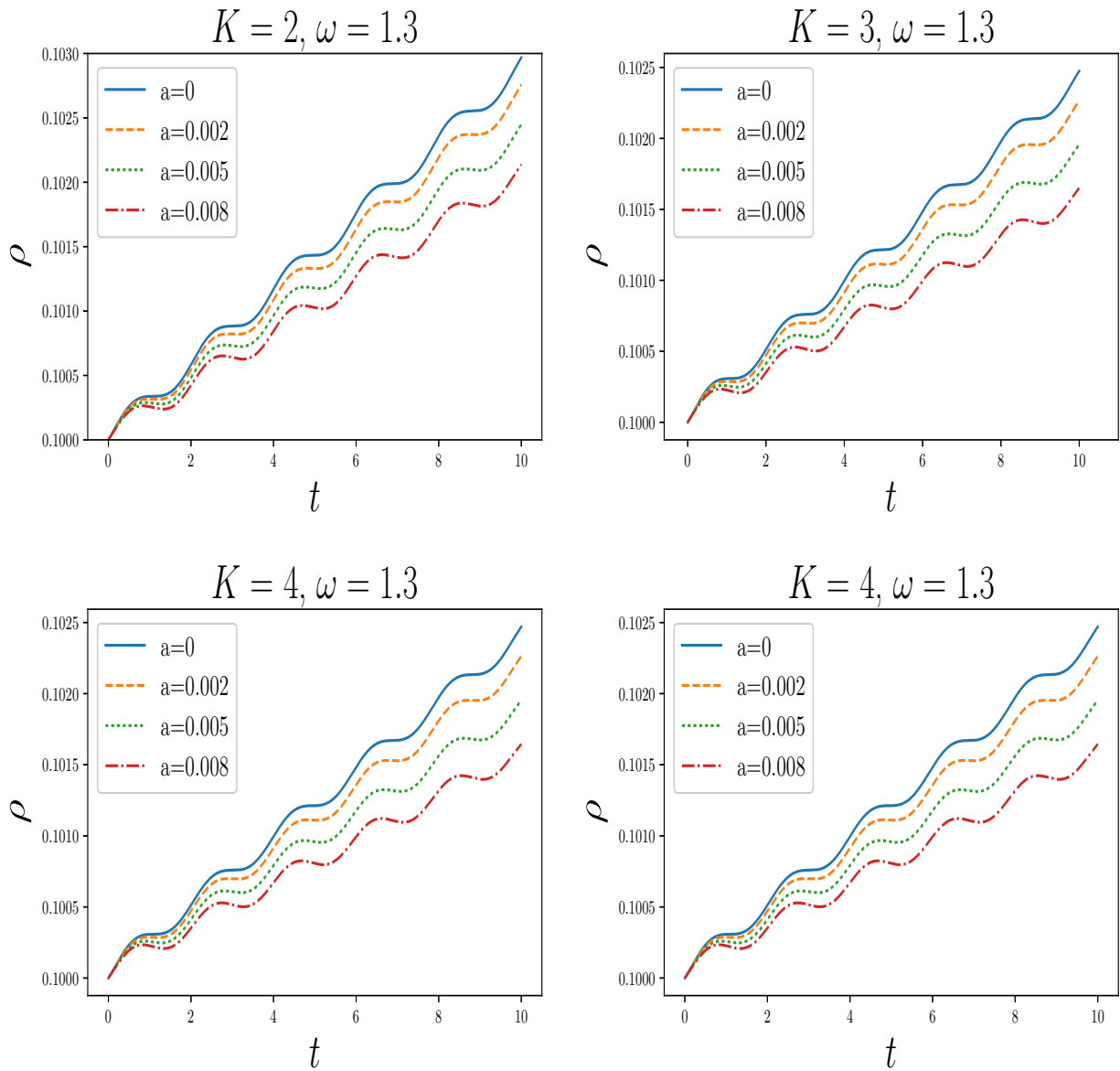


Figure 3.13: Time variation of the electron plasma density ρ , for $K = 2, 3, 4, 5$ and values of a indicated in the graphs. $\sigma = 0.8, \omega_0 = 1.38, \tau_0 = 0.58, \delta = -0.5, \mu = 0.5, \nu = 0.5, \gamma_0 = 0.18, \alpha = 0.6$.

dynamics and stability, we started our analysis by consider a small variation of the electron-hole recombination coefficient \mathbf{a} by taking $\omega = 1.3$ rad/fs. In this case, we observed that, when \mathbf{a} are varying very weakly, the laser amplitude $g(t)$ fluctuated as K increases (see figure 3.12). In addition to this, there is a fall-off of $g(t)$ with time, which is more and more pronounced as K gets larger. We attribute this fall-off to a damping effect induced by the density of electron plasma i.e. $\rho(t)$, which in this context acts like a laser loss. However, the plasma density $\rho(t)$ is always increases even when \mathbf{a} is increase (see figure 3.13). The fluctuation of the laser amplitude $g(t)$ for this case means that the range of recombination coefficient that we have selected is very weak to contribute to the stability of the pulses train in the presence of plasma generated. Therefore the pulse laser is unstable and the inscription process cannot be efficient. From these results, we derived the laser power per unit area as:

$$P(K) = \frac{|g|^2}{A_s}, \quad (3.116)$$

where A_s is the focused area and $K = 2,3,4,5$. This focused area can be calculated as:

$$A_s = \frac{\pi}{4}d_{sp}^2, \quad \text{where } d_{sp} \text{ is the beam spot diameter on the amorphous silica is given by:}$$

$$d_{sp} = 2\sqrt{\frac{A_s}{\pi}} \quad (3.117)$$

We measured the value of g from the four curves given by figure 3.12. We fixed the time over which the laser interact with amorphous silica to be $t = 10$ fs, $A_s = 0.0025\text{cm}^2$ and the laser energy per unit area (i.e. laser fluence) was computed using $F = P(K) \times t$. The results are summarizing in table 3.1.

The electron plasma density ρ (for $\omega = 1.3$ rad/ fs), plotted in figure 3.13, is increasing with time for $\mathbf{a}=0, 0.002, 0.005$ and 0.008 irrespective of the value of K and this affect the inscription process. In order to optimize this process, we have increased the laser frequency to $\omega = 1.5$ rad/fs and keep the other parameters that we used to plot ρ versus time in figure 3.13. From this we obtained the new plot of ρ as a function of time as represented in figure 3.15. We also noticed that even by increasing the value of ω , the plasma density still increase, this means that we need to find the best range of variation for the recombination parameters that will be contributed to the pulse stability. In so doing, we realized that, when \mathbf{a} is increased in a relatively large range of values, $\rho(t)$ decreases exponentially in time tending to its equilibrium

Table 3.1: Parameters for which pulses is unstable: $\omega = 1.3$ rad/fs

Laser amplitude	Power density	Laser fluence	Laser spot diameter
$K = 2, g = 0.057$	$P = 13 \times 10^{14}$ W/cm ²	$F = 13$ J/cm ²	$d_{sp} = 0.056$ cm
$K = 3, g = 0.036$	$P = 5.18 \times 10^{14}$ W/cm ²	$F = 5.18$ J/cm ²	$d_{sp} = 0.056$ cm
$K = 4, g = 0.063$	$P = 15.8 \times 10^{14}$ W/cm ²	$F = 15.8$ J/cm ²	$d_{sp} = 0.056$ cm
$K = 5, g = 0.035$	$P = 4.9 \times 10^{14}$ W/cm ²	$F = 4.9$ J/cm ²	$d_{sp} = 0.056$ cm

Amorphous Silica Glass parameters
Group velocity dispersion, $\delta = -0.5$ fs ² /cm
Kerr nonlinearity coefficient, $\sigma = 0.8$ cm W ⁻¹
Electron lifetime $\tau_0 = 0.58$ fs
Electron plasma frequency $\omega_0 = 1.38$ rad/fs
Avalanche coefficient $\nu = 0.5$ cm ² /J
Loss coefficient of the multiphoton absorption in amorphous silica, $\mu = 0.5$ cm ⁻¹
Radiative recombination coefficient (in cm ³ fs ⁻¹), $\mathbf{a} = 0, 0.002, 0.005, 0.008$

value with an increasingly sharp slope (see figure 3.14). This last behaviour of the plasma density profile takes us in the situation that, when \mathbf{a} is very small ρ is an exponentially increasing function of time and that large value of \mathbf{a} decrease the plasma density. The values of \mathbf{a} chosen for the numerical results just discussed, from figures 3.13 and 3.15 do not enable one appreciate how the electron plasma density ρ changes from its exponentially increasing feature for small values of \mathbf{a} , to an exponentially decreasing feature when \mathbf{a} is large. It is quite apparent that in the very small range of values of \mathbf{a} , ρ is periodically oscillating as it increases exponentially with time (figure 3.16). The quantity \mathbf{a}_{th} in the graphs of figure 3.15, is the characteristic value of the radiative recombination coefficient for which the exponential variation of ρ with time is suppressed. For this value of \mathbf{a} , the electron plasma density $\rho(t)$ constantly oscillates between two positive extrema. Keeping $\omega = 1.5$ rad/fs, we have plotted the laser amplitude $g(t)$ versus time in figure 3.17 for a large values of radiative recombination coefficient (i.e. for the same values of \mathbf{a} used in figure 3.14). In this case we found that, a femtosecond laser amplitude $g(t)$ is manifestly a pulse train with a maximum varying only weakly with \mathbf{a} for $K = 2$. However, as K is increased the maximum of g gets more and more large, which lead to the stability of laser pulses. It follows from this results that the

femtosecond laser powers and energies for different values of K are summarizing in table 3.2. For this case we kept $t = 10$ fs and reduced the focused area to $A'_s = 0.00002$ cm².

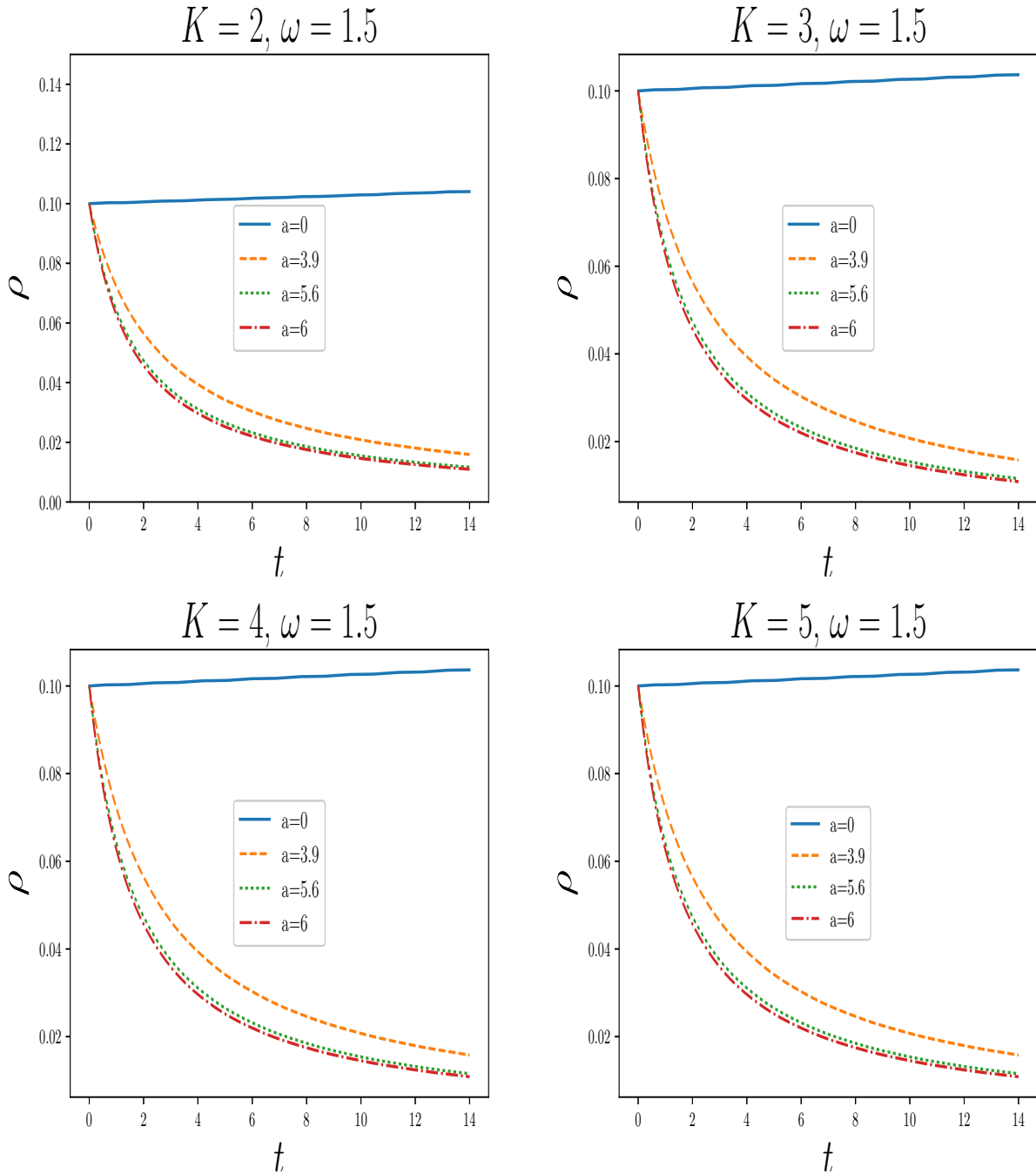


Figure 3.14: Time variation of the electron plasma density ρ , for $K = 2, 3, 4, 5$ and values of a indicated in the graphs. $\sigma = 0.8$, $\omega_0 = 1.38$, $\tau_0 = 0.58$, $\delta = -0.5$, $\mu = 0.5$, $\nu = 0.5$, $\gamma_0 = 0.18$, $\alpha = 0.6$.

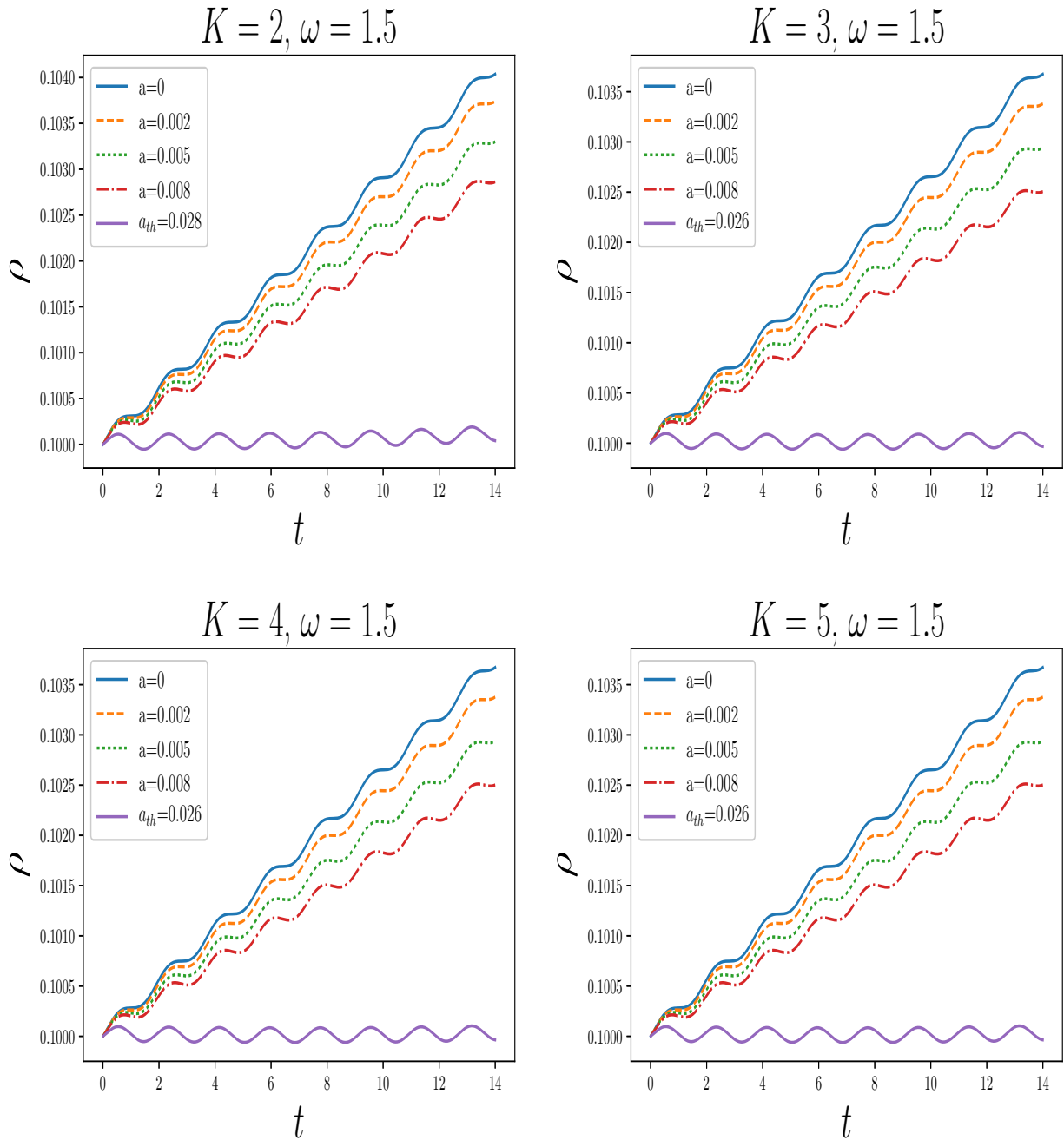


Figure 3.15: Time variation of the electron plasma density ρ , for $K = 2, 3, 4, 5$ and values of a indicated in the graphs. $\sigma = 0.8$, $\omega_0 = 1.38$, $\tau_0 = 0.58$, $\delta = -0.5$, $\mu = 0.5$, $\nu = 0.5$, $\gamma_0 = 0.18$, $\alpha = 0.6$.

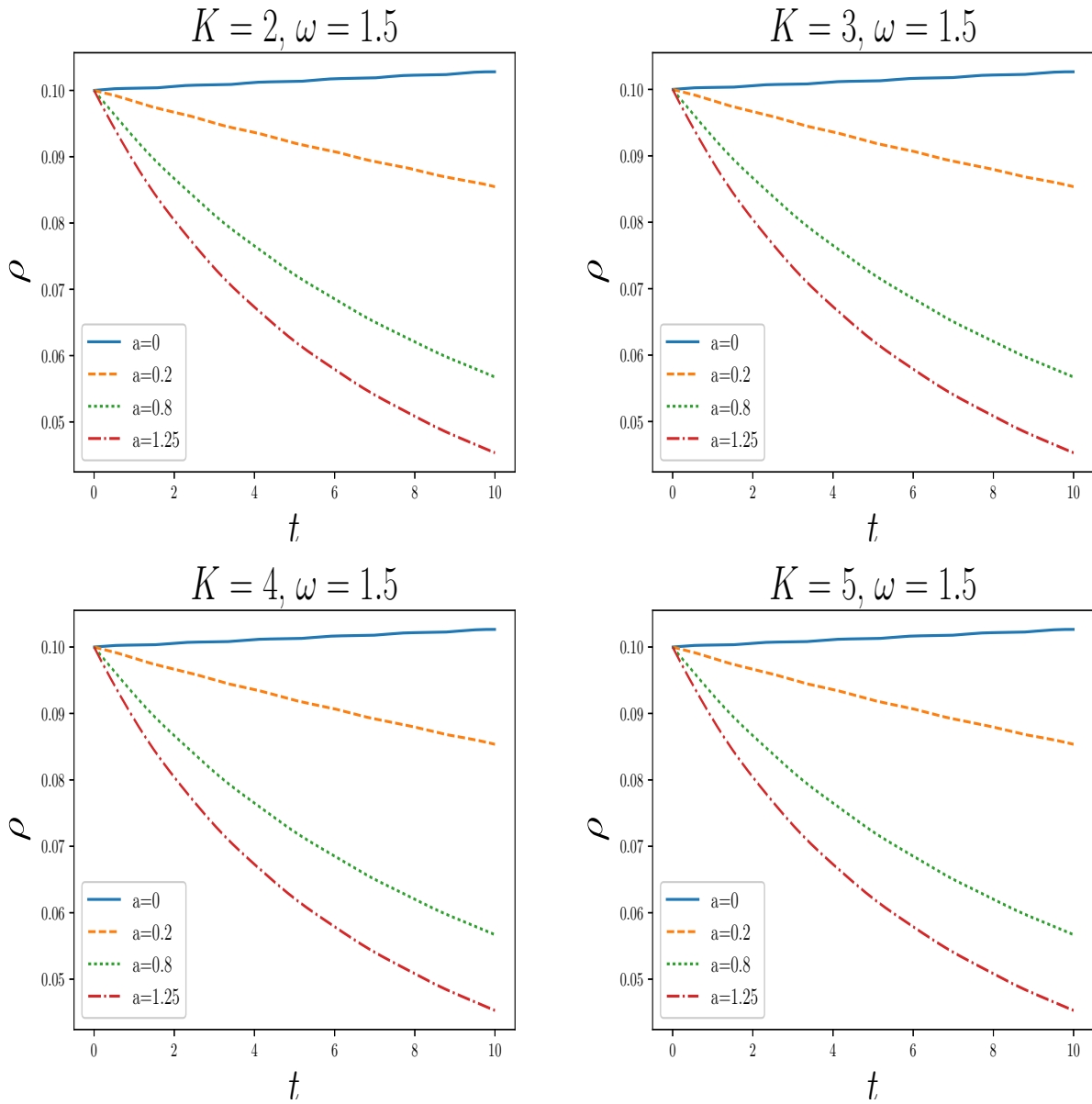


Figure 3.16: Time variation of the electron plasma density ρ , for $K = 2, 3, 4, 5$ and values of a indicated in the graphs. $\sigma = 0.8$, $\omega_0 = 1.38$, $\tau_0 = 0.58$, $\delta = -0.5$, $\mu = 0.5$, $\nu = 0.5$, $\gamma_0 = 0.18$, $\alpha = 0.6$.

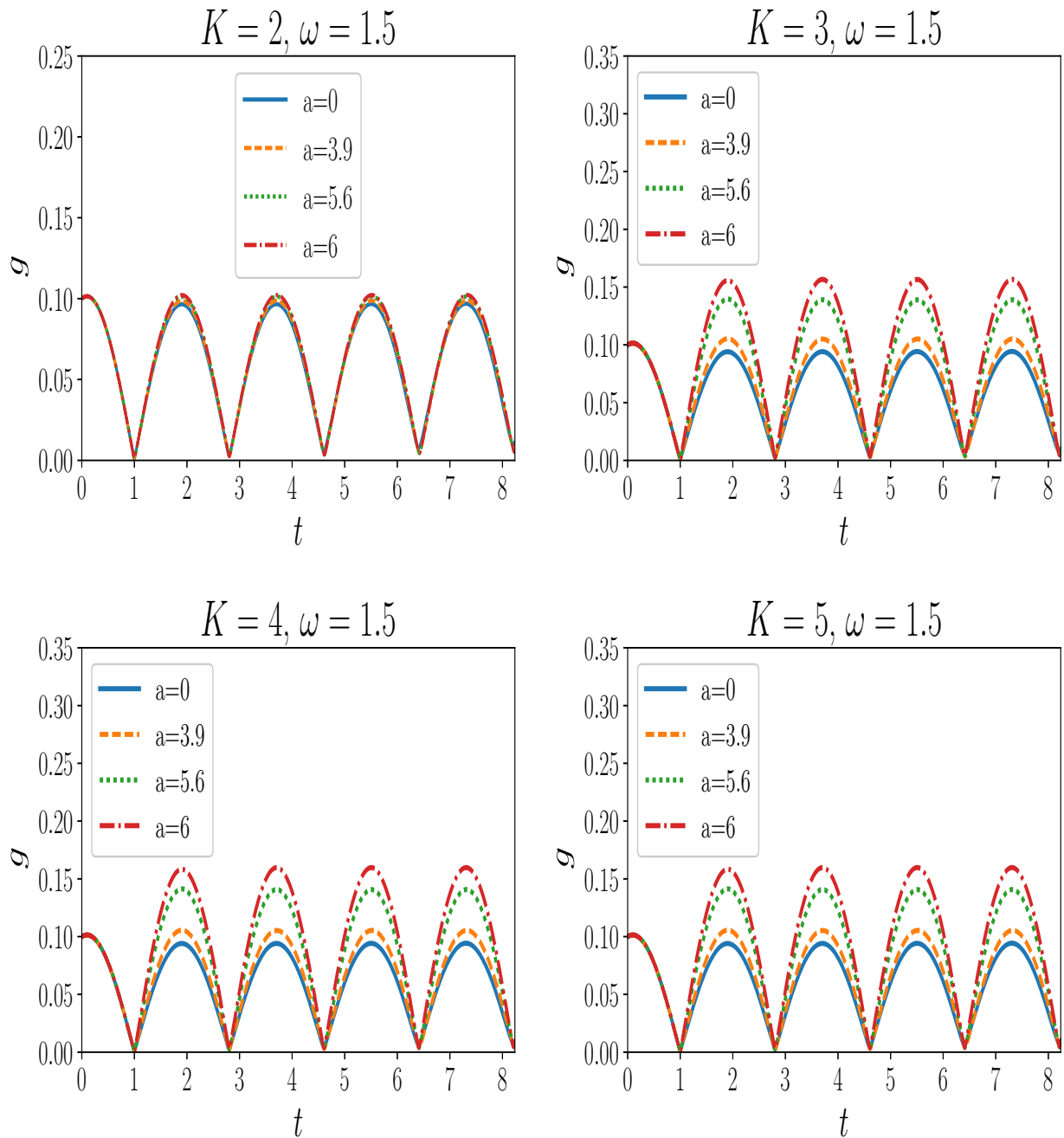


Figure 3.17: Time variation of the laser amplitude g , for $K = 2, 3, 4, 5$ and different values of the radiative recombination coefficient a indicated in the graphs. $\sigma = 0.8, \omega_0 = 1.38, \tau_0 = 0.58, \delta = -0.5, \mu = 0.5, \nu = 0.5, \gamma_0 = 0.18, \alpha = 0.6$.

Table 3.2: Parameters for which pulses is stable: $\omega = 1.5$ rad/fs

Laser amplitude	Power density	Laser fluence	Laser spot diameter
$K = 2, g = 0.11$	$P = 6050 \times 10^{14}$ W/cm ²	$F = 6050$ J/cm ²	$d_{sp} = 0.005$ cm
$K = 3, g = 0.158$	$P = 12482 \times 10^{14}$ W/cm ²	$F = 12482$ J/cm ²	$d_{sp} = 0.005$ cm
$K = 4, g = 0.16$	$P = 12800 \times 10^{14}$ W/cm ²	$F = 12800$ J/cm ²	$d_{sp} = 0.005$ cm
$K = 5, g = 0.16$	$P = 12800 \times 10^{14}$ W/cm ²	$F = 12800$ J/cm ²	$d_{sp} = 0.005$ cm

Amorphous Silica Glass parameters
Group velocity dispersion, $\delta = -0.5$ fs ² /cm
Kerr nonlinearity coefficient, $\sigma = 0.8$ cm W ⁻¹
Electron lifetime $\tau_0 = 0.58$ fs
Electron plasma frequency $\omega_0 = 1.38$ rad/fs
Avalanche coefficient $\nu = 0.5$ cm ² /J
Loss coefficient of the multiphoton absorption in amorphous silica, $\mu = 0.5$ cm ⁻¹
Radiative recombination coefficient, $\mathbf{a} = 6$ cm ³ fs ⁻¹

3.3.3 Summary

The above results shown that, as we increase the femtosecond laser frequency from $\omega = 1.3$ rad/fs (table 3.1) to $\omega = 1.5$ rad/fs (table 3.2), the pulsed wave becomes stable for large values of radiative recombination coefficient. Furthermore, we also observed that, by increasing the pulse frequency and decreasing the focused area, the laser power applied to the amorphous silica glass increases as the recombination coefficient increase. The reduction of the focused area from 0.0025 cm² to 0.00002 cm² is motivated by the fact that, mark width depends on the focused spot size and the focused spot size too is a function of the focal length lens. Indeed, it is revealed experimentally that as the focal length lens is shift a way from the material, the focused area also increases which ultimately increase the mark width and decrease the laser power per unit area. From literature, we found that, decreasing the focused area ultimately decreases the laser beam spot diameter on the material, which leads to a very fine engraving [73]. Indeed with the focused area of 0.00002 cm², we were able to obtain the laser bean spot size of $50\mu\text{m}$, which is well in the range of the laser beam spot size $20 - 100\mu\text{m}$ given in [45].

In this chapter, we carried out a theoretical investigations of the effects of the competition between multi-photon absorption, group-velocity dispersion and electron-hole radiative recombination processes, on the continuous-wave and femtosecond lasers dynamics and stability (i.e. laser beam spot) during inscription on amorphous silica glass. Mathematically the model is represented by a complex Ginzburg-Landau equation with cubic nonlinearity plus a K -order nonlinearity accounting for K -photon absorption processes, coupled to a Drude-type equation with a term quadratic in the electron plasma density, accounting for radiative recombination processes. Given that a laser dynamics in amorphous silica is intimately linked with the specific laser operation regime during the laser inscriptions on amorphous silica, we considered two distinct regimes of laser dynamics namely continuous and pulsed waves. First addressing continuous-wave regime and their stability, a linear-stability analysis was carried out following the modulational-instability theory. In this purpose, a global stability picture have been proposed in terms of a two-dimensional complex parameter space, mapped by the real and imaginary parts of the coefficient of spatial amplification of perturbation over a finite range of values of the modulation frequency. Next we discussed the system dynamics in the full nonlinear regime (for laser operating in femtosecond mode), starting with fixed-point solutions and then carrying out numerical simulations, using a fourth-order Runge-Kutta algorithm, to generate non-linear time series of femtosecond laser amplitude and the electron plasma density, for different values of the radiative recombination coefficient \mathbf{a} and the multi-photon absorption rate K .

■ *General Conclusion and Perspectives*

The objective of this thesis was to propose a theoretical study to explore the effects of the competition between multi-photon absorption, group velocity dispersion and electron-hole radiative recombination processes on the continuous-wave and femtosecond laser dynamics and stability during inscription on amorphous silica glass. This analysis was supposed to allow us to provide the set of parameters of the model that could be considered for an efficient laser inscription. This work is the very first theoretical attempt to understand the stability of laser in engraving processes and results could help better understand the process, as well as the regime when the laser is expected to operate as a continuous wave or as a pulsed regime. Understanding the stability of our model here contributes to the finesse of the characters to be printed on amorphous silica glass. To achieve our goal, we have divided our work into three main parts within chapter 3.

In the first part of chapter 3, we investigated the continuous-wave laser stability (spot) by neglecting the effect of the radiative recombination phenomenon in the plasma generated. By carrying out the modulational-instability analysis of the model that we have considered for this process, we predicted a rich stability property for the cw regime. In this case, we showed that when the modulation frequency of the perturbation parameter is zero, the continuous-wave laser will be always stable and the desired size of a character will be possible to engrave on amorphous silica glass. At non zero modulation frequency of the small perturbation induced by the presence of plasma, the continuous-wave laser is stable in the normal dispersion regime for any value of photon number K . In this case, the set of optimal parameters of the model that will provide a better engraving condition are summarized as follows: a continuous-wave laser frequency $\omega_l = 2.3 \times 10^{-15}$ rad/fs and laser power $I_0 = 2.5$ KW/cm² on amorphous silica of band gap $E_g = 7.6$ eV with a group velocity dispersion $\delta = 0.5$ fs²/cm, Kerr nonlinearity coefficient $\sigma = 0.8$ cm W⁻¹, electron lifetime $\tau_0 = 2.5$ fs, plasma frequency $\omega_0 = 0.44$ rad/fs, avalanche coefficient $\nu = 0.5$ cm²/J and the loss coefficient of the multiphoton absorption in amorphous silica glass $\mu = 0.1$ cm⁻¹.

For the second part of our work of chapter 3, the model that we used is an extension of a version discussed in the first part, where the extension is meant to take into account

the contributions of electron-hole radiative recombination processes. This translates into an additional term in the Drude equation quadratic in the electron plasma density, competing with the avalanche impact ionization and the multi-photon ionization. We start with an analysis of the system dynamics in the cw regime. In this purpose we find steady-state solutions and analyse their stability by means of the modulational-instability theory. We constructed a global stability map, which enabled us explore parameter regimes in which cw operations could be stable. For this case in the steady state, we found that in the normal dispersion regime (i.e. $\delta > 0$) of amorphous silica, the continuous-wave laser becomes stable for $K = 5$ suggesting an optimum condition to engrave a character on amorphous silica. The set of optimal parameters that we pointed out for this case are summarized as follows: a continuous-wave laser frequency $\omega_l = 2.3 \times 10^{-15}$ rad/fs and the laser power $I_p = 2.5$ KW/cm² on amorphous silica of band gap $E_g = 7.6$ eV with a group velocity dispersion $\delta = 0.5$ fs²/cm, Kerr nonlinearity coefficient $\sigma = 0.8$ cm W⁻¹, electron lifetime $\tau_0 = 1$ fs, plasma frequency $\omega_0 = 0.2$ rad/fs, avalanche coefficient $\nu = 0.5$ cm²/J, the loss coefficient of the multi-photon absorption in amorphous silica glass $\mu = 0.1$ cm⁻¹ and the radiative recombination coefficient $\mathbf{a} = \mathbf{0.004}$ cm³ fs⁻¹.

In the last part of chapter 3, we investigated the nonlinear solution of the model. To do this, an ansatz was introduced, which aimed at representing a femtosecond laser as a pulse field with a real amplitude and real phase. With the help of this ansatz, the system dynamics was transformed into a set of four first-order ordinary differential equations. This set of first-order ordinary differential equations was solved numerically using a fourth-order Runge-Kutta algorithm, implemented in python under Linux. In this last part, we plotted dynamical quantities (i.e. time series curves of femtosecond laser amplitude and plasma density) of the model for different values of the radiative recombination coefficient \mathbf{a} starting with $\mathbf{a} = \mathbf{0}$ (i.e. when there is no radiative recombination). We found that, when $\mathbf{a} = \mathbf{0}$, there is a fall-off of femtosecond laser amplitude $g(t)$ with time, which is more and more pronounced as K gets larger. We attribute this fall-off to a damping effect induced by the density of electron plasma $\rho(t)$. According to this, the fine character that one would like to print on amorphous silica glass cannot be achieved. However, when \mathbf{a} is increased in a relatively large range of values, $\rho(t)$ decreases exponentially in time tending to its equilibrium value with an increasingly sharp slope. In this case, the femtosecond laser amplitude $g(t)$ is manifestly a pulse train with a peak varying only weakly with \mathbf{a} for $K = 2$. However, as K increases, the maximum of $g(t)$ gets more and more

large and stable with an increasing value of radiative recombination coefficient \mathbf{a} . Moreover, from the data obtained from the time series curves of the dynamics quantities of the model that we have plotted, we showed that as we increase the femtosecond laser frequency from $\omega = 1.3$ rad/fs to $\omega = 1.5$ rad/fs as well as the radiative recombination coefficient $\mathbf{a} = 3.9, 5.6, 6$ (in $\text{cm}^3 \text{fs}^{-1}$), the femtosecond laser pulse stabilizes. In order to compare our simulation results and what could be obtained experimentally, we have reduced the femtosecond laser focused area on amorphous silica glass and we observed that an increase in a pulse frequency induces an increase in power density while the laser beam spot size decreases. This leads to a very fine engraving on amorphous silica. We have obtained four sets of parameters for a femtosecond laser at frequency $\omega = 1.5$ rad/fs. One of them is the photon number $K = 5$, the laser amplitude $g = 0.16$, power density $P = 12800 \times 10^{14} \text{ W/cm}^2$, when engraving amorphous silica having the following parameters: group velocity dispersion $\delta = -0.5 \text{ fs}^2/\text{cm}$, Kerr nonlinearity coefficient $\sigma = 0.8 \text{ cm W}^{-1}$, electron lifetime $\tau_0 = 0.58 \text{ fs}$, plasma frequency $\omega_0 = 1.38 \text{ rad/fs}$, avalanche coefficient $\nu = 0.5 \text{ cm}^2/\text{J}$, loss coefficient of the multi-photon absorption in amorphous silica glass $\mu = 0.1 \text{ cm}^{-1}$ and the radiative recombination coefficient $\mathbf{a} = 6 \text{ cm}^3 \text{ fs}^{-1}$. We used the focused area of 0.00002 cm^2 to obtain the above results. Indeed, with this focused area, we were able to obtain the femtosecond laser beam spot size of $50 \mu\text{m}$, which is well in the range of the laser beam spot size $20 - 100 \mu\text{m}$ given in [45]. This value of the femtosecond laser spot size that we proposed from our analysis can allow to obtain a fine engraving on amorphous silica glass.

For our future work, we shall be considering the electron plasma density at its equilibrium, by assuming that the plasma density will change very slowly with time as compared to the laser field amplitude. Such a consideration could be achieved by doping the material to be engraved therefore contributing significantly to the stability of continuous-wave and femtosecond laser inscription. In addition to this, we shall be considering the effects of electron diffusion and its competitive effects coupled with radiative recombination on laser stability.

References

- [1] F. Dausinger, F. Lichtner, and H. Lubatschowski. Femtosecond technology for technical and medical applications,. *Springer, Berlin*, 2004.
- [2] J. Krüger and W. Kautek. The femtosecond pulse laser: a new tool for micromachining. *Laser Physics*, **9**:30–40, 1999.
- [3] G. Chryssolouris. Laser machining: theory and practice. *1st edt., Springer, New York*, 1991.
- [4] M. Stolze, T. Herrmann, and J. A. L’huillier. Laser applications in microelectronic and optoelectronic manufacturing (lamom) xxi. *Proc. SPIE, March 14th*, **9735**:97350O, 2016.
- [5] A. V. Dostovalov, A. A. Wolf, V. K. Mezentsev, A. G. Okhrimchuk, and S. A. Babin. Quantitative characterization of energy absorption in femtosecond laser micro-modification of fused silica. *Opt. Express*, **23**:25–811, 2015.
- [6] R. R. Gattass and E. Mazur. Femtosecond laser micromachining in transparent materials. *Nature photonics*, **2**:219, 2008.
- [7] A. G. Okhrimchuk, V. K. Mezentsev, H. Schmitz, M. Dubov, and I. Bennion. Cascaded nonlinear absorption of femtosecond laser pulses in dielectrics,. *Laser Phys.*, **19**:1415–1422, 2009.
- [8] S. M. Eaton, G. Cerullo, and R. Osellame. Fundamentals of femtosecond laser modification of bulk dielectrics. *In: Femtosecond Laser Micromachining, Topics in Applied Physics (R. Osellame, G. Cerullo and R. Ramponi, eds.)*, 123:3–18, 2012.
- [9] A. Couairon and A. Mysyrowicz. Femtosecond filamentation in transparent media. *Phys. Rep.*, **441**:47–189, 2007.
- [10] H. Shin and D. Kim. Cutting thin glass by femtosecond laser ablation. *Opt. Laser Technol.*, **102**:1–11, 2018.
- [11] P. K. Shukla, J. Lawrence, and Y. Zhang. Understanding laser beam brightness: a review and new prospective in material processing. *Opt. Laser technol.*, **75**:40–51, 2015.

- [12] Zh. Wang, Y. B. Li, F. Bai, C. W. Wang, and Q. Z. Zhao. Angle-dependent lubricated tribological properties of stainless steel by femtosecond laser surface texturing. *Opt. Laser Technol.*, **81**:60–66, 2016.
- [13] H. B. Xu, J. Hu, H. Sheng, and Z. C. Du. Thermal stress analysis for laser cutting corner with a fluctuant cutting speed in steel plate. *J. Phys. Conf. Ser.*, **633**:0120901–0120907, 2015.
- [14] J. W. Jung and C. M. Lee. Cutting temperature and laser beam temperature effects on cutting tool deformation in laser-assisted machining. In: *Proceedings of IMECS II*, pages 1817–1822, 2009.
- [15] S. M. Eaton, H. Zhang, and P. R. Herman. Heat accumulation effects in femtosecond laser-written waveguides with variable repetition rate. *Optics Express*, **13**:4708–4716, 2005.
- [16] D. Savastru, R. Savastru, S. Miclos, and I. I. Lancranjan. Simulation of laser induced absorption phenomena in transparent materials. *Opt. Laser. in Eng.*, **110**:288295, 2018.
- [17] S. Nolte, M. Will, J. Burghoff, and A. Tünnermann. Longitudinal coherence in cold atom interferometry. *J. Mod. Opt.*, **51**:2533–2540, 2004.
- [18] L. Rihakova and H. Chmelickova. Laser micromachining of glass, silicon, and ceramics. *Journal of Advances in Materials Science and Engineering*, **6**:584–952, 2015.
- [19] M. Sanjay and Y. Vinod. Laser beam micromachining (lbmm)-a review. *Optics and Lasers in Engineering*, **73**:89–122, 2015.
- [20] C.F. Melian. *Recherches concernant la qualité de surface de verre gravé au laser*. PhD thesis, Université Technique de CLUJ-NAPOCA, 2013.
- [21] J.S. Petrovic, V. Mezentsev, H. Schmitz, and I. Bennion. Model of the femtosecond laser inscription by a single pulse. *Opt. Quant. Electron*, **39**:939–946, 2007.
- [22] P. A. Markopoulos and E. D. Manolakos. Ablation study of laser micromachining process with molecular dynamics simulation. *Journal of Engineering and Manufacture*, **1**:1–12, 2015.

- [23] M.Karthigayan, R.Nagarajan, Y. Sazali, P. Paulraj, R. Mohammed, H.A. Shamsudin, and K. Marzuki. A real time marking inspection scheme for semiconductor industries. *Int. J. Adv Manuf Technol*, **34**:926–932.
- [24] E. Wangui, B. W. Ikua, and G. N. Nyakoe. A study on influence of beam orientation in engraving using co_2 laser. *Journal of Sustainable Research in Engineering*, **1**:42–48, 2014.
- [25] J. P. Gordon, H. J. Zeiger, and C. H. Townes. Molecular microwave oscillator and new hyperfine structure in the microwave spectrum of nh_3 ,. *Phys. Rev. A*, **95**:282–284, 1954.
- [26] N. G. Basov and A. M. Prokhorovich. Possible methods of obtaining active molecules for a molecular oscillator. *J. Exptl. Theor. Phys*, **28**:249–250, 1955.
- [27] A. L. Schawlow and C. H. Townes. Infrared and optical masers. *Phys. Rev.A*, **112**:1940–1949, 1958.
- [28] T. H. Maiman. Stimulated optical radiation in ruby. *Nature*, **187**:493–494, 1960.
- [29] K. Audo. *Etude théorique et expérimentale des lasers solides bi-fréquences auto-régulés en bruit d'intensité via des non-linéarités intracavité*. PhD thesis, Optique. Université Rennes 1, Français, 2018.
- [30] William T. Silfvast. *Laser Fundamentals*. First Edition, Cambridge University Press, 1996.
- [31] Orazio Svelto David C. Hanna. *Principles of Lasers*. Fifth Edition, 1982.
- [32] <http://www.physics-and-radio-electronics.com/physics/laser/principlesofworkinglaser.html>., 2020.
- [33] s.s. mao, u f. quériv, s. guizard, x. mao, r.e. russo, g. petite, and p. martin. Dynamics of femtosecond laser interactions with dielectrics. *Appl. Phys. A*, **79**:1695–1709, 2004.
- [34] L. Sudrie. *Propagation non-linéaire des impulsions laser femtosecondes dans la silice*. PhD thesis, Université de Paris XI Orsay, 2015.

- [35] A. Q. Wu, I. H. Chowdhury, and X. Xu. Femtosecond laser absorption in fused silica: Numerical and experimental investigation. *Physical Review B*, **72**:085128, 2005.
- [36] C.J. Chen. *Theoretical Study of Passively Modelocked Laser with fast Saturable Absorber*. PhD thesis, University of Maryland, 1993.
- [37] D. Hélie. *Développement de procédés de micro-usinage de matériaux optiques au laser femtosecond*. PhD thesis, Université Laval Québec, Canada, 2014.
- [38] N.S. Graham, K.Kyriacos, and S.Kate. Advances in femtosecond micromachining and inscription of micro and nano photonic devices. *Frontiers in Guided Wave Optics and Optoelectronics*, 2010.
- [39] C.B. Schaffer, A. Brodeur, J. García, and E.Mazur. Micromachining bulk glass by use of femtosecond laser pulses with nanojoule energy. *Optics letters*, **26**:93–95, 2001.
- [40] C. B. Schaffer. *Interaction of Femtosecond Laser Pulses with Transparent Materials*. PhD thesis, Harvard University Cambridge, Massachusetts, 2001.
- [41] E. Yablonovitch and N. Bloembergen. Avalanche ionization and the limiting diameter of filaments induced by light pulses in transparent media. *Phys. Rev. Lett.*, **29**:907–910, 1972.
- [42] A.H. Hamad. *Effects of Different Laser Pulse Regimes (Nanosecond, Picosecond and Femtosecond) on the Ablation of Materials for Production of Nanoparticles in Liquid Solution*. 2016.
- [43] P. Sachin, B. Sandip, B. Patel, and B. Anup Patel. A review on laser engraving process. *IJSRD-International Journal for Scientific Research and Development*, **3**:2321–0613, 2015.
- [44] P. Deprez, C.F. Melian, F. Breaban, and J.F. Coutouly. Glass marking with co_2 laser: Experimental study of the interaction laser-material. *Journal of Surface Engineered Materials and Advanced Technology*, **2**:32–39, 2012.

- [45] Md. N. Yusoff, S.C. Tam, L.E.N. Lim, and S. Jana. A review of the nd:yag laser marking of plastic and ceramic ic packages. *Journal of Materials Processing Technology*, **42**:95–133, 1994.
- [46] M.C.K. Chua, S. Rao, S.H. Tan, and S.J. Chua. Computer controlled optical system for nd : yag laser plastic integrated circuit package marking. *Proc. Asia Pacific Conf. On Optics Technology, Institute of Physics, Singapore*, pages 1–18, 1988.
- [47] Adelina Han and Dinu Gubencu. Analysis of the laser marking technologies. *Nonconventional Technologies Review*, **4**, 2008.
- [48] L. Lyubomir, D. Hristina, and N. Pavels. Laser marking methods. In *Proceedings of the 10th International Scientific and Practical Conference*. Rezekne, Latvia Higher Education Institution, 2015.
- [49] M. Hoffmann, F. Brietenfellner, N. Buhler, R.C. Sykes, and H. Gugger. High contrast and intact surface-a challenge in laser marking of plastics. *Proc. SPIE*, **744**:156–180, 1987.
- [50] J. P. Dudeja. Laser application in apparel industry. *International Journal of Advanced Scientific Technologies in Engineering and Management Sciences*, **4**, 2018.
- [51] Barcode 1, adams communications. <http://www.adams1.com/stack.html>, 2020.
- [52] Data matrix codes vs. qr codes, barcode labels. <https://www2.camcode.com/asset-tags/barcodes-data-matrix-vs-qr-codes/>, 2020.
- [53] Understanding laser marking technologies. www.linx.co.uk/laser-coders, 2020.
- [54] A.D. Compaan, I.Matulionis, and S. Nakade. Laser scribing of polycrystalline thin films. *Optics and Lasers in Engineering*, **34**:15–45, 2000.
- [55] J. QI, K.L. Wang, and Y.M.Zhu. A study on the marking process of stainless steel. *Material Processing Technology*, **139**:273, 2003.
- [56] J.B. Willis. Techniques and applications of laser marking. *Proc. 1st Int. Conf. on Lasers in Manufact., Brighton, UK*, pages 53–62, 1983.

- [57] H.K. Bernhard. State of the art in laser marking and engraving. *Proc.SPIE*, **744**, 1987.
- [58] D.V. Perry Jr. and W.H. Huffines. Quality evaluation of co_2 and nd:yag laser marking of ceramic chip capacitors. *IEEE Proc. 36th Electronic Components Conf.*, pages 655–658, 1986.
- [59] Y.M. Noor. *Marking of plastic and ceramic IC packages using a pulsed Nd : YAG laser*. PhD thesis, Nanyang Technological University, Singapore, 1993.
- [60] M. Bass. *Laser Materials Processing, North-Holland, New York, USA*. 1983.
- [61] J.F. Ready. *Lasers in Modern Society, Society of Manufacturing Engineers*. 1979.
- [62] B. Bernard. Laser marking techniques, lasers in materials processing. *American Society for Metals, Los Angeles, USA*, pages 48–52, 1983.
- [63] S.C. Tam, Y.M. Noor, L.E.N. Lim, S. Jana, L.J. Yang, M.W.S. Lau, and C.Y. Yeo. Marking of leadless ic chip carriers with a pulsed *nd : yag* laser. *Proc. I. Mech. Eng.*, **207**:179–192, 1993.
- [64] O.D.D. Soares and M. Perez-Amor. *Applied laser Tooling, Nijhoff, Boston, USA*. 1987.
- [65] D. Belforte and M. Lemitt. *The Industrial Laser Annual Handbook 1990 Edition, Pen Well, Books, USA*. 1990.
- [66] Th. Dumont, T. Lippert, A. Wokaun, and P. Leyvray. Laser writing of 2d data matrices in glass. *Thin Solid Films*, **453**:42–45, 2004.
- [67] K.Miura, Q. Jianrong, S.Fujiwara, S.Sakguchi, and K.Hirao. Three-dimensional optical memory with rewriteable and ultrahigh density using the valence-state change of samarium ions. *Apply. phy. Lett*, **80**:13, 2012.
- [68] S. Shuttleworth. Optimisation of laser wavelength in the ablation sampling of glass materials. *Applied Surface Science*, **96**:513–517, 1996.
- [69] R. Chanchani. Processibility of thin-film, fine-line pattern on aluminium nitride substrates for hics. *IEEE*, pages 584–588, 1988.

- [70] R. Morrel. *Handbook of Properties of Technical and Engineering Ceramics Part I: An Introduction for the Engineer and Designer, Her Majesty's Stationery Office, London.* Second Edition, 1985.
- [71] A. Böcker, H.G. Brokmeier, and H.J. Bunge. Determination of preferred orientation textures in al_2o_3 ceramics. *J. Eur. Ceramic Soc.*, **8**:187–194, 1991.
- [72] H. Kröckel, M. Merz, and O. Van der Biest (Eds.). *Ceramics in Advanced Energy Technologies, Reidel, (Dordrecht).* First Edition, 1984.
- [73] J. Peter, B. Doloi, and B. Bhattacharyya. Analysis of nd: Yag laser marking characteristics on alumina ceramics. *J. Inst. Eng. India Ser.*, **94**:287–292, 2013.
- [74] A.N. Samant and N.B. Dahotre. Laser machining of structural ceramics: A review. *Journal of the European Ceramics Society*, **29**, 2009.
- [75] J. Hajkova. Parameterization of laser burned samples and its usage in data description and simulation. *Proceedings 23rd European Conferences on Modelling and simulation*, 2009.
- [76] J.P. Desbiens and P. Masson. Arf excimer laser micromachining of pzrex, sic and pzt for rapid prototyping of mems component. *Journal Sensor and Actuators*, **136**:554–563, 2007.
- [77] H. Soder and E. Audouard. Utilisation des lasers femtosecondes pour le marquage du verre , dans le cadre de la lutte contre la contrefaçon. <http://www.photoniques.com>, 2011.
- [78] M. Lebugle. *Étude des phénomènes d'absorption laser en régime femtoseconde pour l'ablation de matériaux diélectriques.* PhD thesis, Université D'AIX-Marseille, 2013.
- [79] V. Leboeuf. *Caractérisation cinétique et structurale de verres sodo-silicatés soumis à un échange ionique au potassium.* PhD thesis, Université d'Orléans, 2016.
- [80] www.translume.com/index.php/resources/item/186-fused-silica-material-properties, 2020.
- [81] R. Kitamura, L. Pilon, and M. Jonasz. Optical constants of silica glass from extreme ultraviolet to far infrared at near room temperature. *Applied optics*, **46**:8118–8133, 2007.

- [82] www.base-materials.heraeus-conamic.com, 2020.
- [83] F. Nürnberg, B. Kühn, and K. Rollmann. Metrology of fused silica. *Conference Paper*, 2016.
- [84] *Document 1: Solide cristallin et solide amorphe*.
- [85] K. Mishchik. *Ultrafast laser-induced modification of optical glasses: a spectroscopy insight into the microscopic mechanisms*. PhD thesis, Université Jean Monnet-Saint-Étienne, 2012.
- [86] N. Varkentina, O. Utéza, N. Sanner, B. Chimier, M. Sentis, and T. Itina. Absorption of femtosecond laser pulse in fused silica: experiments and modelling. *Laser Applications in Microelectronic and Optoelectronic Manufacturing (LAMOM) XVI*, **7920**:792003, 2011.
- [87] W. H. Zachariasen. The atomic arrangement in glass. *Journal of the American Chemical Society*, **54**:3841–3851, 1932.
- [88] A. Q. Wu, I. H. Chowdhury, and X. Xu. Femtosecond laser absorption in fused silica: Numerical and experimental investigation. *Physical Review B*, **72**, 2005.
- [89] Y. Sanichiro, D. H. Reitze, B.D. Tanner, and J. D. Mansell. Method for measuring small optical absorption coefficients with use of a shack-hartmann wave-front detector. *Applied optics, Optical Society of America*,, **42**:24, 2003.
- [90] P. Holmberg. *Laser processing of Silica based glass*. PhD thesis, Royal Institute of Technology Stockholm, Sweden, 2015.
- [91] <https://www.google.cm/search?source=univ&tbm=isch&q=continuous-wave+laser+profile/>, 2020.
- [92] L. Bergé and S. Skupin. Modeling ultrashort filaments of light. *Discrete and continuous dynamical systems*, **23**(4):1099–1139, 2009.
- [93] S. Skupin. *Nonlinear Dynamics of Trapped Beams*. PhD thesis, Friedrich-Schiller-Universität Jena, 1976.

- [94] A. Couairon, E. Brambilla, T. Corti, D. Majus, O. de Ramírez Góngora, and M. Kolesik. Practitioner's guide to laser pulse propagation models and simulation. *Eur. J. Special Topics*, **199**:5–76, 2011.
- [95] P. Sprangle, E. Esarey, and J. Krall. Self-guiding and stability of intense optical beams in gases undergoing ionization. *Physical Review E*, **54**(4), 1996.
- [96] Ch. Cheng, E. M. Wright, and J. V. Moloney. Generation of electromagnetic pulses from plasma channels induced by femtosecond light strings. *Physical Review Letters*, **87**(21), 2001.
- [97] L. Tatarinova. *Analytical Study of Light Propagation in Highly Nonlinear Media*. PhD thesis, Universität Kassel, 2009.
- [98] A. Vincotte. *Propagation non-linéaire d'impulsions laser ultra-courtes dans les milieux transparents*. PhD thesis, Université Bordeaux 1, 2006.
- [99] L. Bergé and A. Couairon. Nonlinear propagation of self-guided ultra-short pulses in ionized gases. *J. Physics of Plasma*, **7**(1), 2000.
- [100] Q. Feng, J. V. Moloney, A. C. Newell, E. M. Wright, K. Cook, P. K. Kennedy, D. X. Hammer, B. A. Rockwell, and C. R. Thompson. Theory and simulation on the threshold of water breakdown induced by focused ultrashort laser pulses. *Journal of Quantum Electronics*, **33**(2), 1997.
- [101] N. B. Dahotre and A. Samant. Laser machining of advanced materials. *CRC Press, Taylor and Francis*, 2014.
- [102] C. J. Chen, P. K. A. Wai, and C. R. Menyuk. Self-starting of passively mode-locked lasers with fast saturable absorbers. *Op. Lett.*, **20**:350–352, 1995.
- [103] A. M. Dikandé, J. Voma Titafan, and B. Z. Essimbi. Continuous-wave to pulse regime for a family of passively mode-locked lasers with saturable nonlinearity. *J. Opt.*, **19**:1055041, 2017.
- [104] D. Jr. Jubgang Fandio, A. M. Dikande, and A. Sunda-Meya. Continuous-wave stability and multipulse structures in a universal complex ginzburg-landau model for passively

- mode-locked lasers with a saturable absorber. *Journal of the Optical Society of America B*, **37**, 2020.
- [105] https://en.wikipedia.org/wiki/Runge%E2%80%93Kutta_methods, 2020.
- [106] Y.S. Kivshar and B.A. Malomed. Dynamics of solitons in nearly integrable systems. *Rev. Mod. Phys.*, **61**(763), 1989.
- [107] N.R. Pereira and L. Stenflo. Nonlinear schrödinger equation including growth and damping. *Phys. Fluids*, **20**(1733), 1977.
- [108] J.M. Soto-Crespo, N. Akhmediev, and V. Afanasjev. Stability of the pulselike solutions of the quintic complex ginzburg-landau equation. *J. Opt. Soc. Am. B*, **13**(1439), 1996.
- [109] J.M. Soto-Crespo, N. Akhmediev, and G. Town. Continuous-wave versus pulse regime in a passively mode-locked lasers with a fast saturable absorber. *J. Opt. Soc. Am. B*, **19**:234–242, 2002.
- [110] J.M. Soto-Crespo, M. Grapinet, Ph. Grelu, and N. Akhmediev. Bifurcations and multiple-period soliton pulsations in a passively mode-locked fiber laser. *Phys. Rev. E*, **70**:0666121, 2004.
- [111] D. Jr. Jubgang Fandio, A.M. Dikandé, and A. Sunda-Meya. Elliptic solitons in optical fiber media. *Phys. Rev. A*, **92**:0538501, 2015.
- [112] D. Jr. Jubgang Fandio and A. M. Dikandé. Pulse train uniformity and nonlinear dynamics of soliton crystals in mode-locked fiber ring lasers. *J. Opt. Soc. Am. B*, **34**:2721–2730, 2017.
- [113] R.D. Dikandé Bitha and A.M. Dikandé. Elliptic-type soliton combs in optical ring microresonators. *Phys. Rev. A*, **97**:0338131, 2018.
- [114] J.M. Soto-Crespo and N. Akhmediev. Multisoliton regime of pulse generation by lasers passively mode locked with a slow saturable absorber. *J. Opt. Soc. Am. B*, **16**:674–677, 1999.

- [115] V. Mezentsev, M. Dubov, J. S. Petrovic, Jürgen Dreher I. Bennion, and Rainer Grauer. Role of plasma in femtosecond laser pulse propagation. In *23rd Summer School and International Symposium*, 2006.
- [116] L. Turi A. Fürbach, X. Peng and F. Krausz. Compact high-energy picosecond laser for micromachining applications. *Appl. Phy. B*, **78**:261–264, 2004.
- [117] Y. Dai, G. Yu, M. He, H. Ma, X. Yan, and G. Ma. High repetition rate femtosecond laser irradiation-induced elements redistribution in ag-doped glass. *Appl. Phy. B*, **103**:663, 2011.
- [118] K. Venkatakrisnan, B. Tan, and B. K. A. Ngoi. Femtosecond pulsed laser ablation of thin gold film. *Opt. Laser Technol.*, **34**:199, 2002.
- [119] B. Tan, K. Venkatkrishnan, N.R. Sivakumar, and G. K. Gan. Laser drilling of thick material using femtosecond pulse with a focus of dual-frequency beam. *Opt. Laser Technol.*, **35**:199, 2003.
- [120] C. W. Hee, B. K. A. Ngoi, L. E. N. Lim, K. Venkatakrisnan, and W. L. Liang. Effect of polarization on femtosecond pulsed laser ablation on surface relief gratings. *Opt. Laser Technol.*, **37**:93, 2005.
- [121] K. T. Paula, G. Gaál, G. F. B. Almeida, M. B. Andrade, and C. R. Mendonca. Femtosecond laser micromachining of polylactic acid/graphene composites for designing interdigitated microelectrodes for sensor applications. *Opt. Laser Technol.*, **101**:74, 2018.
- [122] C.B.Schaffer, J.F. García, and E. Mazur. Bulk heating of transparent materials using a high-repetition-rate femtosecond laser. *Applied Physics A*, **76**:351–354, 2003.
- [123] K. Minoshima, A. W. Kowalevich, I. Hartl, E. P. Ippen, and J. G. Fujimoto. Photonic device fabrication in glass by use of nonlinear materials processing with a femtosecond laser oscillator. *Opt. Lett.*, **26**:1516–1518, 2001.
- [124] J. R. Grenier, L. A. Fernandes, and P. R. Herman. Femtosecond laser inscription of asymmetric directional couplers for in-fiber optical taps and fiber cladding photonics. *Optics Express*, **23**:16760–16771, 2015.

- [125] I.S. Aranson and L. Kramer. The world of the complex ginzburg-landau equation. *Rev. Mod. Phys.*, **74**:99–143, 2002.
- [126] L. Sudrie, A. Couairon, M.Franco, B. Lamouroux, B.Prade, S. Tzortzakis, and A. Mysyrowicz. Femtosecond laser-induced damage and filamentary propagation in fused silica. *Phys. Rev. Lett.*, **89**:1866011–1866014, 2002.
- [127] L. A. Siiman, J. Lumeau, and L. B. Glebov. Nonlinear photoionization and laser-induced damage in silicate glasses by infrared ultrashort laser pulses. *Appl. Phy. B*, **96**:127–134, 2009.
- [128] A. Valenzuela, A. Munson, A. Porwitzky, M. Weidman, and M. Richardson. Comparison between geometrically focused pulses versus filaments in femtosecond laser ablation of steel and titanium alloys. *Appl. Phy. B*, **116**:485–491, 2014.
- [129] V. E. Zakharov and L. A. Ostrovsky. Modulation instability: The beginning. *Physica D*, **238**:540–548, 2009.
- [130] A. Rapaport, F. Szipöcs, and M. Bass. Dependence of two-photon absorption excited fluorescence in dye solutions on the angle between the linear polarizations of two intersecting beams. *Appl. Phy. B*, **78**(65-72), 2004.
- [131] Ch.Tao, SI. Jinhai, H. Xun, K. Shingo, M. Kiyotaka, and H. Kazuyuki. Luminescence of black silicon fabricated by high-repetition rate femtosecond laser pulses. *Appl. Phy. B*, **110**:073106, 2011.
- [132] S.O. Kasap. *Optoelectronic Prentice Hall*. Second Edition, 1999.
- [133] Orazio Svelto. *Principles of Lasers*. Fifth Edition 2004.
- [134] Peter W. Milonni and Joseph H. Eberly. *Lasers Physics*. First Edition, 1988.
- [135] Peter W. Milonni and Joseph H. Eberly. *Laser physics*. Second Edition, 2010.
- [136] A. Javan, W. R. Bennett, and D. H. Herriott. Population inversion and continuous optical maser oscillation in a gas discharge containing a he-ne mixture. *Phys. Rev. Lett.*, **6**:106, 1961.

- [137] William T. Silfvast. *Laser fundamentals*. Second Edition, Cambridge University press, 2004.
- [138] Chunlei Guo Subhash Chandra Singh, Haibo Zeng and Weiping Cai. *Lasers: Fundamentals, Types, and Operations*. 2012.
- [139] W. R. Bennett. Supplement 1, optical masers. *Applied Optics*, **24**, 1962.
- [140] B. S. Williams, H. Callebaut, S. Kumar, Q. Hu, and J. L. Reno. 3.4 – thz quantum cascade laser based on longitudinal-optical-phonon scattering for depopulation. *Appl. Phys. Lett*, **82**:1015–1017.
- [141] M.A. Choudhury. Making your mark and electronic packaging. *Prod.*, **26**:477–48, 1986.
- [142] G.D. Poulin and P.A. Eisele. A versatile excimer laser processing system. *Proc. SPIE -Fiber Laser*, page 88, 1988.
- [143] A. Sethand and J. Scaroni. Ceramic component marking with yag lasers. *Semiconductor Int.*, **9**:80–83, 1986.
- [144] J. Miller. Laser marking enhances ic identification. *Eval. Eng.*, **29**:20–22, 1990.
- [145] G.D. Poulin, P.A. Eisele, and T.A. Znotins. Advances in excimer laser material processing,. *Int. Cong. Optical and Science En., Hamburg, Germany,*, 1988.
- [146] G. Holizinger, K. Kosanke, and W. Menz. Printing of part numbers using a high power laser beam. *Optics Laser Technol.*, **5**:256–265, 1973.
- [147] D. Wildmann and B. Pietsch. Industrial marking of laser-sensibly pigmented plastics. *German Plastics*, **79**:18–20.
- [148] R.L. Stevenson. Nd:yag laser marking of gold plated kovar packages. *Hybrid Circuit Technol.*, **7**:52–54, 1990.
- [149] K. Murakami, M. Moriyasu, and S. Hiramoto. Development of laser marking for ic packages. *Preprint*.
- [150] R.R. Tummala and E.J. Rymaszewski. *Microelectronics Packaging Handbook, Van Nostrand Reinhold, New York,*. Second Edition, 1989.

- [151] M. Pecht. *Handbook of Electronic Package Design*, Marcel Dekker, New York. First Edition 1991.
- [152] W.B. Lan. *Laser Processing of Thin Films and Microstructures: Oxidation, Deposition and Etching of Insulators*, Springer, Berlin. First Edition, 1987.
- [153] H.K. Bernhard. State of the art in laser marking and engraving. *Proc. SPIE*, pages 185–189, 1987.
- [154] D. Crater. Multiple roles of laser marking. *Laser Optonics*, **6**:63–65, 1987.
- [155] J.T. Luxon and D.E. Parker. *Industrial Lasers and their Applications*, Prentice-Hall International Edition, New Jersey, USA. Second Edition, 1992.
- [156] M. Nelkon and P. Parker. *Advanced Level Physics, 3rd ed.*, Heinemann, London. 1975.
- [157] W.M. Steen. *Surface engineering with lasers*. First Edition, 1987.
- [158] Zhang W. Tao YL, Chen H. Time scale effects in laser material removal. *a review. Int J Adv Manuf Technol*, **26**:598–608, 2005.
- [159] C.Hua and JP. Longtin. Modeling optical breakdown in dielectrics during ultrafast laser processing. *Appl. Opt.*, **40**:3124–3131, 2001.
- [160] D. Ashkenasi, G.Muller, A. Rosenfeld, R.Stoian, IV.Hertel, and NM. Bulgakova. Fundamentals and advantages of ultrafast micro-structuring of transparent materials. *Appl Phys A*, **77**:223–228, 2003.
- [161] SJ. Qin and WJ. Li. Process characterization of fabricating 3d micro channel systems by laser-micromachining. *Sens Actuator A*, **97**:749–757, 2002.
- [162] J. Meijer. Laser beam machining (lbm) state of the art and new opportunities. *J. Mater Process Technol*, **149**:2–17, 2004.
- [163] *Laser Marking, High Performance Thermoplastics LATI*. printed by C and I Italy, 2008.
- [164] B. A. Serinsu. The effects of laser engraving methods on ceramic surfaces. *The Journal of Academic Social Science Studies*, **66**:197–210, 2018.

- [165] D. Karnakis. *Ultrafast Laser Nanomachining: Doing More With Less*. Commercial MicroManufacturing, Oxford, 2008.
- [166] Laser marking measurement. <http://www.cybertechtechnologies.com>, 2020.
- [167] J. Lawrence. *Advances in Laser Materials Processing: Technology, Research and Application*. Second Edition, Elsevier, Amsterdam, 2018.
- [168] A. Pilipovic, T. Brajliah, and I. Drstvensek. Influence of processing parameters on tensile properties of sls polymer product. *Journal of Polymers*, **10**:1208, 2018.
- [169] A. A. Tseng, Ch. Ying-Tung, C. Choung-Lii, M. Kung-Jeng, and T.P. Chen. Recent developments on microablation of glass materials using excimer lasers. *Optics and Lasers in Engineering*, **45**, 2007.
- [170] R. K. Maher. *Silica (Amorphous)*. First Edition, 1979.
- [171] S. Vukelic, S. Ryu, B. Gao, and Y.L. Yao. Structural modification of amorphous fused silica under femtosecond laser radiation. *Proceedings of the International Manufacturing Science and Engineering Conference*, 2008.
- [172] Harvey segur, Diane henderson, John carter, Joe hammack, Cong-mingli, Dana Pheiff, and Katherine Sacha. Stabilizing the benjamin-feir instability. *J. Fluid Mech.*, **539**:229–271, 2005.
- [173] R. Stoian, A. Mermillot-Blondin, S.W. Winkler, A. Rosenfeld, I.V. Hertel, M. Spyridaki, E. Koudoumas, P. Tzanetakis, C. Fotakis, I.M. Burkanov, and N.M. Bulga-kova. Temporal pulse manipulation and consequences for ultrafast laser processing of materials. *Optical Engineering*, **44**:05, 2005.
- [174] <http://www.femtoprint.eu/>, 2020.
- [175] K. Mishchik, G. Cheng, G. Huo, M. Burakov, C. Mauclair, A. Mermillod-Blondin, A. Rosenfeld, Y. Ouerdane, A. Boukenter, O. Parriaux, and R. Stoian. Nanosize structural modifications with polarization functions in ultrafast laser irradiated bulk fused silica. *Optics Express*, **18**:24, 2010.

Python code for fourth-order Runge-Kutta algorithm used in chapter 3

```
import matplotlib.pyplot as plt
import numpy as np
import cmath as cm
%matplotlib inline

def RK4(fcn, Tspan, I, Nt, k,a):

t = np.linspace(Tspan[0], Tspan[1], Nt+1)
dt = t[1] - t[0]

f_ = lambda u, t, k,a: np.asarray(fcn(u, t, k,a))
if isinstance(I, (float, int)):
u = np.zeros(Nt+1) # u[k] is the numerical solution
else:
I = np.asarray(I)
neq = I.size
u = np.zeros((Nt+1, neq))

u[0] = I
for n in range(Nt):
k1 = dt*f_( u[n], t[n], k,a)
k2 = dt*f_( u[n] + 0.5*k1, t[n] + 0.5*dt, k,a)
k3 = dt*f_( u[n] + 0.5*k2, t[n] + 0.5*dt, k,a)
k4 = dt*f_( u[n] + k3, t[n+1], k,a)
u[n+1] = u[n] + ( k1 + 2.0 * ( k2 + k3 ) + k4 ) / 6.0
return u, t
```

Appendix

```
gamma=0.18; delta=-0.5; nu=0.5; omegtau=0.8;
sigma=0.8; mu=0.5; alpha =0.6; omega=1.5;

def fcn(u, t, k,a):
Mprime=((gamma*u[3])/delta)-(2*u[0]*u[1]/u[2])+
mu*(u[2]**(2*k-2))/delta
yprime=((omega+(delta*u[0]**2))+gamma*omegtau*u[3])*u[2]/delta
+sigma*(u[2]**3)/delta
gprime=u[1]
rhoprime=(nu*u[3]*u[2]**2)+(alpha*u[2]**(2*k))-a*u[3]**2
return [Mprime, yprime, gprime, rhoprime]

import numpy as np
import matplotlib.pyplot as plt
Tspan = [0.,10]
Nt = 1000
plt.xticks(fontsize=10)
plt.yticks(fontsize=10)
plt.rc('font', family='serif', serif='cm10')
plt.rc('text', usetex=True)
#intial Condition:
M0=0.002; y0=0.03; g0=0.1; rho0=0.1
#M0=0.05*np.pi; y0=0.3; g0=0.7; rho0=0.8
I = np.stack((M0,y0,g0,rho0))
k=0
#A=[0.001,0.002,0.003,0.01,0.02]
A=[0,3.9,5.6,6 ]
lstyle=['solid','dashed','dotted','dashdot']
```

```
counter = 0
for a in A:
u, t = RK4(fcn, Tspan, I, Nt, k+2,a)
plt.plot(t, u[:,0],'-',linestyle=lstyle[counter],label="a
="+str(a),linewidth=1.5)
plt.title(r'$K = $ '+str(k+2)+' , '+r'$\omega
= 1.5$ ',fontsize=25)
counter=counter+1
#plt.ylim((0,12))
plt.xlabel(r'$t$',fontsize=22)
plt.ylabel(r'$M$',fontsize=22)
plt.legend(loc='best', fontsize=14)
plt.savefig('/home/peguykameni/Videos/M-t2.eps',dpi = 10000)
plt.show()

import numpy as np
import matplotlib.pyplot as plt
#Tspan = [0.,11]
Tspan = [0.,11]
Nt = 1000
plt.rc('font', family='serif', serif='cm10')
plt.rc('text', usetex=True)
#intial Condition:
M0=0.002; y0=0.03; g0=0.1; rho0=0.1
#M0=0.05*np.pi; y0=0.3; g0=0.7; rho0=0.8
I = np.stack((M0,y0,g0,rho0))
k=0
#A=[0.001,0.002,0.003,0.01,0.02]
```

```
A=[0,3.9,5.6,6]
lstyle=['solid','dashed','dotted','dashdot']
counter = 0
for a in A:
u, t = RK4(fcn, Tspan, I, Nt, k+2,a)
plt.plot(t, u[:,1],'-',linestyle=lstyle[counter],
label="a="+str(a),linewidth=1.5)
plt.title(r'$K = $ '+str(k+2)+' , '+r'$\omega = 1.5$ ',fontsize=25)
counter=counter+1
#plt.ylim((0,12))
plt.xlabel(r'$t$',fontsize=22)
plt.ylabel(r'$y$',fontsize=22)
plt.legend(loc="upper left",fontsize=11.4)
plt.savefig('/home/peguykameni/Videos/y-t2.eps',dpi = 10000)
plt.xlim((0,11))
#plt.grid(True)
plt.show()
import numpy as np
import matplotlib.pyplot as plt
plt.xticks(fontsize=20)
plt.yticks(fontsize=20)
Tspan = [0.,8.3]
#Tspan=[0.,10]
Nt = 1000
plt.rc('font', family='serif', serif='cm30')
plt.rc('text', usetex=True)
#intial Condition:
```

Appendix

```
M0=0.002; y0=0.03; g0=0.1; rho0=0.1
#M0=0.05*np.pi; y0=0.3; g0=0.7; rho0=0.8
I = np.stack((M0,y0,g0,rho0))
k=0
#A=[0.1,0.2,0.3,0.4,0.5]
A=[0,3.9,5.6,6]
lstyle=['solid','dashed','dotted','dashdot']
counter = 0
for a in A:
u, t = RK4(fcn, Tspan, I, Nt, k+2,a)
plt.plot(t, u[:,2],'-',linestyle=lstyle[counter],label=
"a="+str(a),linewidth=2.5)
plt.title(r'$K = $ ' +str(k+2)+', '+r'$\omega = 1.5$ ',fontsize=28)
counter=counter+1
plt.ylim((0,0.28))
plt.xlabel(r'$t$',fontsize=30)
plt.ylabel(r'$g$',fontsize=30)
plt.legend(loc="upper center",fontsize=17.2)
#plt.legend(loc='best', fontsize=14)
plt.tight_layout()
plt.savefig("/home/peguykameni/Documents/s5k2.png")
plt.xlim((0,8.236))

#plt.grid(True)
plt.show()

import numpy as np
import matplotlib.pyplot as plt
```

```
plt.xticks(fontsize=22)
plt.yticks(fontsize=22)
Tspan = [0.,10]
Nt = 10000
#intial Condition:
plt.rc('font', family='serif', serif='cm30')
plt.rc('text', usetex=True)
M0=0.002; y0=0.03; g0=0.1; rho0=0.1
#M0=0.05*np.pi; y0=0.3; g0=0.7; rho0=0.8
I = np.stack((M0,y0,g0,rho0))
k=0
#A=[0.005]
A=[0,0.2,0.8,1.25]
lstyle=['solid','dashed','dotted','dashdot']
counter = 0
for a in A:
u, t = RK4(fcn, Tspan, I, Nt, k+2,a)
plt.plot(t, u[:,3],'-',linestyle=lstyle[counter],label=
"a="+str(a),linewidth=4)
plt.title(r'$K = $ '+str(k+2)+' , '+r'$\omega
= 1.5$ ',fontsize=28)
counter=counter+1
#plt.ylim((0,0.15))
plt.xlabel(r'$t$',fontsize=30)
plt.ylabel(r'$\rho$',fontsize=30)
plt.legend(loc="lower left",fontsize=15)
plt.tight_layout()
plt.savefig("/home/peguykameni/Documents/s5k6.png")
```



```
#plt.xlim((0,20))

#plt.grid(True)
plt.show()

import numpy as np
import matplotlib.pyplot as plt
plt.xticks(fontsize=20)
plt.yticks(fontsize=20)
Tspan = [0.,14]
Nt = 90000
plt.rc('font', family='serif', serif='cm30')
plt.rc('text', usetex=True)
#intial Condition:
M0=0.002; y0=0.03; g0=0.1; rho0=0.1
#M0=0.05*np.pi; y0=0.3; g0=0.7; rho0=0.8
I = np.stack((M0,y0,g0,rho0))
k=3
#A=[0.001,0.002,0.003,0.01,0.02]
A=[0,0.002,0.005,0.008, 0.026]
lstyle=['solid','dashed','dotted','dashdot','solid']
counter = 0
for a in A:
u, t = RK4(fcn, Tspan, I, Nt, k+2,a)
if(a!=A[len(A)-1]):
plt.plot(t, u[:,3],'-',linestyle=lstyle[counter],label=
"a="+str(a),linewidth=4)
else:
```

Appendix

```
plt.plot(t, u[:,3],'-',linestyle=lstyle[counter],label="$a_{th}$  
="+str(a),linewidth=4)  
plt.title(r'$K = $ '+str(k+2)+' , '+r'$\omega = 1.5$ ',fontsize=28)  
counter=counter+1  
#plt.ylim((-0.12,0.12))  
plt.xlabel(r'$t$',fontsize=30)  
plt.ylabel(r'$\rho$',fontsize=30)  
plt.legend(loc="upper left",fontsize=16)  
plt.tight_layout()  
plt.savefig("/home/peguykamani/Documents/s5k13.png")  
#plt.xlim((0,3))  
  
#plt.grid(True)  
plt.show()
```

Publications

- [1] **P. Kameni Nteutse**, A.M. Dikandé and S. Zekeng *Competing effects of Kerr nonlinearity and K-photon absorptions on continuous-wave laser inscriptions*. Opt. Quant. Electron 51, 313 (2019), Impact factor 1.842, <https://doi.org/10.1007/s11082-019-2031-5>

- [2] **P. Kameni Nteutse**, A.M. Dikandé and S. Zekeng *Laser dynamics in nonlinear transparent media with electron plasma generation: effects of electron-hole radiative recombinations*. J. Opt. 23, 035402 (2021), Impact factor 2.379, <https://doi.org/10.1088/2040-8986/abdf6a>